universität wien

MASTERARBEIT / MASTER'S THESIS

Titel der Masterarbeit / Title of the Master's Thesis

„Synthesis of carbon coated SnS_2 anode active materials for Li-ion batteries“

verfasst von / submitted by

Lukas Fischer, BSc

angestrebter akademischer Grad / in partial fulfilment of the requirements for the degree of

Master of Science (MSc)

Wien, 2021 / Vienna 2021

Studienkennzahl lt. Studienblatt / degree programme code as it appears on the student record sheet:	A 066 862
Studienrichtung lt. Studienblatt / degree programme as it appears on the student record sheet:	Masterstudium Chemie
Betreut von / Supervisor:	ao. Univ.-Prof. MMag. Dr. Hans Flandorfer

Preface

First and foremost, I want to thank my supervisors Damian Cupid and Hans Flandorfer for their patient guidance during this master's thesis and their support during my academic development.

This work was undertaken from June 2020 to December 2020 at the Austrian Institute of Technology (AIT) and the University of Vienna. Special thanks to the teams of electric drive technology and low emission transport at AIT and the Department of Inorganic Chemistry - functional Materials at the university.

Thanks to Stephan Puchegger and Ningxin Zhang for their help with the SEM measurements.

It is needless to say that I want to thank my parents Hermine and Christian, my brother Michael, my uncle Walter and my close friends for their support throughout my life. Ein besonderes Dankeschön auch an meine Großeltern.

Table of Contents

1 Introduction

Due to the steadily increasing energy demands of today's society, mankind is facing severe challenges such as a strong dependency on fossil fuels coupled with high CO_2 and other greenhouse gas emissions, which lead to global warming. Consequently, there is an increasing requirement for energy from sustainable and renewable sources as alternatives for the use of fossil-fuel and crude oil. Additionally, energy storage systems and rechargeable systems are necessary in order to store energy from only temporally available sources like solar and wind energy.

Lithium-ion batteries show remarkable properties such as high operating voltages, high energy densities, low self-discharge rates and a relatively wide operation temperature range. Therefore, they are considered as promising energy sources in the transportation, communication, and portable electronics sectors. Consequently, there is a constant need for improvement in the cell properties and performance characteristics.

This master thesis was performed within the framework of the project "Optimized Processing Parameters of **Tin S**ulfides as Anode Materials in **L**ithium **I**on **B**atteries: **TINSLIB**", which is funded by the FFG (Österreichische Forschungsförderungsgesellschaft). This is a collaborative project between the Austrian Institute of Technology AIT and the industrial partner Frimeco. The work performed in this master thesis was supervised together with the University of Vienna at the Faculty of Chemistry, Department of Inorganic Chemistry - functional Materials. Within the scope of TINSLIB, tin sulfides are investigated as potential anode active materials for lithium-ion batteries. In this master's thesis, the electrochemical behavior of SnS_2, SnS_2/C composite materials and carbon coated tin sulfides as alternative anode active materials to conventional graphite are specifically investigated.

The major problems and disadvantages of advanced anode materials for lithium-ion batteries such as silicon and tin are the large volume expansions which occur due to formation of various Li-alloys. This results in severe degradation mechanism leading to cyclic capacity fade. Possible strategies for performance enhancement are carbon coating and particle size reduction. Both of these approaches are examined more closely in this thesis.

The tin-sulfide anode materials were prepared via two different routes and characterized using thermogravimetric analysis, electron microscopy and X-ray diffraction. In the first approach, known as the mechanochemical route, SnS_2 and SnS_2/C with different carbon contents were ball-milled in argon atmosphere. In the second approach, a thermal route was selected, in which SnS_2 was mixed with polyvinyl alcohol as a carbon source and subjected to thermal treatments under Argon for different time durations. Electrochemical cells vs. Li^+/Li were prepared and electrochemical investigations were performed using galvanostatic cycling under potential limitation.

2 Lithium-ion batteries

Electrochemical or galvanic cells are electrochemical power sources with an anode, a cathode and an electrolyte as the main elements. The electrical energy is stored as chemical energy in a reductant and an oxidant. When the redox reaction takes place on the cell level, an electronic current is produced, which flows through an external electric conductor. Thereby, chemical energy is converted into electrical work. Galvanic cells are categorized in primary cells, secondary cells and fuel cells. Primary cells are non-rechargeable because the electrochemical processes which takes place is practically irreversible. Secondary cells are rechargeable since the electrochemical reactions can be reversed through external application of electrical energy. According to this definition, lithium-ion batteries (LIBs) are secondary cells. Fuel cells are able to, in contrast to the others categories, operate continuously since the reactants are fed to the cell externally [1][2].

A Ragone plot of common battery systems is illustrated in Figure 1 and shows the high energy density of Li-ion batteries compared to lead-acid batteries (also known as SLI-batteries from **s**tarter-**l**ight-**i**gnition) for cars, nickel-cadmium batteries and nickel-metalhydrid systems. PLiONs are plastic lithium-ion batteries [3].

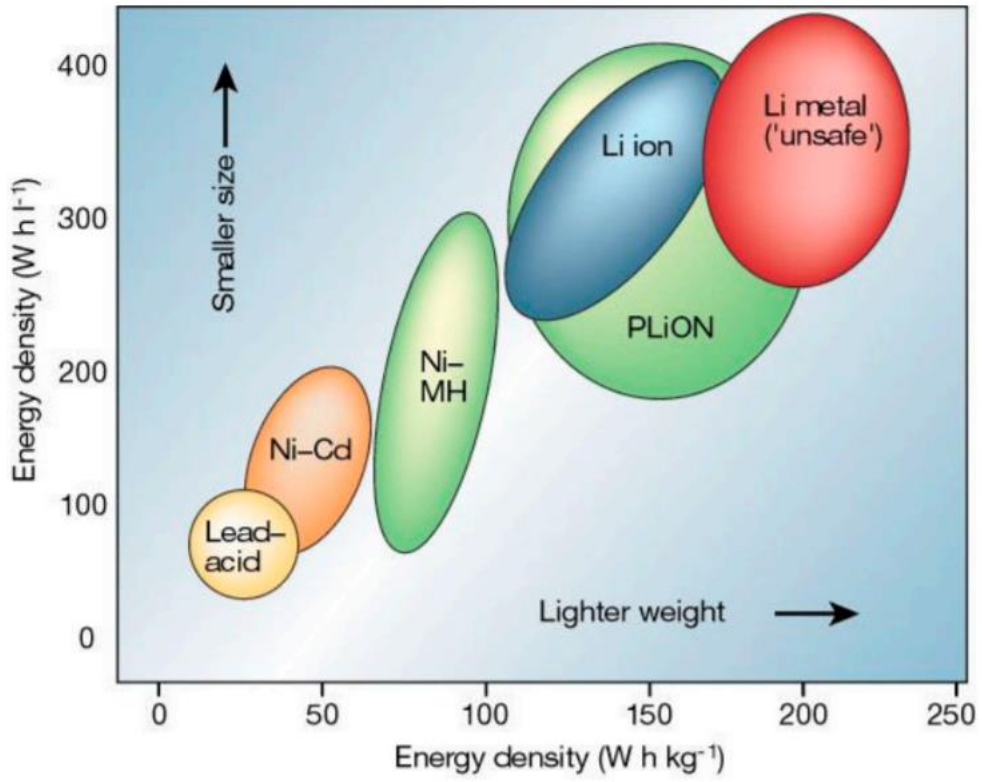

Figure 1: Ragone plot of different battery systems [3].

The amount of electrical energy available in a cell can either be expressed per unit volume (Wh/l) as volumetric energy density or per unit weight (Wh/kg) as gravimetric energy density. The latter is preferably called specific energy since density generally refers to a unit of volume. Lithium metal is quite unique compared to other metals, as it has the lowest electrode potential of -3.01 V versus the normal hydrogen electrode, the lowest density with 0.54 g cm^{-3} and a low electrochemical equivalent of 0.259 g Ah^{-1} [1]. Consequently, a mass of 7.19 x 10^{-5} g lithium

can be transported by one coulomb of electric charge. Nowadays Li-ion batteries do not contain lithium metal, whereas lithium primary batteries do [3]; see also subchapter 2.3. A very brief history of the development of LIBs is given in the following paragraph.

Stanley Whittingham investigated titanium disulfide as a possible intercalation cathode material in the 1970s, at the time of the oil crisis. Furthermore John B. Goodenough proposed metal oxide materials as alternative cathode material and Akira Yoshino used carbon materials instead of lithium as anodes in the 1980s. In 1985, Akira Yoshino built the first commercially viable lithium-ion battery and the system was commercialized by Sony in 1991 for usage in camcorders. The Nobel prize for chemistry in 2019 was awarded to John B. Goodenough, M. Stanley Whittingham and Akira Yoshino “for the development of lithium-ion batteries” and their contributions in the development of intercalation materials [4][5].

The concept of lithium-ion batteries will be explained in more detail in subchapter 2.1.

2.1 Working principle of LIBs

A conventional lithium-ion battery consists of five fundamental elements, namely a negative electrode (anode, e.g. graphite), a positive electrode (cathode, lithium metal oxide, e.g. $LiCoO_2$), a separator (e.g. a polymer), an electrolyte (organic solvent containing lithium salt, e.g. $LiPF_6$ in dimethyl carbonate) and the electrode current collectors. Generally, aluminum is used as the positive current collector whereas copper is used the negative current collector [6]. A schematic LIB is illustrated in Figure 2.

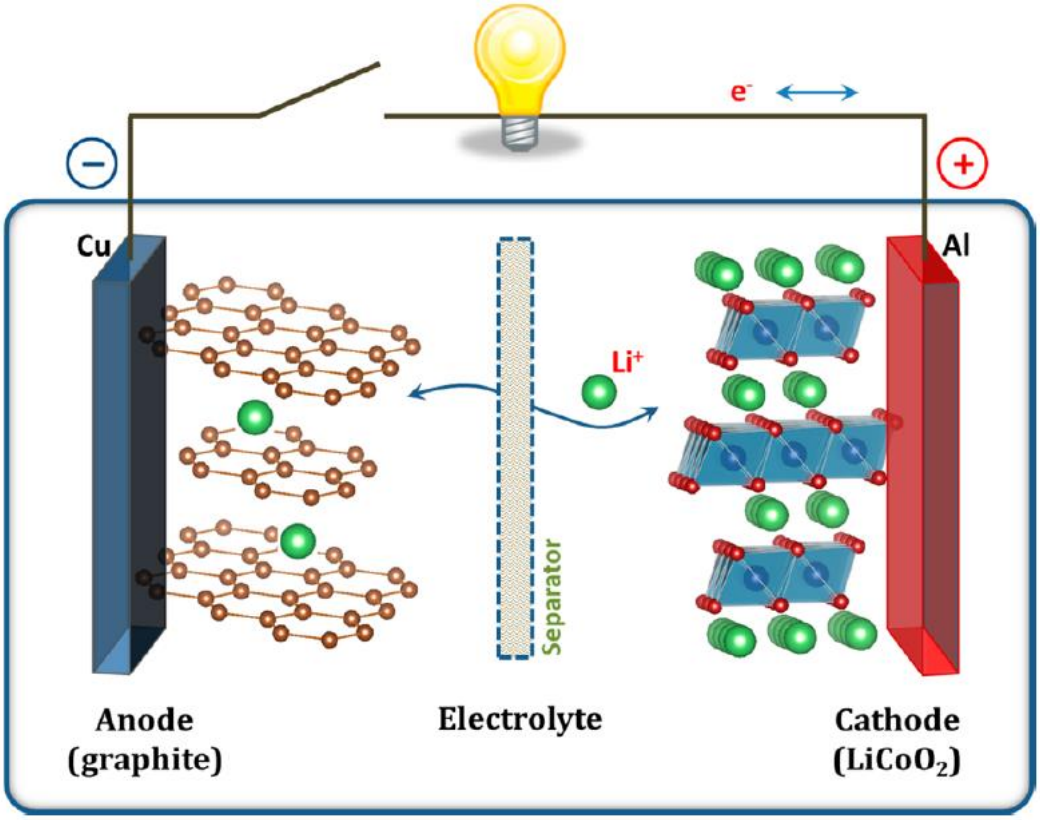

Figure 2: Schematic Li-ion battery [2].

The half-cell reaction for the positive electrode during charge is:

$$LiMO_2 \leftrightharpoons Li_{1-x}MO_2 + x\,Li^+ + x\,e^-$$

where M is a transition metal cation. For the negative electrode, the half-cell reaction during charge can be written as:

$$C + x\, Li^+ + x\, e^- \leftrightharpoons\ Li_xC$$

Correspondingly, the full-cell reaction during charge is expressed as:

$$LiMO_2 + C \leftrightharpoons\ Li_xC + Li_{1-x}MO_2$$

Generally, the lithium-ions in the cell shuttle between positive and negative electrode during charge and discharge; therefore the working principle of the rechargeable LIB is also called the rocking chair mechanism [1]. The open-circuit voltage of a chemical cell is determined by the difference of the electrochemical potentials of the charge carrier (lithium) in the anode and cathode [2]. During discharge, lithium-ions are intercalated into the crystal lattice of the active material of the positive electrode (cathode), and the cell voltage decreases. During charge, lithium-ions are extracted from the active material of the cathode intercalated into the negative electrode (anode), resulting in an increase of the cell voltage. During the charge step, the active material in the positive electrode is oxidized whereas the active material in the negative electrode is reduced. The terms cathode and anode must be treated carefully in this context. For example, the positive electrode is the cathode during discharge but the anode during the charge process [7].

In addition to the electrochemical reactions taking place at the electrodes, other factors also influence the available energy and general behavior of a battery, namely the electrolyte and its conductivity as well as the separator materials and their characteristics. Separators are permeable for the electrolyte and Li^+ ions but impervious for electrons and therefore prevent short circuits from taking place via contact between the anode and cathode. The electrolyte acts as ionic conductor as well as electronic insulator so that the electron current flows through an external circuit and is therefore able to perform work during discharge [7][8]. The energy difference between the lowest unoccupied molecular orbital (LUMO) and the highest occupied molecular orbital (HOMO) of the liquid electrolyte determines the voltage stability window of the battery.

2.2 Battery characteristics and parameters

This subchapter gives an overview on important battery characteristics and parameters and is therefore not only applicable for LIBs but for all galvanic cells.

The total energy in a cell is the integral of voltage–capacity curve of the electrochemical system:

$$Energy = \int E\, dq$$

where *E* is the output voltage and *q* is the amount of electronic charge transferred. The maximum capacity is the charge that can theoretically be transferred between the anode and cathode in a cell. While voltage is an intensive quantity, the charge capacity is an extensive quantity, which leads to the fact that only the capacity (and not the voltage) is dependent on the amount of active material in the battery [7].

The voltage of the cell itself is determined by the difference of the electrochemical potentials of the charge carrier in the anode and the cathode [2].

$$E = (\mu_A - \mu_C) / e$$

where *e* is the elementary charge. The maximum theoretical specific energy (MTSE) for a reaction can be calculated using following equation:

$$MTSE = \frac{x\, E}{W_t} F$$

where *x* is the number of elementary charges per mol, *E* is the voltage, W_t is the sum of all molecular masses of involved reactants and *F* is Faraday's constant [7].

Cyclability and cycling behavior are assigned a fundamental role in modern battery research. The major goal of battery design is to maintain the initial properties of the cells over a large number of discharge – charge cycles. In the real case, the initial capacity is always reduced. One way to indicate and illustrate the change in capacity of the cell is to calculate the coulombic efficiency, which is the fraction of capacity that is still obtainable on discharge after charging [7].

$$Coulombic\ efficiency = \frac{q_{dis}}{q_{ch}}$$

To graphically illustrate the change in Colombic efficiency, the percentage of the original capacity still retained can be plotted against the number of cycles. Coulombic efficiency and cycling behavior are illustrated in Figure 3.

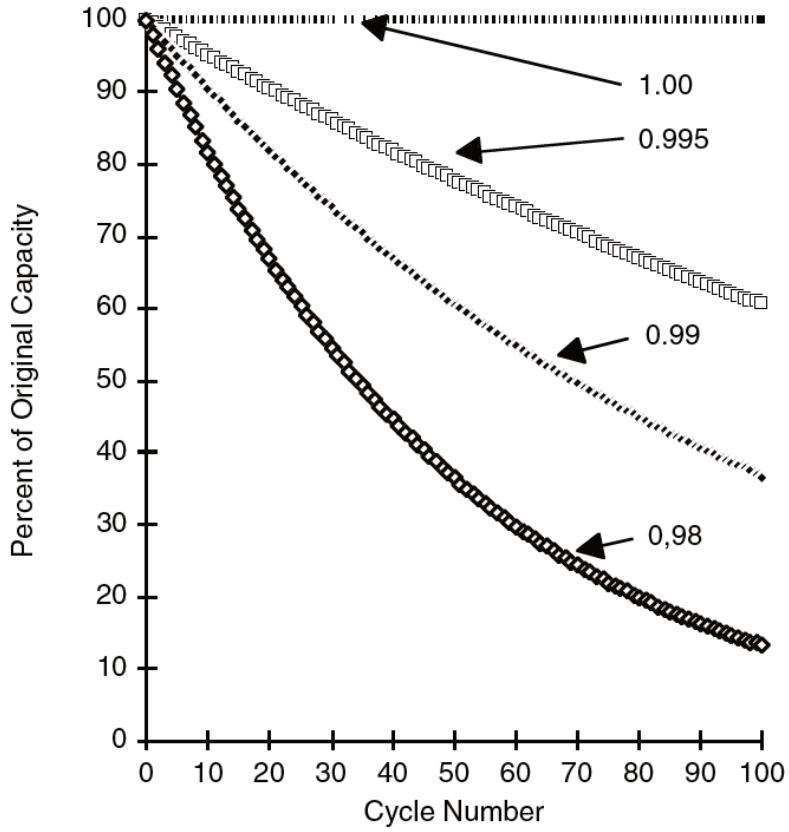

Figure 3: Cycling behavior and illustration of coulombic efficiency [7].

One sees that already small deviations from perfect coulombic efficiency (=1) have huge impacts on the remained capacities. A minimal decrease in coulombic efficiency of e.g. 0.005 leads to a dramatic decrease in long-time performance as illustrated in Figure 3. Important influences on the coulombic efficiency are the current density and depth of discharge during cycling. Strategies such as particle size reduction of active material can lead to improvement in cycling stability. This is explained in more detail in subchapter 2.3 [9].

The correlation between thermodynamics, phase diagrams and electrochemistry was investigated in detail by Godshall et al. [10]. Their work shows important coherences between thermodynamic parameters, phase equilibria and electrochemical measurements and electrochemical values [10]. The first equation of this subchapter to exemplify this correlation can therefore be rewritten as:

$$\Delta G_r^0 = -z\,F\,E$$

$$\Delta G_r^0 = -z\,F \int_0^x E\,dx$$

$$\Delta G_r^0 = \Delta G_f^0(products) - \Delta G_f^0(reactants)$$

where z is the number of electrons transferred per formular unit and ΔG_f^0 is the integral Gibbs free energy of formation. ΔG_r^0 is standard Gibbs free energy change per mol of reaction that can be calculated by integration of the area under the equilibrium potential-composition (E-x) curve [10]. This is equivalent to the reversible work which can be performed by the cell.

An equilibrium discharge curve is illustrated in Figure 4, where various plateau voltages can be observed. In order to understand the shape of the discharge curve, the Gibbs phase rule can be used.

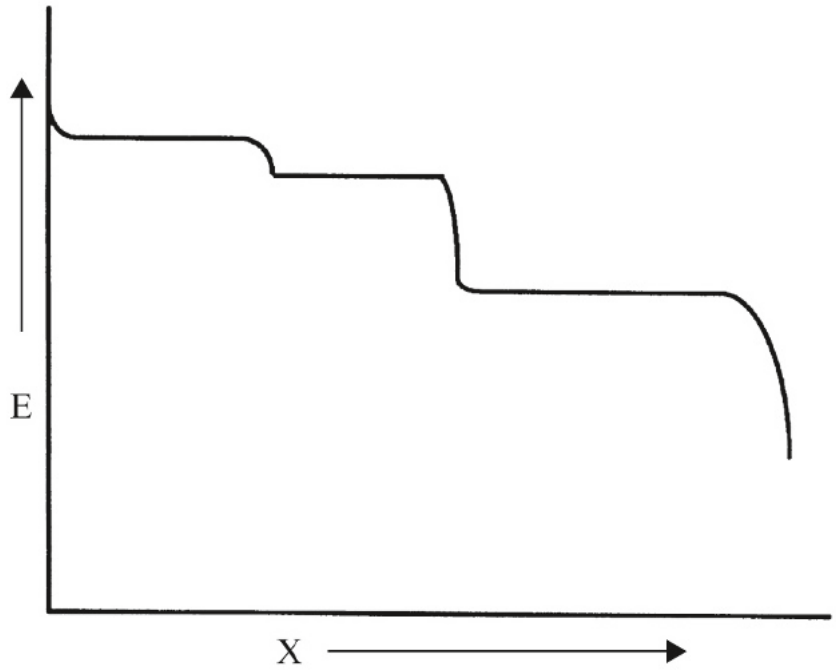

Figure 4: Equilibrium discharge curve with multiphase reactions [7].

The Gibbs phase rule shows the relation between number of components, number of phases and degrees of freedom in a system and reads as follows:

$$F = C - P + 2$$

In this expression, *C* is the number of components, *P* the number of phases in equilibrium and *F* is the amount of degrees of freedom. At constant pressure, the rule can be simplified to:

$$F = C - P + 1$$

Thus, ternary systems with one-phase and two-phase equilibria at constant temperature show nonzero degrees of freedom. On the other hand, the system becomes invariant (F=0) when three phases coexist. These relations are consequently reflected in the profile of the discharge curve. Constant voltage plateaus are visible where the number of residual degrees of freedom F equals zero [7], and tie lines illustrating variant one- and two phase equilibria in a ternary system can be drawn at steps between plateau voltages [10].

The potential of the plateaus can generally be calculated using the following equation:

$$E - E^0 = \frac{-\Delta G_r^0}{F}$$

where E^0 is the potential against pure lithium [7].

2.3 Anode materials for LIBs

Although metallic lithium has the lowest potential and the lowest weight per unit charge compared to all lithium reservoir materials, it was replaced quite quickly as the negative electrode material for secondary Li-ion batteries for safety reasons. The major problems regarding the use of elemental lithium are deposition at unwanted locations, shape change, dendrite formation, filamentary growth and thermal runaway [7]. Alternatives have been found in the form of lithium carbon alloys, which are the most common anode materials today. However, metallic lithium alloys are gaining more importance in next generation LIBs using solid electrolytes which, however, still suffer on low ion conductivity compared to liquid electrolytes.

The first carbonous negative electrode materials were developed by Akira Yoshino in the form of petroleum coke. In general, there are many different carbon modifications existing in 1-dimensional, 2-dimensional and 3-dimensional structures. The most popular one is graphite which is used in most of the current commercial LIBs. Graphite is amphoteric, meaning that cations or anions can be inserted between its layers. The specific capacity of fully lithiated carbon is 372 $mAhg^{-1}$ and the fully lithiated phase is LiC_6. C-atoms in graphitic carbon are sp2-hybridized and they are arranged in a hexagonal layers [1]. The remaining p_z-orbitals, filled with a single electron, form band structures which cause the metallic properties of graphite.

A nowadays very commonly used carbon source, as an alternative for petroleum coke and graphite, are mesophase carbon microbeads (MCMB). MCMBs are synthesized by heat treatment of a precursor carbonaceous material like petroleum pitch at about 400°C. Consequently, a mesophase of spherical particles is formed that is stabilized during a following quenching step. Isotropic materials that surround the spherical particles are extracted here. They are reheated at higher temperatures over 2000 °C what causes an improvement in the degree of graphitization and low surface area compared to its particle size. MCMBs show excellent properties for the use in LIBs due to their high specific capacity and their flat discharge profile [11]. Figure 5 shows a SEM micrograph of a MCMB with a diameter of about 6 µm and illustrates its spherical form.

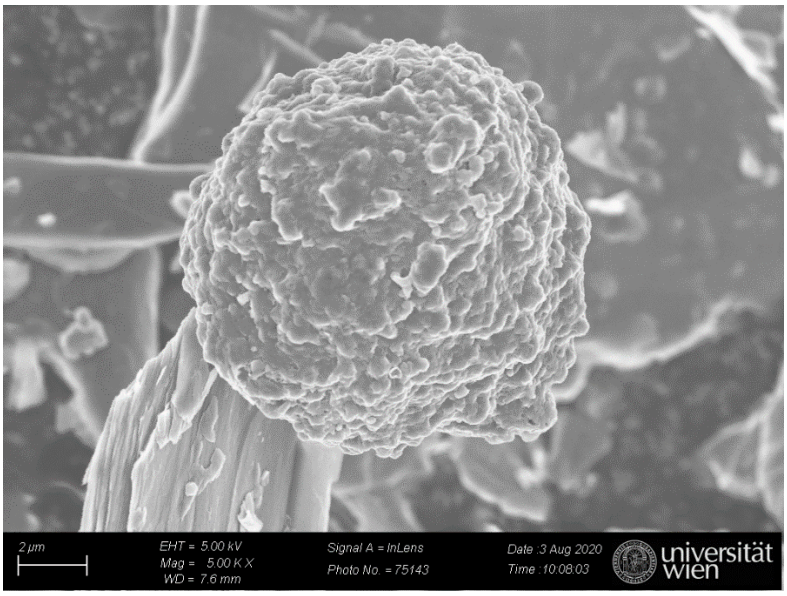

Figure 5: SEM micrograph of meso carbon micro beads (MCMB).

Poor specific capacity sets limits for carbon-based materials in modern applications. Obvious alternatives are, among others, further elements from Group IV of the periodic table, also called carbon group, such as silicon, germanium and tin [12]. Table 1 lists density, theoretic specific capacity, theoretical charge density, volume expansion, the potential versus Li^+/Li and the composition of the fully lithiated phase for Li, C, Si and Sn concerning their usage as anode materials in Li-ion batteries.

Table 1: Material characteristics of various anode materials for LIBs [9].

	Li	**C**	**Si**	**Sn**
Density [g cm^{-3}]	0.53	2.25	2.33	7.29
Lithiated phase	Li	LiC_6	$Li_{4.4}Si$	$Li_{4.4}Sn$
Theoretical specific capacity [mAh g^{-1}]	3862	372	4200	994
Theoretical charge density [mAh cm^{-3}]	2047	837	9786	7246
Volume expansion [%]	100	12	320	260
Potential vs. Li [V]	0	0.05	0.4	0.6

Table 1 illustrates the low theoretical specific capacity and low theoretical charge density of carbon compared to silicon and tin. Another advantage of Si and Sn are the potentials vs. lithium since they are higher than that of graphite and therefore the risk of dendrite formation during charge is lower. All of them form different alloys with Li and are therefore classified as alloy anode materials. The major challenges of these alloy anodes are their large volume changes during lithiation as illustrated in Table 1 [13].

Silicon-based anodes impress with a theoretical specific capacity of 4200 $mAhg^{-1}$ associated with the formation of $Li_{4.4}Si$ but suffer from problematic volume changes of up to 320 %. Sn-based anodes do not exhibit as large specific capacities as Si, but slightly smaller volume expansions. In comparison, the volume expansion of graphite with 12 % is very low. A particular advantage of tin is its higher electric conductivity compared to silicon [9].

The electrochemical performance of Sn-based anodes were investigated in detail by Wachtler et al. [13]. Tin has a theoretical specific capacity of 994 $mAhg^{-1}$ when $Li_{4.4}Sn$ (4.4 Li + Sn → $Li_{4.4}Sn$) is formed with an associated volume expansion of up to 260 % [9]. During lithiation of Sn, several Li_xSn alloys can be observed. This is in accordance with the phase diagram in the Li-Sn binary system, which shows seven intermediate phases (for more details, refer to subchapter 3.3 and Figure 12). These phases are Li_2Sn_5 (with the lowest degree of lithiation), LiSn, Li_7Sn_3, Li_5Sn_2, $Li_{13}Sn_5$, Li_7Sn_2 and the fully lithiated $Li_{17}Sn_4$ [14].

The reasons for the relatively poor long-term performance of alloy anodes are described in various literature sources. According to Son et al. degradation mechanisms can be categorized in mechanical changes (volume expansion), chemical changes (solid electrolyte interface (SEI) formation) and atomic changes (phase transformation) for Si (and Sn) [15]. According to Wachtler et al. and W.-J. Zhang et al. the reasons for irreversible capacity losses and cyclic capacity fade are electrolyte decomposition and consequent increased formation of SEI films, loss of contact between current collector and active material due to volume changes, trapping of lithium in the host alloy due to thermodynamic and kinetic factors and aggregation of alloy

particles [9][13]. All fading mechanisms during charging and discharging are directly or indirectly related to the volume changes. Volume changes during cycling leads to cracks and pulverization of the electrode active material, thereby yielding new interfaces between Si and/or Sn and the electrolyte and therefore continuous SEI formation during cycling [15]. These degradations mechanisms are illustrated in Figure 6.

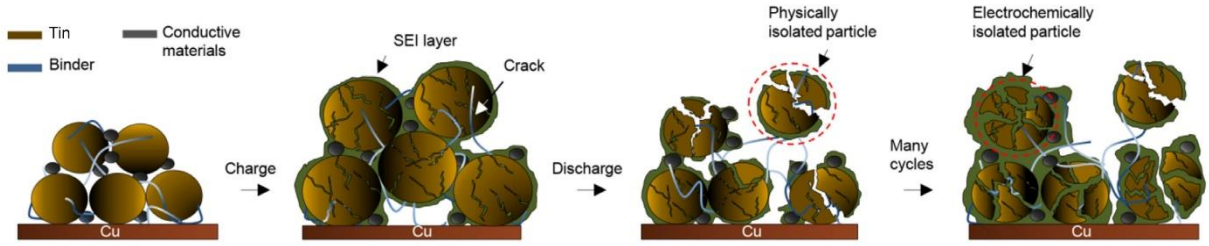

Figure 6: Illustration of degradation during cycling. Adapted for Sn, originally for Si [15]*. Pulverization and cracking occur due to large volume expansion during cycling. Each new cycle results in the growth of more SEI layer. Additionally, due to cracking and pulverization, some active material particles become physically and electrochemically isolated.*

Various approaches have been developed to make use of the high capacities of alloy anodes despite their degradation mechanisms described above. According to W.-J. Zhang et al. some of these approaches are usage of multiphase composites forming matrices including inactive-matrix composites, active-matrix composites, carbon-based composites and porous structures. Another possibility is particle size control and dimension reduction, both of which can be achieved with ball-milling [9]. Figure 7 illustrates summarizes the possible problem-solving strategies concerning the cycling capacity fade.

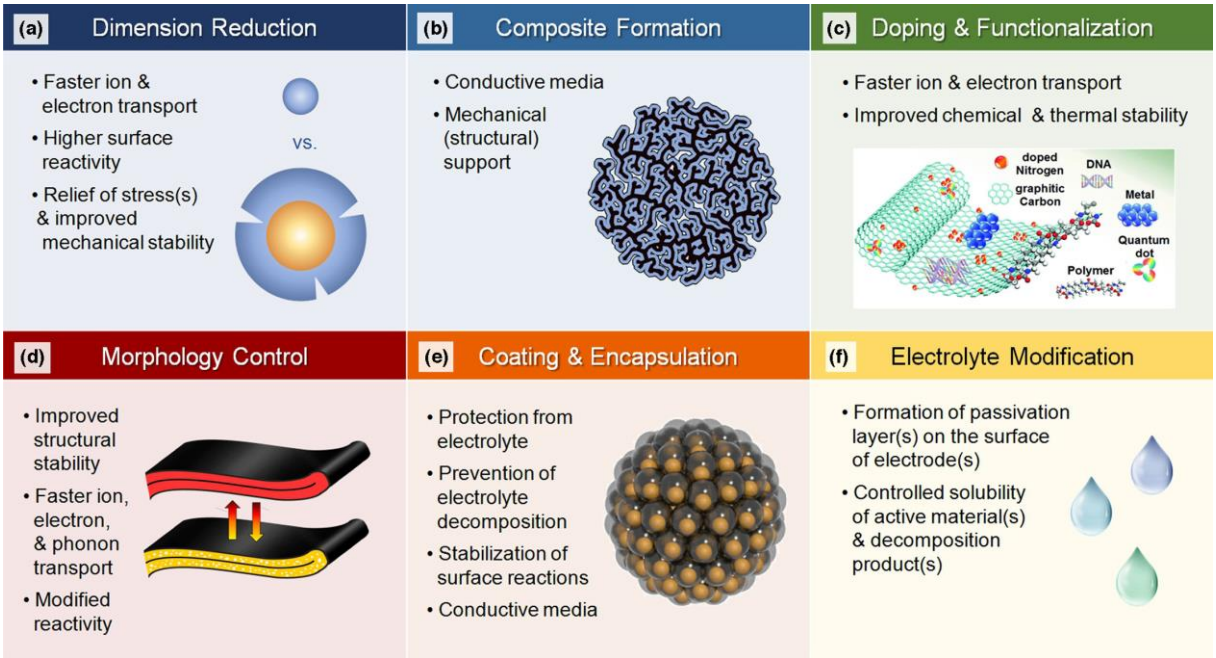

Figure 7: Strategies for performance enhancement of anode materials [16]*.*

In this master thesis, the mechanochemical approach is used to explore the effects of dimension reduction and composite formation (Figure 7 (a) and (b), respectively) on the cycle life of tin-sulfide anodes. Furthermore, the thermal approach (Figure 7 (e)) is targeted toward

developing a conductive coating on the tin-sulfide particles. Nitta et al. claim that a reduction in dimensions of the active material particles leads to higher specific surface areas and therefore higher surface reactivity, improved stability due to lower stress developments and faster transport mechanisms. Coating of the active material particles with e.g. carbon protects them from the electrolyte and its decomposition products and can also be used to improve the electric conductivity. Other possible performance enhancements are doping and functionalization, morphology control and electrolyte modification. The latter play a minor role in this thesis [16].

One way to make use of the high specific capacity of Sn and limit the problems due to its degradation mechanisms is to use Sn-based chalcogenide compounds like SnO_2, SnS and $SnSe_2$ as anode active materials. In this thesis, focus is placed on SnS_2. SnS_2 as an anode active material exhibits a theoretical capacity of 1209 $mAhg^{-1}$ for full lithiation of SnS_2 and a reversible capacity of 644 $mAhg^{-1}$. A Li_2S inert matrix is formed during the first discharge cycle according to the generalized reaction.

$$SnS_2 + 4\,Li^+ + 4\,e^- \leftrightharpoons 2\,Li_2S + Sn$$

This Li_2S matrix phase is intended to impart mechanical and structural stability to the electrode active material, as illustrated in Figure 7 (b). On the other hand, the reversible capacity of the electrode originates from the alloying reaction of ($Li^+ + e^-$) and Sn [13]. The crystal structure of SnS_2 and the lithium insertion mechanism including intercalation, conversion and alloying reaction will be explained in more detail in subchapter 3.1.

3 Literature review

3.1 SnS_2

Tin(IV)sulfide is described in various literature references as a versatile material with the advantage that the elemental components are relatively cheap and abundant. Research has been performed on SnS_2 as an earth-abundant disulfide photocatalyst for water photolysis in hydrogen gas synthesis, a promising IV-VI 2-D semiconductor, in photovoltaics (PV) and of course as an anode active material in LIBs [17][18].

Tin(IV)sulfide has a hexagonal layered CdI_2 crystal structure with P-3m1 symmetry (space group No. 164). The lattice constants of the unit cell are a= 3.649 Å and c= 5.899 Å. SnS_2 is built up of edge-sharing SnS_6-octahedra in hexagonal layers and shows S-Sn-S stacking along the c-direction [0 0 1]. The layers are bound together via weak Van der Waals interactions [19].

As expected in such kind of compounds polytypism based on stacking variants along [0 0 1] can be observed. Their description here is based on the so-called ABC$\alpha\beta\gamma$-notation where in this case the upper case Latin letters describe the stacking of sulfur layers whereas the lower case Greek letters describe the stacking of Sn-layers. The basic polytype 2H-SnS_2 [20] is represented by (AγB) [21]stacking while others like 4H-SnS_2 show (AγB)(AβC) stacking and 18R-SnS_2 shows (AγB)(AγB)(CαB)(CβA)(CβA)(BγA)(BαC)(BαC)(AβC) stacking [22].

It can be seen that intra-layer stacking of the S-Sn-S units remains always the same whereas the interlayer stacking alters. The crystal structure of the basic polytype SnS_2 which contains only one S-Sn-S layer per unit cell is illustrated in Figure 8. The crystal structure was drawn using the free of charge software “Visualization for Electronic and Structural Analysis” (VESTA).

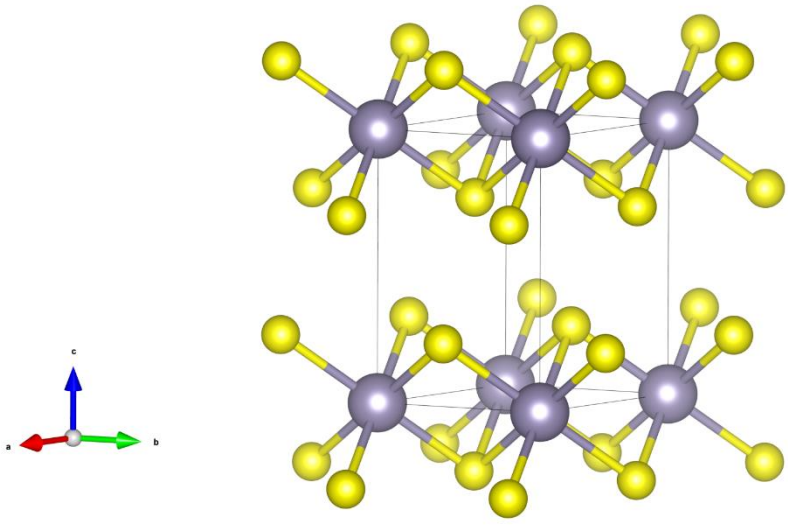

Figure 8: Crystal structure of SnS_2.

S-atoms occupy 2d positions in the hexagonal lattice (shown as yellow spheres in Figure 8) whereas Sn-atoms occupy the octahedral intra-layer 1a position (shown as purple spheres in Figure 8). Vacant octahedral 1b positions and vacant tetrahedral inter- and intra-layer 2d positions are possible sites for Li intercalation.

The full lithiation of SnS_2 is divided into intercalation, conversion and alloying reactions. The intercalation of lithium into SnS_2 can be written as:

$$SnS_2 + x\ Li + x\ e^- \rightarrow Li_xSnS_2$$

After intercalation conversion happening formulated as:

$$SnS_2 + 4\ Li^+ + 4\ e^- \rightarrow Sn + 2\ Li_2S$$

During conversion, Sn and Li_2S form simultaneously in the active material. After conversion, only the reversible alloying and de-alloying of Sn takes place since the Li_2S is electrochemically inactive or inert. The reversible reaction between Sn and Li can be written as:

$$Sn + x\ Li^+ + x\ e^- \leftrightharpoons Li_xSn$$

where x varies between 0 and 4.4 with $Li_{17}Sn_4$ as the fully lithiated phase [23].

The insertion of lithium into the crystal lattice of SnS_2 (intercalation reaction) has been investigated by J. Morales et al. [24] and I. Lefebvre-Devos et al. [25]. Former performed chemical intercalation via treatment of SnS_2 with an excess of n-butyl-lithium and used X-ray powder diffraction, SEM and atomic absorption spectrometry for characterization. According to J. Morales et al. the first lithiated product ($x<0.6$) is isostructural with SnS_2 and shows similar unit cell parameters. Although the reduction of Sn^{4+} during ($Li^+ + e^-$) intercalation leads to negative charges in the layers which should increase the repulsion and decrease the strength of van der Waals bonds to increase interlayer spacing, this is counteracted by the Li cations, which induce attractions that decrease interlayer spaces. Due to these two contrary effects, there is no significant change in the unit cell parameters in the end [24]. The latter characterized chemically lithiated SnS_2 with X-ray diffraction, atomic emission spectroscopy and Mössbauer spectroscopy. Additional calculations of the theoretical electronic structures were performed with density-functional theory (DFT) methods. I. Lefebvre-Devos et al. postulate that the first lithium ions ($x<0.16$) are inserted into the inter-layer 1b octahedral sites of the van der Waals gap with a respective reduction of Sn^{4+} to Sn^{2+}. Increasing the amount of lithium ($x<0.49$) decreases interlayer interactions and Li ions are inserted into tetragonal intra-layer positions while a mixed occupation of inter-layer and intra-layer sites is postulated for further increased lithium amounts ($x<1.66$) [25].

3.2 The binary system Sn-S

Although there are many experimental investigations of this binary system, only the two from Sharma et al. [26] and G. Lindwall et al. [27] will be discussed. These two descriptions were chosen to discuss the different results that were achieved in this system regarding the allotropes of the intermediate phases. According to Sharma et al., the binary system Sn-S has three intermediate phases, namely SnS_2, Sn_2S_3 and SnS. Allotropes are indicated for all three phases: two for SnS (α-SnS and β-SnS), four for Sn_2S_3 (α-Sn_2S_3, β-Sn_2S_3, γ-Sn_2S_3 and δ-Sn_2S_3) and two for SnS_2 (α-SnS_2 and β-SnS_2). While SnS and SnS_2 melt congruently, melting of Sn_2S_3 occurs via a peritectic reaction. The system exhibits two miscibility gaps in the liquid phase, i.e. one in the Sn-SnS region and one in the SnS_2-S region. The phase diagram further shows three eutectic reactions, one between SnS and Sn_2S_3 and the others in the Sn-rich and the S-rich corners, respectively. Figure 9 and Figure 10 illustrate the described binary system Sn-S [26].

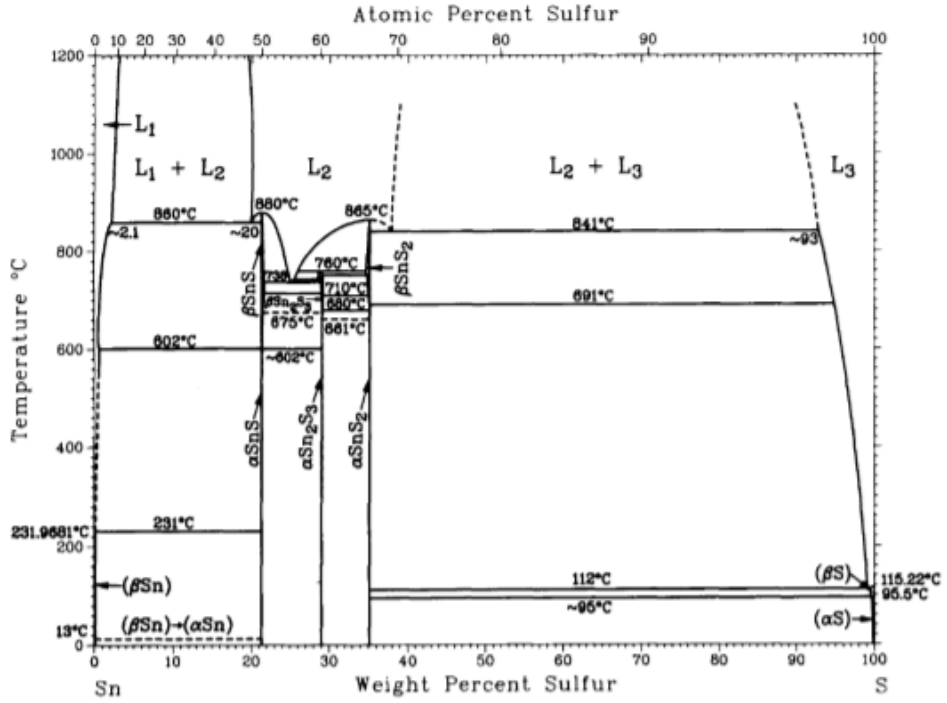

Figure 9: T-x phase diagram of the binary system Sn-S as reported by Sharma et al. [26].

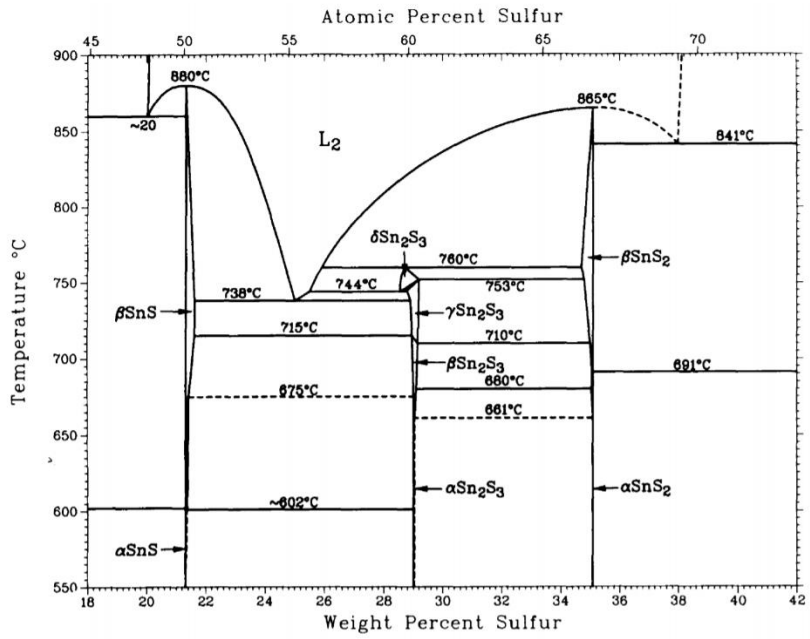

Figure 10: T-x phase diagram of the binary system SnS from 18 to 42 wt. % sulfur as reported by Sharma et al. [26].

G. Lindwall et al. developed a thermodynamic description of the binary system using the CALPHAD (CALculation of PHase Diagram) method with input from first-principle calculations and experimental literature date. Figure 11 shows the comparison of the calculated phase diagram using Gibbs energy minimization to the experimental data at a pressure of 1 bar. The experimental data were measured by Moh, Anderson and Ridge, Biltz and Mecklenburg respectively Albers and Schol [27].

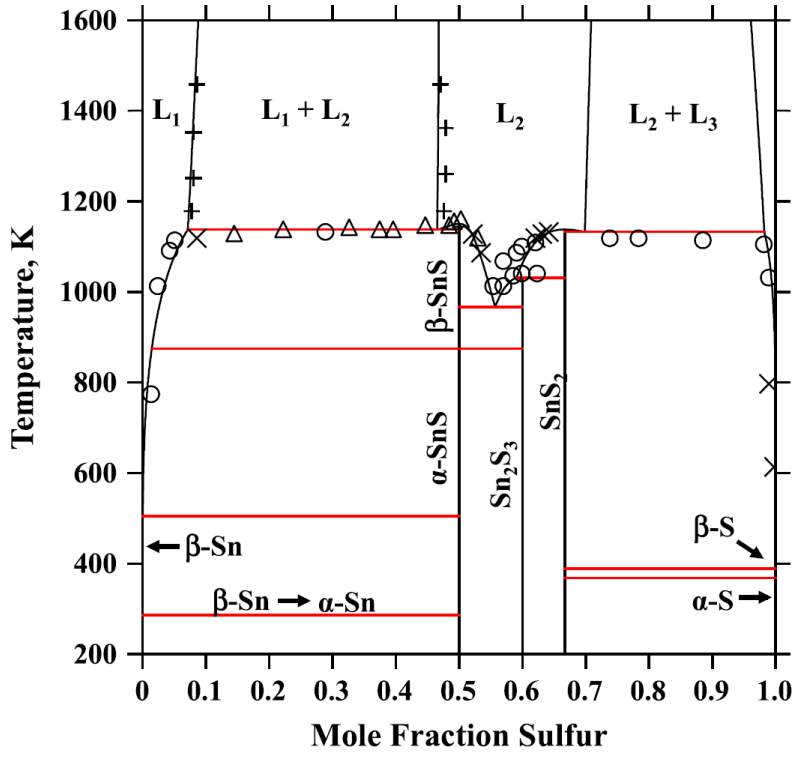

Figure 11: T-x phase diagram of the binary system Sn-S as reported by Lindwall et al. [27].

Red solid lines illustrate the calculated invariant transformation temperatures. In comparison to the diagram of Sharma et al. [26], only the SnS is shown to form allotropes (β-SnS (high temperature) and α-SnS (low temperature), whereas Sn_2S_3 and SnS_2 only show one stable modification. Table 2 lists invariant reactions in the binary system Sn-S.

Table 2: Reactions in the binary system Sn-S as reported by Lindwall et al. [27].

Reaction	**Mole fraction sulfur**	**Temperature [K]**
$L_1 \leftrightharpoons$ β-Sn; α-SnS	-	505
$L_2 \leftrightharpoons L_1$ + β-SnS	0.465	1137
$L_2 \leftrightharpoons$ β-SnS + Sn_2S_3	0.557	967
L_2 + $SnS_2 \leftrightharpoons Sn_2S_3$	0.591	1031
$L_2 \leftrightharpoons SnS_2 + L_3$	0.698	1132
$L_3 \leftrightharpoons SnS_2$ + β-S	1	388
T_m β-SnS	0.5	1150
T_m Sn_2S_3	0.6	1031
T_m SnS_2	0.6667	1138

3.3 The binary system Li-Sn

The binary system Li-Sn was first investigated by G. Masing et al. [28], who used thermal methods to study the behavior of Li with other metals like Na, K, Cd, Mg and Sn. Although the phases Li_4Sn, Li_3Sn_2 and Li_2Sn_5 were found in their publication, only Li_2Sn_5 still appears in current descriptions of the system. Grube et al. further investigated the system by measuring the electric conductivity and thermal properties of binary alloys including variant Li-Sn phases [29]. There have been many more investigations of this binary systems over the years, however they are not listed here for the sake of brevity.

One of the last assessments of the Li-Sn system was conducted by Li et al., who performed phase diagram investigations and developed a thermodynamic assessment of the Li-Sn system using the CALPHAD method. Experimental data were generated via differential thermal analysis (DTA) and XRD of several alloy compositions in the system [14]. The Li-Sn description was further updated by Reichmann et al. [30], who measured the heat capacity of $Li_{17}Sn_4$ and Li_7Sn_3 and used the data to improve their Gibbs free energy expressions. The binary system Li-Sn is illustrated in Figure 12.

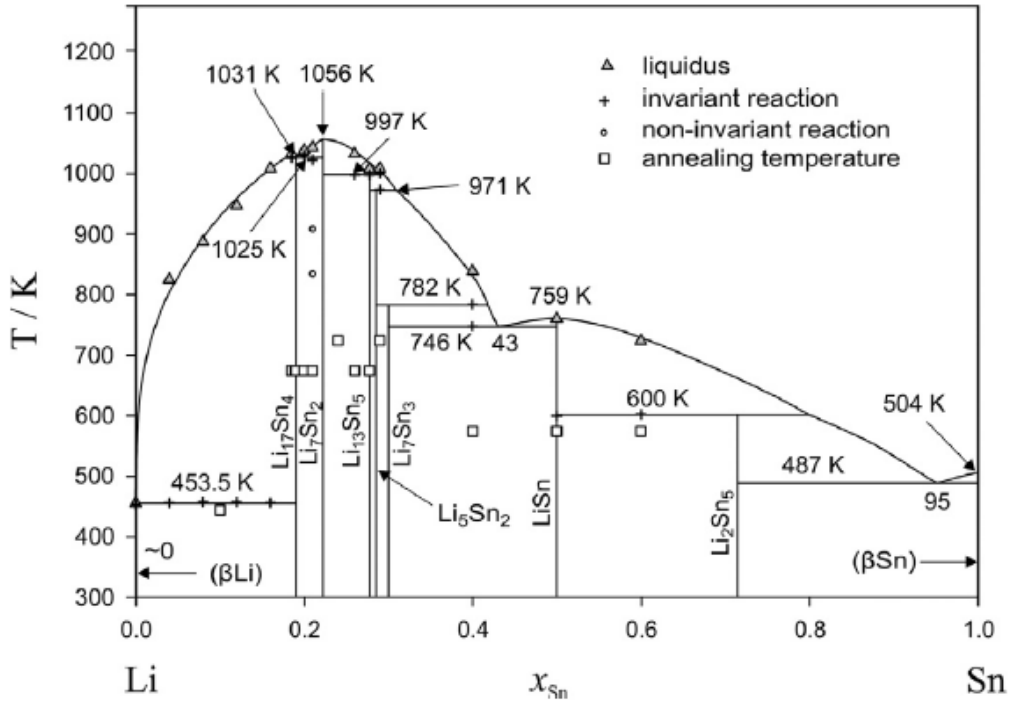

Figure 12: T-x phase diagram of the binary system Li-Sn as reported by Li et al. [14].

Seven intermediate phases are found in the system, namely Li_2Sn_5, LiSn, Li_7Sn_3, Li_5Sn_2, $Li_{13}Sn_5$, Li_7Sn_2 and $Li_{17}Sn_4$, whereby the latter is described as $Li_{22}Sn_5$ in other literature sources with a slightly different atomic arrangement (Sangster and Bale [31]). Table 3 lists the invariant reactions in the binary Li-Sn system as reported by Li et al. from DTA data.

Table 3: Invariant reactions in the binary system Li-Sn as reported by Li et al. [14].

Reaction	**Reaction type**	**Temperature [K]**
L ⇋ β-Li	Melting	454
L ⇋ β-Li + $Li_{17}Sn_4$	Degeneration	454
L ⇋ $Li_{17}Sn_4$	Congruent	1031
L ⇋ $Li_{17}Sn_4$ + Li_7Sn_2	Eutectic	1025
L ⇋ $Li_{17}Sn_4$	Congruent	1056
L + Li_7Sn_2 ⇋ $Li_{13}Sn_5$	Peritectic	997
L + $Li_{13}Sn_5$ ⇋ Li_5Sn_2	Peritectic	971
L + Li_5Sn_2 ⇋ Li_7Sn_3	Peritectic	782
L ⇋ Li_7Sn_3 + LiSn	Eutectic	746
L ⇋ LiSn	Congruent	759
L + LiSn ⇋ Li_2Sn_5	Peritectic	600
L ⇋ Li_2Sn_5 + ß-Sn	Eutectic	487
L ⇋ ß-Sn	Melting	505

The melting point of pure Li is at 453.6 K and that of pure Sn is 505.05 K. Li_2Sn_5 is the intermetallic phase that shows the lowest lithium content. This phase was found in several cycled electrodes and will be discussed in more detail in the results and discussion (chapter 6). Li_2Sn_5 is involved in an eutectic reaction with ß-Sn at 487 K and a peritectic reaction with LiSn at 600 K. $Li_{17}Sn_4$, which shows the highest degree of lithiation, melts congruently at 1031 K and participates in a eutectic reaction with Li_7Sn_2 as well as a degenerate reaction with ß-Li to form the liquid.

3.4 Mechanochemical route

In 2019, the International Union of Pure and Applied Chemistry (IUPAC) mentioned mechanochemical synthesis in their list of ten chemical innovations that will change the world. The major reasons for this are the elimination of potentially toxic solvents and the reduction of waste. The exact mechanisms taking place during mechanochemical treatments have not yet been clarified to this day and are still under investigation [32].

Ball milling has been applied in research as a relatively established synthesis method for the preparation of different battery materials. For example, Zhang et al. published a ball-milling approach to prepare insertion compounds, composites and sodium-based alloys as positive electrodes for sodium-ion batteries [33]. Likewise, graphene nanostructured cathodes for lithium-sulfur batteries have been developed by Xu et al. using ball-milling synthesis [34].

There are also several applications of ball-milling for the preparation of Sn-S-based electrode active materials. For example, J. Xia et al. synthesized SnS_2/graphene nanosheets via ball-milling for use as anode materials for LIBs [35]. H. Zhao et al. [36] followed a similar approach and published the article “Facile ball-milled synthesis of SnS_2-carbon nanocomposites with superior lithium storage”, in which SnS_2 nanocomposites with different carbon contents are prepared using a mechanochemical ball-milling synthesis method. SnS_2/C composites with carbon contents of 40, 50 and 60 wt. % were produced and electrochemically investigated. After mechanochemical synthesis, homogenously embedded nanoparticles of SnS_2 in a graphitic network were achieved. The best electrochemical performance was attained with 50 wt. % carbon. For such samples, a starting capacity of 700 $mAhg^{-1}$, an initial coulombic efficiency of 80.8% and a residual specific capacity of 540 $mAhg^{-1}$ after 100 cycles were obtained at a specific current of 100 mAg^{-1} in the potential window between 0.01 and 3 V vs Li^+/Li. According to the authors, the improved electrochemical performance is largely related to the reduction in particle sizes and increased carbon contents, resulting in improvements in electronic conductivity of the electrode. The carbon forms a graphite nanoparticle network with embedded electrochemically active nanoparticles particles [36].

3.5 Thermal route

In the literature, a variety of possibilities are described for applying conductive coatings to electrode materials using thermal methods. In most cases, polymers are used as the source material for the carbon coating layers. Liu et al. synthesized SnS/Polypyrrole ultrathin Nanosheets as anode materials for Li-ion batteries via pyrrole reduction and in-situ polymerization using a hydrothermal method [37]. Kim et al. coated SnS_2 nanoparticles with a carbon layer via the solvothermal method in ethylene glycole using glucose as carbon source. In that work, the SnS_2 nanoparticles were produced also via solvothermal synthesis from tin chloride and thioacetamides, and the presence of a carbon coating was confirmed by means of Raman spectroscopy [38].

According to Y. Li et al. [39] it is possible to apply a carbon coating onto SnS particles using thermal synthesis with polyvinyl alcohol (PVA) as the carbon source. Further details are described in the article “Nanoscale SnS with and without carbon-coatings as an anode material for lithium ion batteries”. The SnS samples were synthesized from elemental Sn and S powders using a ball-milling approach. Heat treatment of a 1:1 mixture of SnS and PVA was performed at temperatures of 400, 500, 600, 700 and 800 °C under argon flow. No information about the duration of the heat treatment can be found in the article. They claim 700 °C to be the best coating temperature. Coated particles with a particle size of 20-30 nm were shown using transmission electron microscopy (TEM). No further investigations regarding the composition of the coating layer were done, therefore it is not clarified if the coating is pure carbon, a hydrocarbon layer or a polymer. Carbon content determination using TG showed that the amount of carbon decreases with increasing coating temperature. In the sample that was coated at 700 °C, the carbon content was found to be about 6.2 wt. %. According to the authors, the anode active material shows good electric conductivity and a buffering matrix effect of the coating. Y. Li et al. claim that 53.1 % higher capacity values are attained after the 31st cycle in comparison with non-treated SnS anode material [39].

Peng et al. investigated the degradation mechanism of PVA during heat treatment using fourier transform infrared/thermogravimetric analysis (FT-IR/TGA) and mass spectrometric analysis (MS) and found that besides H_2O, the following products are eliminated in the first step: acetaldehyde, acetone, furan, acetic acid, low molecular polyenes and benzenoid derivatives [40]. This complex mixture of products together with sulfur- and SnS-vapor from SnS_2 makes a precise description of the reaction mechanism of PVA with tin sulfides in general very difficult.

4 Sample preparation and experimental

4.1 Mechanochemical route

SnS_2 powder from MKNano with an average particle size of 10 µm and a purity of 99% was milled in a planetary ball-mill machine (Fritsch pulverisette 6) in argon atmosphere. This was ensured by sealing the milling bowl with a clamping system in an argon-filled glovebox (MBraun) and placing it into the ball-milling machine. A ZrO_2 milling bowl was used in combination with ZrO_2 balls. Powder and balls were weighted in mass ratio of 1:20.

Depending on the particular sample, SnS_2 was prepared and used either in its pristine form or mixed with mesophase carbon micro beads (MCMB) graphite. Accordingly, SnS_2 powder with 10 and 20 wt. % MCMB powder were mixed in an agate mortar before the milling experiments to ensure a certain degree of homogeneity prior to milling. Ball-milling was performed using the airtight closed milling bowl with rotation speeds of 100, 200 and 400 revolutions per minute (rpm) respectively, for a total milling time of 1 hour, 5 hours and 10 hours. After each 15 minutes of milling a pause of 30 minutes was introduced in order to reduce thermal effects. The total milling time of 1, 5 or 10 hours does not include the pauses. After milling, the bowl was opened in ambient conditions.

The obtained powders were characterized by powder X-ray diffraction (PXRD), scanning electron microscopy (SEM) and selected ones with thermogravimetric analysis (TGA) combined with differential thermal analysis (DTA). SnS_2 samples with 0, 10 and 20 wt. % graphite that were milled for 10 hours with 100 rpm, 200 rpm and 400 rpm were used for electrode preparation, coin cell assembly and electrochemical investigations using galvanostatic cycling under potential limitation (GCPL).

4.2 Thermal route

Mechanochemically prepared SnS_2 powder, which was milled for 10 hours with a rotation speed of 200 rpm, was mixed with polyvinyl alcohol (PVA, Sigma Aldrich) in a 1:1 mass ratio and homogenized using an agate mortar. The thermal treatment was performed in an Al_2O_3 crucible under argon flow (100ml/min) in a tube furnace system (MTI OTF-1200X). Prior to the thermal treatment, the furnace with sample was evacuated and flushed with argon once. Afterward, the tube furnace with sample was heated to a temperature of 500 °C with a heating rate of 2°C /min. This temperature was held for 1 minute, 2 hours, 5 hours, 10 hours, 15 hours as well as 20 hours. After the isothermal segment, the furnace was cooled down with a cooling rate of 5°C /min.

The obtained powders were characterized by powder X-ray diffraction (PXRD) and scanning electron microscopy (SEM). The sample that was heat treated for 15 hours was further electrochemically investigated using Galvanostatic cycling with potential limits (GCPL).

4.3 Cell assembly and electrochemical measurements

Electrodes were made from a mixture of active material (SnS_2, SnS_2-C composite or thermally treated SnS_2 material), carbon black super C45 (Imerys) conductive additive and Solef 5130 polyvinylidene fluoride (PVDF, Solvay) binder in weight ratio of 80:10:10. The electrodes were assembled at the Austrian Institute of Technology.

PVDF was dried at 80 °C for 12 hours in vacuum and then dissolved overnight in an n-methyl-2-pyrrolidone (NMP, Sigma Aldrich) solvent, forming a 5 wt. % solution. Prior to slurry preparation, the active materials were dried at 80°C for 12 hours in vacuum in a tube furnace (MTI OTF-1200X). After drying, the active material and carbon C45 were mixed in an agate mortar. To prepare the slurry, the 5wt. % PVDF in NMP solution was dropped into the prepared mixture of active material and C45 in order to maintain the 80:10:10 ratio of active material to conductive additive to binder. The resulting slurry was stirred for 12 hours at room temperature with a magnetic stirrer and coated onto copper foil using doctor blade (speed 2 mm/s) with a gap thickness of 60 µm. The electrodes were dried at 60 °C in air for one hour and then further dried in a vacuum oven at 80 °C for 12 hours afterwards to remove residual NMP.

Circular electrodes, with a diameter of 15 mm, were cut using a heavy-duty disc cutter, weighed, and dried again under vacuum in a heated flask (Büchi system) at 120°C for 12 hours. The electrodes were directly transferred in an argon-filled glovebox where coin cells in half-cell configuration were assembled. The loading of the electrodes was about 0.8-1 $mAhcm^{-2}$ and the coating thickness averaged 38 µm.

2016-type coin cells were constructed using Li metal (PI-KEM, 99.9 % purity) with a thickness of 0.6 mm as counter electrode, 75 µl soulbrain electrolyte (1 M $LiPF_6$ in 3:7 weight ratio of ethylene carbonate and ethyl methyl carbonate with 2 % vinylene carbonate additive) and 19 mm Celgard 2500 separator (polypropylene) with a thickness of 0.25 µm. The spacer had a thickness of 0.4 mm whereas that of the spring is 9 mm. The construction was done in argon atmosphere at the Austrian Institute of Technology. A schematic drawing of a coin cell is illustrated in Figure 13.

Figure 13: Illustration of a schematic coin cell. From bottom to top: bottom cap, Cu current collector coated with SnS_2 active material (cathode), separator, Li metal (anode), spacer, spring, top cap. Reproduced with permission from Albina Glibo.

Galvanostatic cycling under potential limitation (GCPL) tests were performed on a Maccor series 4000 battery tester in the potential range of 0.01 V to 1.8 V versus Li/Li^+ and with a specific current of 100 mAg^{-1} at the Austrian Institute of Technology. After 50 cycles, the cells were disassembled and the electrodes were washed twice using dimethyl carbonate (DMC) in an Ar-filled glove box. Further investigations of the electrodes were performed with post-mortem XRD in argon atmosphere at the University of Vienna and with post-mortem SEM at the Austrian Institute of Technology.

4.4 Characterization

X-ray diffraction (XRD) was performed on a Bruker D8 Discover with θ/2θ Bragg-Brentano geometry and a copper X-ray tube as a radiation source at the University of Vienna. The measurements were done with an acceleration voltage of 40 kV and an electric current of 40 mA. A Ni-filter was used to extinct Cu $K_ß$-radiation. The total measurement time for powders was 1 hour and 2 hours for ex-situ XRD electrodes under an airtight polycarbonate dome. Coin cells were disassembled in an argon filled glove box at the AIT and the electrodes were transferred to the University of Vienna in airtight tubes. Powders as well as electrodes were fixed with petroleum jelly onto a silicon monocrystal sample holder. Signals were recorded with a Lynxeye strip detector using the software Diffrac XRD commander for measurements. The resulting XRD-patterns where analyzed in terms of full-profile Rietveld refinements using Topas software from Bruker.

Scanning electron microscopy (SEM) was performed using a ESEM Zeiss Supra 55 VP instrument at the Austrian Institute of Technology. Powders were dispersed on a carbon conducting foil that was glued onto the sample holder. Gold sputtering was performed on the powder samples to prevent charge effects. Post-mortem electrodes were put directly onto the sample holder without gold sputtering and in argon atmosphere. The electrodes were transferred to the scanning electron microscope in a glass bottle that was sealed in the argon filled glove box. The acceleration voltage of the electron beam was 5 kV. Imaging was done with a secondary electron detector (SE).

Additional SEM measurements of powder samples were performed at the University of Vienna. The morphology was studied using a SEM Zeiss Supra 55 with in-lens detector collecting secondary electrons. The acceleration voltage of the electron beam was 5 kV. The powders were dispersed on a carbon conducting foil that was glued onto the sample holder.

Thermogravimetric (TG) measurements were done using a Setaram SETSYS Evolution system equipped with a TG/DTA transducer and S-type thermocouples (T_{max} =1600 °C) at the University of Vienna. The experiments were performed using Alumina Al_2O_3 crucibles that can be heated to 1600 °C [41]. The sample amount was averagely about 35 mg. SnS_2 samples, which were occasionally mixed with carbon, were heated from 30 °C to 1200 °C at a heating rate of 10 °C /min under synthetic air flow (20ml/min). The system was immediately cooled down to 30 °C with a cooling rate of 10 °C /min. The same crucible was heated up and cooled down twice for baseline correction. SnS_2 samples without carbon and with PVA were heated from 30 to 500 °C with a heating rate of 2 °C /min and held isothermal for 2, 5, 10, 15 and 20 hours under argon flow (20ml/min). After the isothermal step the system was cooled down to 30 °C with a cooling rate of 5 °C /min. Prior the measurement the system was evacuated and flushed three times. The whole experiment was done twice separately, once with the empty crucible and once with the same crucible and weighted sample. The empty crucible is the reference for baseline correction.

5 Experimental methods

5.1 X-ray diffraction

5.1.1 X-rays

X-rays are electromagnetic radiation with wavelengths in the range of few angstrom Å (10^{-10} m). This type of radiation was first described by Wilhelm Conrad Röntgen, who was awarded the first Nobel prize in physics in 1901 “in recognition of the extraordinary services he has rendered by the discovery of the remarkable rays subsequently named after him” [42]. The orders of magnitude of X-ray wavelengths roughly correspond to the range of atomic spacing in ordered solids.

X-rays are typically generated using an X-ray tube in the laboratory scale or alternatively using electron accelerator systems like a synchrotron. A schematic X-ray tube is illustrated in Figure 14.

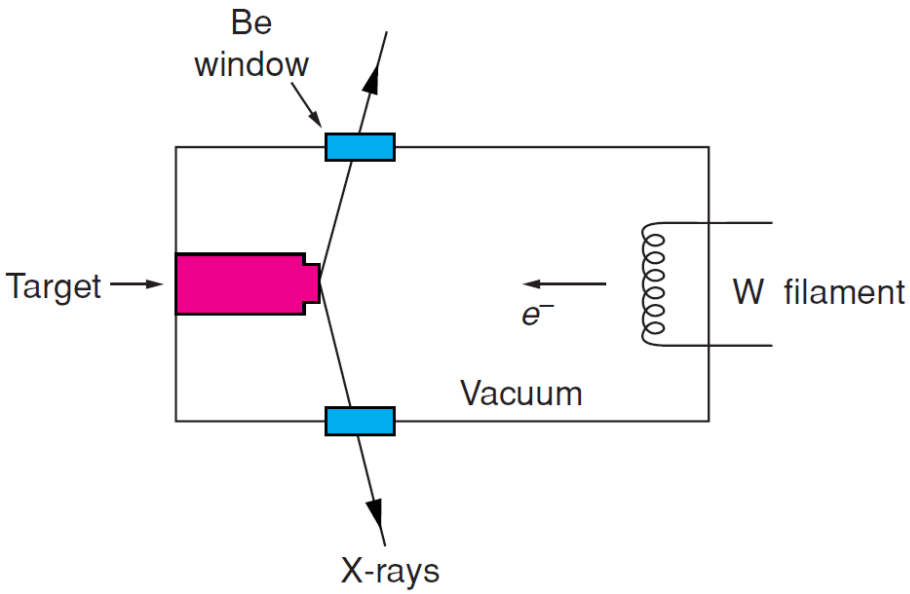

Figure 14: Schematic X-ray tube [43].

An electric field with a potential difference of about 30-40 kV is applied between two electrodes to accelerate electrons that are emitted by a heated electron gun. The cathode is usually a heated tungsten filament and the anode is a metal such as e.g., copper, molybdenum, or cobalt. The X-ray chamber is evacuated to avoid oxidation of the electrode materials and interactions of electrons and X-rays with gas species. When the electron beam hits the target metal, the kinetic energy of the electrons is converted into electromagnetic energy, emission of secondary electrons as well as heat energy. Due to the heat generation, the anode needs to be water cooled. The irradiated electrons can eject electrons from the inner orbitals and thus cause X-rays emission with characteristic wavelengths. The X-rays exit through a Be window to keep absorption effects low, since Be with atomic number 4 is the lightest appropriate material for this application [43].

The wavelength of X-rays is specified by the X-ray tube metal. They are in the range of a few Angstrom as mentioned before, for example 0.7107 Å (K_α for Mo), 1.5418 Å (K_α for Cu) and 1.3922 Å ($K_ß$ for Cu). During X-ray emission, an inner-shell electron 1s (K-shell) is ejected by an incident electron leaving a vacancy. During relaxation, an electron from an outer orbital

immediately occupies the vacancy, emitting its energy as an X-ray photon. Different wavelengths for the same metals are a result of the different electronic transitions that occur during relaxation. Transitions from the L-shell to the K-shell (2p→1s) result in the production of K_{α}-lines, which are split into the doublet $K_{\alpha 1}$ and $K_{\alpha 2}$-lines by spin-orbit interactions of the L-shell. Transitions from the M-shell to the K-shell (3p→1s) result in the emission of $K_{ß}$-lines [43]. Figure 15 illustrates the generation of X-rays using Cu as target metal as well as a typical X-ray emission spectrum.

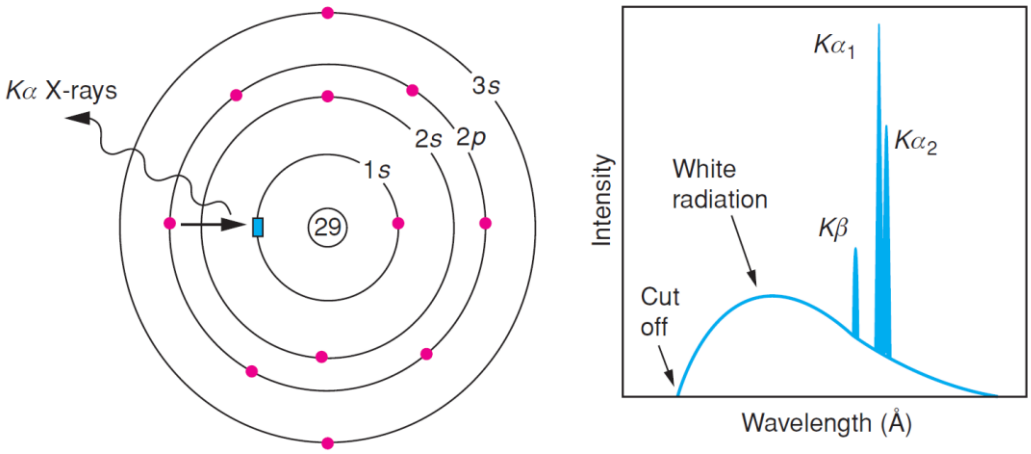

Figure 15: Left: schematic generation of X-rays from Cu target material. Right: schematic X-ray emission spectrum of Cu [43].

The X-ray emission spectrum not only contains the characteristic lines but also shows Bremsstrahlung, which is also known as white radiation with a continuous spectrum. Bremsstrahlung is produced when incident electrons are slowed down as they pass the nucleus. In general, a monochromatic X-ray beam is desired for diffraction experiments, therefore all effects besides the most intense $K_{\alpha 1}$-line need to be filtered out. $K_{ß}$ radiation is removable with a Ni-metal filter because nickel shows an X-ray absorption edge at 1.488 Å which lies between the K_{α} (λ = 1.5418 Å) and $K_{ß}$ (λ = 1.392 Å) X-ray emission lines of copper [43]. The further separation of the $K_{\alpha 1}$-line from the $K_{\alpha 2}$-lines requires a monochromator crystal (Si, C), which however, mandatorily reduces the intensity and can cause asymmetry of the diffraction signals. Therefore, especially powder XRD-patterns are often recorded with both K_{α} wavelengths what results in split diffraction signals which complicate the pattern, however, enhance the experimental information.

5.1.2 X-ray diffraction

Crystals are 3D arrangements of atoms with regularly repeating structures and a periodic electron density distribution with interatomic distances similar to the wavelength of X-ray radiation. The structure is described based on a unit cell, the smallest unit which contains full crystallographic information in terms of spacing and symmetry. The metric of the unit cell is described by the lattice parameters a, b, c and α, β, γ. Together with the occupation of the atomic positions the unit cell describes the atom arrangement. All symmetry operations applicable to a certain crystal structure are defined by its space groups. The space group symbols are abbreviations for the 230 groups of symmetry elements in 3D-space summarized in the International Tables for Crystallography [44].

During interaction of X-rays with a crystal, the atoms[1] act as secondary point sources and show a scattering effect [43]. W. Friedrich, P. Knipping, M. Laue described the effects of diffraction in 1912 leading to the postulation of the Laue equations [45].

$$\vec{a}\ \vec{s} = h$$

$$\vec{b}\ \vec{s} = k$$

$$\vec{c}\ \vec{s} = l$$

In these equations, h, k and l are integer numbers and integer multiples of the path difference. $\vec{s}$ is the scattering vector, whereas the vectors $\vec{a}\ \vec{b}\ \vec{c}$ describe the orientation of the crystal and span the crystal lattice. Each equation corresponds to one of the three crystallographic axes in a crystal. Diffraction only occurs when all Laue equations are fulfilled and constructive interference takes place (Laue conditions). When the Laue conditions are not fulfilled, destructive interference occurs and no diffracted signal is detected. Each triplet (h k l) describes one unique reflection of the diffraction pattern, respectively one crystallographic plane, also called miller indices [43].

In a second approach, Bragg described an alternative way to represent the same coherences and phenomena as illustrated in the Laue equations. Bragg's solution is the simpler and more universal to use. Bragg's approach is illustrated geometrically in Figure 16.

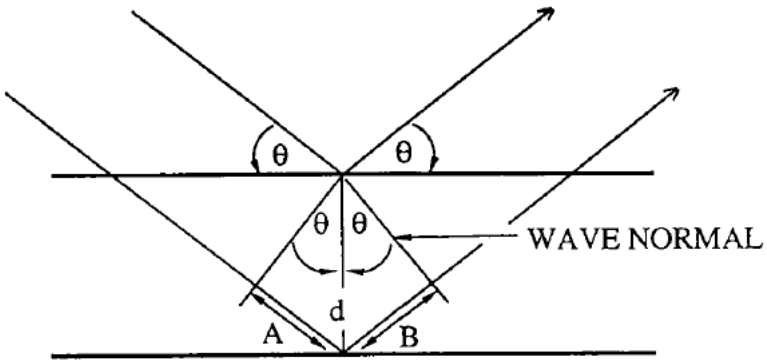

Figure 16: Geometric illustration of Bragg's law [46].

[1] The electrons mainly interact with X-ray photons. Nevertheless, the atoms can be considered as scattering centers.

A crystal can be considered as built up from layers of crystal planes that show properties like semi-transparent mirrors. Horizontal lines represent crystal planes, where d is the distance between these planes. Some X-rays are reflected, where the angle of reflection equals the angle of incidence, whereas the rest of the X-rays is transmitted. The angle θ is also called the Bragg angle. The second beam (left one) must travel the additional distance A+B compared to first beam (right one) to be in-phase. For constructive interference, the distance A+B has to be an integer multiple of the incoming wavelength. Consequently Bragg's law reads as follows [47]:

$$2\, d_{hkl} \sin\theta = n\, \lambda$$

When Bragg's law is fulfilled, constructive interference occurs and the reflected beams are in-phase. The interplanar d-spacing is also called resolution and it is possible to calculate the lattice parameters from d and vice versa depending on the crystal system (cubic, hexagonal, trigonal, tetragonal, orthorhombic, monoclinic and triclinic). θ is the angle of the incident X-ray beam and λ the wavelength of the X-ray radiation used. In general, there are several possible solutions of Bragg's law due to the fact that n is any integer number. However, it is common to set n to 1 and modify the d-spacing by multiples of the miller indices, e.g. the plane (2 2 2) corresponds to the second order (n=2) interference of (1 1 1) with half d-spacing [43].

Up to this point, no information is known about the atom types, only about their interspacing. As mentioned above, atoms behave like secondary point sources for X-rays during scattering after interactions with the incident X-ray beam. During the interaction event, electrons are set into vibration and scatter in-phase in direction of the incident beam. In total, the X-rays scattered by the atoms are the sum of interfering waves scattered by every occurring electron. For this reason, the atomic scattering factor f is proportional to the number of electrons of a specific element. When θ equals zero, the atomic scattering factor corresponds to the atomic number of the atom [48]. Atomic form factors for different elements as a function of angle and X-ray wavelength are illustrated in Figure 17.

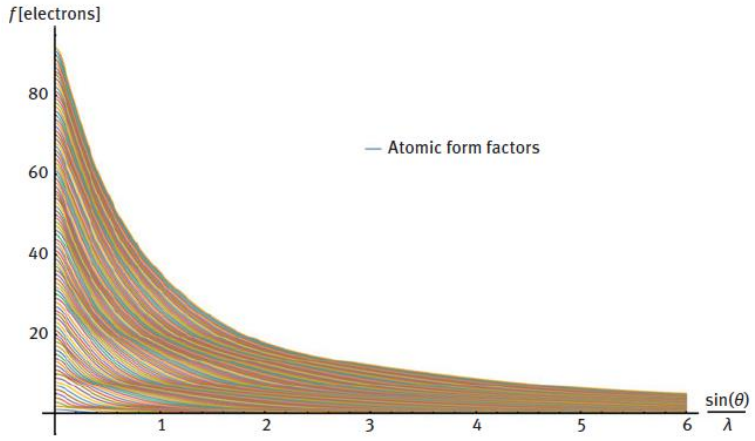

Figure 17: Atom scattering factors for different elements as function of sin(θ)/λ [48].

One can see a gradual decrease in intensity with increasing X-ray incidence angle and decreasing wavelength due to greater cancellation of the phase differences of the exiting beam. The atom form factor can be written as:

$$f = f_0\, e^{(-B \sin^2\theta\, /\, \lambda^2)}$$

Where f is the scattering factor under experimental conditions, f_0 is the scattering factor at a temperature of 0 K and B is the Debye-Waller factor to model thermal motion and vibrations. B can be modeled isotropically for spherical particles or anisotropically for more precise experiments.

When looking at scattering by a crystal, each set of planes can result in a diffracted beam. Where the intensity of the diffracted beam from a given plane is zero, destructive interference is shown. Therefore, valuable information is still generated due to systematic absences. To model a general crystal, the individual waves produced by atoms need to be summerized to result in a diffracted beam intensity, whereby phase and amplitude must be considered.

The so-called structure factor F for a specific reflection (hkl) can be written as [46]:

$$F(hkl) = \sum_j n_j f_j \cos\left[2\pi\left(h\,x_j + k\,y_j + l\,z_j\right)\right]$$

Where j is any atom in the unit cell and x, y, z are the fractional coordinates of the atomic position in the unit cell. A graphical illustration of the complex structure factor as vector sum of the individual atomic form factors is shown in Figure 18.

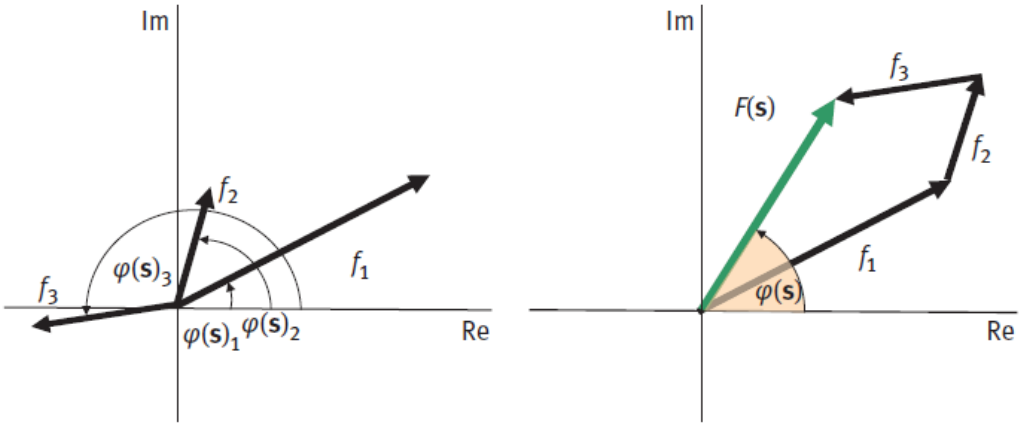

Figure 18: Illustration of complex structure factor as vector sum of individual atom form factors [48].

The intensity of the diffraction radiation I_{hkl} is proportional to the squared structure factor $|F_{hkl}|^2$.

$$I(hkl) \propto |F(hkl)|^2$$

This results in the so-called phase problem of crystallography. While amplitudes of wave functions can be calculated from intensities, their phase angles cannot, so information is lost. As only intensities are detected, phase angles must be determined with other methods like the Patterson method, Fourier method or direct method [43]. However, these advanced crystallographic techniques are not needed in the scope of this master thesis and are therefore not explained in more detail.

5.1.3 X-ray powder diffraction

During X-ray powder diffraction (XPD) experiments, a powdered sample is penetrated by monochromatic X-rays. A powder consists of randomly oriented crystallites and therefore there are lattice planes statistically in every possible orientation. In such a way there are always hkl planes fulfilling Braggs law. Requirement for diffraction is that the respective plane is positioned at a valid Bragg angle θ to the incident beam. The angle between diffracted and not diffracted beam is 2θ and the total angle of the cone is 4θ [43]. This results in circle shaped (surface of a cone) signal for each diffraction angle because the crystal planes can have different spatial orientations all fulfilling Braggs law. Figure 19 shows the formation of such cone from a diffracted X-ray beam after interaction with a powdered sample.

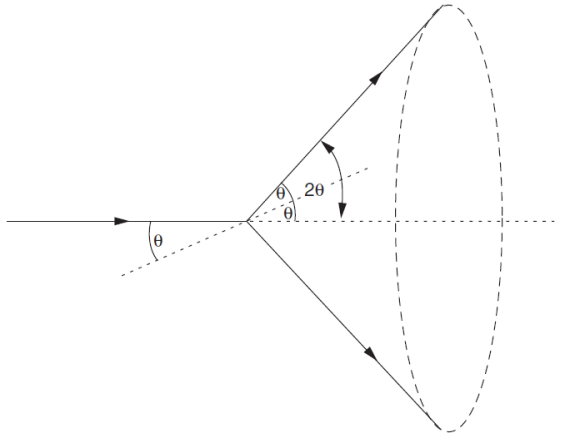

Figure 19: X-ray powder cone [43].

Due to the lack of X-ray lenses, the circle theorem is instead applied to focus and converge the beam. The arrangement of the source of X-rays, the measured sample and the detector is illustrated in Figure 20.

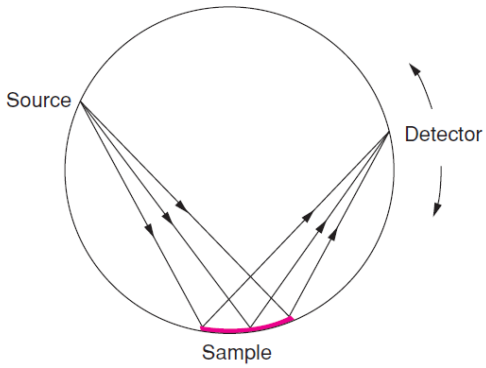

Figure 20: Circumference alignment of source, sample and detector [43].

Depending on the respective instruments, either the source and detector (θ/θ-geometry) can move or the sample and detector (θ/2θ-geometry or Bragg-Brentano geometry) can move during measurement. Conventional detectors for powder-XRD are scintillation counters, solid state detectors and one-dimensional strip detectors.

Higher symmetry crystals show simpler powder patterns compared to crystals with lower symmetry at comparable unit cell sizes. A cubic primitive cell of small size shows less reflections compared to a face centered cell of large size. Crystals are usually randomly oriented in a prepared powder sample; when the powder particles are far to be centrosymmetric, e.g. platelets or needles, preferred orientation has to be taken into account. Generally, PXRD is a powerful technique to identify crystalline phases but it can be quite difficult to solve unknown structures using since diffraction signals of all crystal planes with the same d-spacing, regardless of their crystallographic orientation, unify at one diffraction angle. Therefore single crystal X-ray diffraction, which represents the full reciprocal space may be used for crystal structure determination [43][48].

5.1.4 Rietveld Refinement

The Rietveld refinement method was developed by Hugo Rietveld [48] and compares experimentally measured XRD patterns with calculated profiles using adjustable parameters. It fits the measured data using the least-square method to confirm structural details of powder samples. Structural information is available from different databases like e.g. Inorganic Crystal Structure Database (ICSD), which was used in this thesis. Alternatives are the Cambridge Structural Database (CSB) for small organic and organometallic molecules or the Protein Data Bank (PDB) for proteins.

R-values are used for judgment of the quality of a Rietveld refinement. The R value is a calculation of the differences between the measured and calculated profile and is therefore a measure of their agreement. The weighted R-value and the expected R-value are calculated using following equations:

$$R_{wp} = \sqrt{\frac{\sum_{i=1}^{N} w_i \left(y_{obs,i} - y_{calc,i}\right)^2}{\sum_{i=1}^{N} w_i y_{obs,i}^2}}$$

$$R_{exp} = \sqrt{\frac{N - P}{\sum_{i=1}^{N} w_i y_{obs,i}^2}}$$

Where N is the number of data points in the pattern and P the number of used parameters. R_{exp} is also considered as the best possible R-value based on an ideal model to describe the diffraction pattern. The ratio of the weighted R-value to the expected R-value is called goodness of Fit (GOF) and is an indicator for the quality of the Rietveld refinement [48].

$$\chi = \frac{R_{wp}}{R_{exp}}$$

5.2 Scanning electron microscopy

The general aim is to overcome the Abbe limit, which defines the limit of resolution for microscopy using an optical light source and attain higher magnifications. This can at one hand be achieved by a shorter wavelength of the incident beam as it was realized using electron beams in transmission electron microscopes. Another way is to scan the object in a raster point for point with an appropriate detector. The idea of scanning optical microscopy was developed by Synge in 1928. Stintzing first proposed the usage of an electron beam in a scanning device in 1929 and the first scanned images using an electron beam were published by Knoll in 1935. However, it took over 30 more years until the first commercialized scanning electron microscope (SEM) was sold by the Cambridge Instrument Company in 1965 [49]. A schematic SEM setup is illustrated in Figure 21.

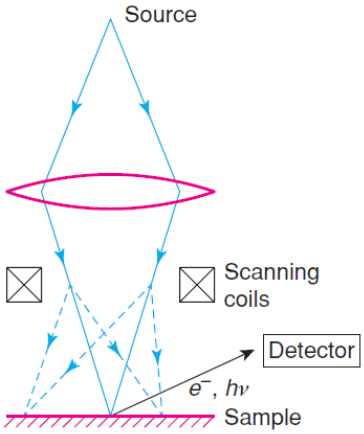

Figure 21: Schematic scanning electron microscope (SEM) [43].

Electrons are emitted by a heated cathode, which is also called the electron gun (similar to X-ray tube). Examples of electron guns are tungsten hairpin filaments, lanthanum hexaboride filaments and field emission guns. The latter is not heated during usage and therefore also called “cold cathode emitter”. All systems can only be operated in vacuum atmosphere. Primary electron beams have energies in the keV range with de-Broglie wavelengths that are fractions of nanometers and therefore several orders of magnitude smaller than those of visible light. Electromagnetic optics and condenser lenses guide and focus the electron beam onto the sample surface that is scanned in a defined area. During interactions of the electron beam with the sample surface, penetration of the specimen occurs, thereby leading to a pear-shaped interaction volume. The dimensions of the interaction volume is defined by the energy of the electron beam, its incident angle and the elements in the sample. The higher the electron beam energy as well as the incident angle and the lower the atomic mass the higher the penetration depth. Due to the interaction of the electron beam with the sample, fluorescence X-rays, characteristic X-rays, Bremsstrahlung and Auger electrons, back scattered and secondary electrons are produced, which can all be detected with different detectors [50]. Also electron back scatter diffraction (EBSD), which provides crystallographic information can be measured in such instruments.

During the interaction of the electrons of the electron beam with those of the atoms in the specimen, a change in momentum as well as a change in energy can occur. Therefore, the electrons can scatter elastically and inelastically. During elastic scattering, the direction of the electrons changes while the energy is kept constant. In comparison, a change of electron energy takes place during inelastic scattering [51].

SEM provides information about surface topography, chemical composition, crystalline structure and electrical behavior of roughly the first micron of the sample. Back scattered electrons (BSE) and secondary electrons (SE) are mainly used for imaging. During imaging, every scanned point corresponds to one point on the reproducing screen and/or micrograph. SE are produced by inelastic scattering of primary electrons by electrons in the atomic shell of the sample and give the highest spatial resolution due to their production close to the surface. Therefore, SE are mainly used for topography investigations. Energies of SE are typically not higher than 50 eV and are therefore much lower compared to the energy of the electrons of the primary electron beam (keV range). BSE are primary electrons that exit the sample again after elastic and inelastic interactions. These primary electrons interact with different numbers of electrons depending on the atomic number of the elements in the sample. The higher the atomic number of the sample, the higher the number of BSE. Higher atomic numbers give a brighter region in the SEM graph and lower atomic numbers give a darker region in the SEM graph. This is called atomic-number contrast [50].

The pear-shaped volume as well as the schematic difference of depth for SE and BSE are illustrated in Figure 22.

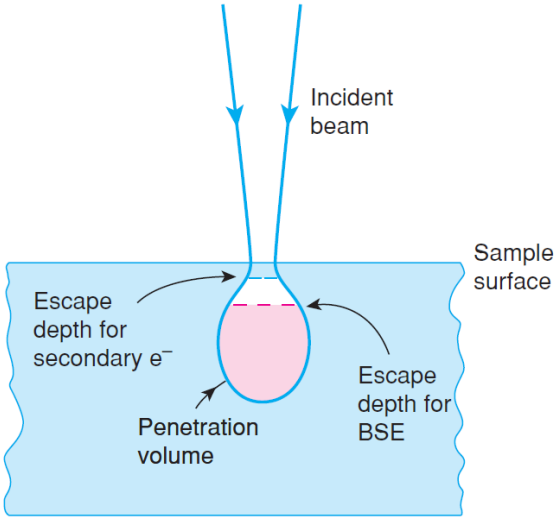

Figure 22: Schematic specimen - electron beam interaction [43].

The systems mentioned so far only allow qualitative analysis and topography investigations, while more sophisticated electron microprobe analysis (EPMA) systems using energy-dispersive X-ray spectroscopy (EDX) detectors or wavelength-dispersive X-ray spectroscopy (WDX) detectors also allow quantitative analysis.

In all cases, the samples to be examined must be clean, dry and electrically conductive. Therefore, a sample preparation step may be necessary, in which a conductive layer is deposited onto the surface of the specimen. The latter is not required for semiconductors and metallic systems [51]. It has to be mentioned that samples and their structures to be observed need to withstand the ultrahigh vacuum ($<10^{-8}$ mbar) in the microscope chamber.

5.3 Thermogravimetric analysis and difference thermal analysis

Thermal analysis (TA) broadly describes the measurement of physical and chemical properties as a function of temperature. In thermogravimetric analysis (TGA) and difference thermogravimetry (DTG), the change in the mass of a sample is measured as a function of time and/or temperature. In difference thermal analysis (DTA), the temperature difference between a sample and reference material as function of time and temperature is monitored. In DTA, the measured value is a voltage signal of a thermopair or thermopile, taking advantage of the fact that a temperature difference in a thermoelement, that consists of two different metals, leads to a change in voltage aproportional to the Seebeck effect [43].

Thermobalances as used in TGA are constructed as top loading, hang down or horizontal arrangements. Figure 23 illustrated different designs and constructions of thermobalances [41].

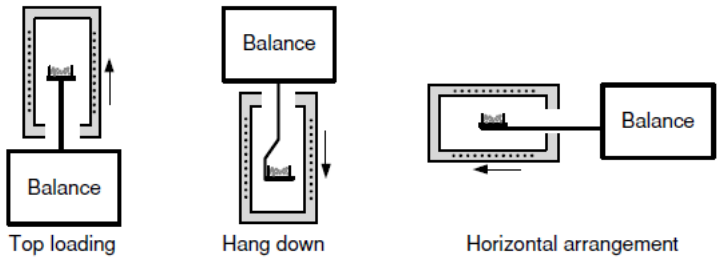

Figure 23: Thermobalance designs [41].

Figure 24 shows a schematic TG curve with mass loss for increasing temperature.

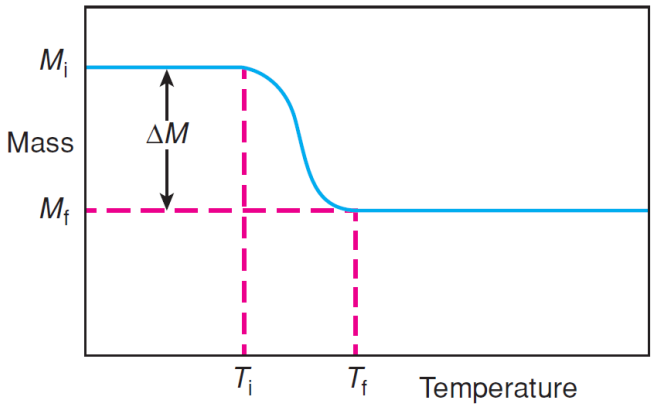

Figure 24: Schematic TG curve [43].

In Figure 21, M_i and M_f are the initial and final masses of the samples, respectively. In a well-conducted experiment, $\Delta M/M_i = (M_f - M_i)/ M_i$ should be a fundamental property of a sample and therefore not depend on the experimental conditions. The values of T_i and T_f are related to the heating rates and other influencing properties like particle size [43].

In general, the mass of the sample changes when a loss of material or reaction with the atmosphere during the measurement take place. Steps in TGA are shown as peaks in the DTG curve. A sample may lose or gain mass due to the evaporation of volatiles (e.g. water or other solvents), oxidation reactions, thermal decomposition and heterogenous chemical reactions. Simultaneous TGA/DTA benefits from the generation of both thermogravimetric and differential

temperature signals in the same experiment [41]. A simultaneous experiment performing DTA and TG is illustrated schematically in Figure 25.

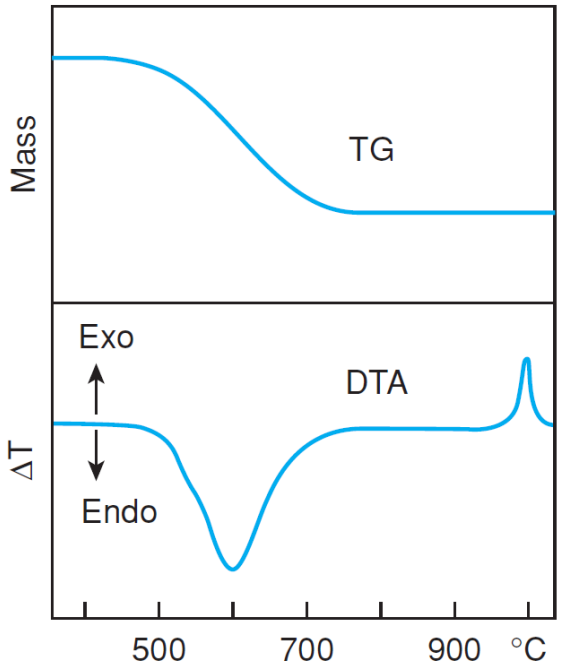

Figure 25: Schematic TG and DTA curves [43].

The point of inflection of the TG curve agrees in most cases with the peak maximum of the DTA curve and the corresponding temperature is that where the rate of mass change has its maximum. The direction of the DTA curve depends whether the effect is endothermic (e.g., thermal composition) or exothermic (e.g., oxidation) [52].

6 Results and discussion

6.1 Mechanochemical route

6.1.1 Sample preparation und evaluation

Preliminary ball-milling experiments were d in order to establish a baseline set of parameters for the further investigations. Since carbon is expected to change the general milling behavior of the materials, the first pre-investigations were performed on mixtures of SnS_2 and graphite. In these tests, a mixture of SnS_2 with 10 wt. % graphite was prepared and homogenized with an agate mortar. The samples were then milled in argon atmosphere for 1, 5 and 10 hours with rotation speeds of 100, 200 and 400 revolutions per minute. Milling was performed in steps of 15 minutes, followed by a 30-minute pause, until the total milling time (1, 5, or 10 hour) was attained. SEM micrographs of the milled SnS_2/10C samples are shown in Figure 26.

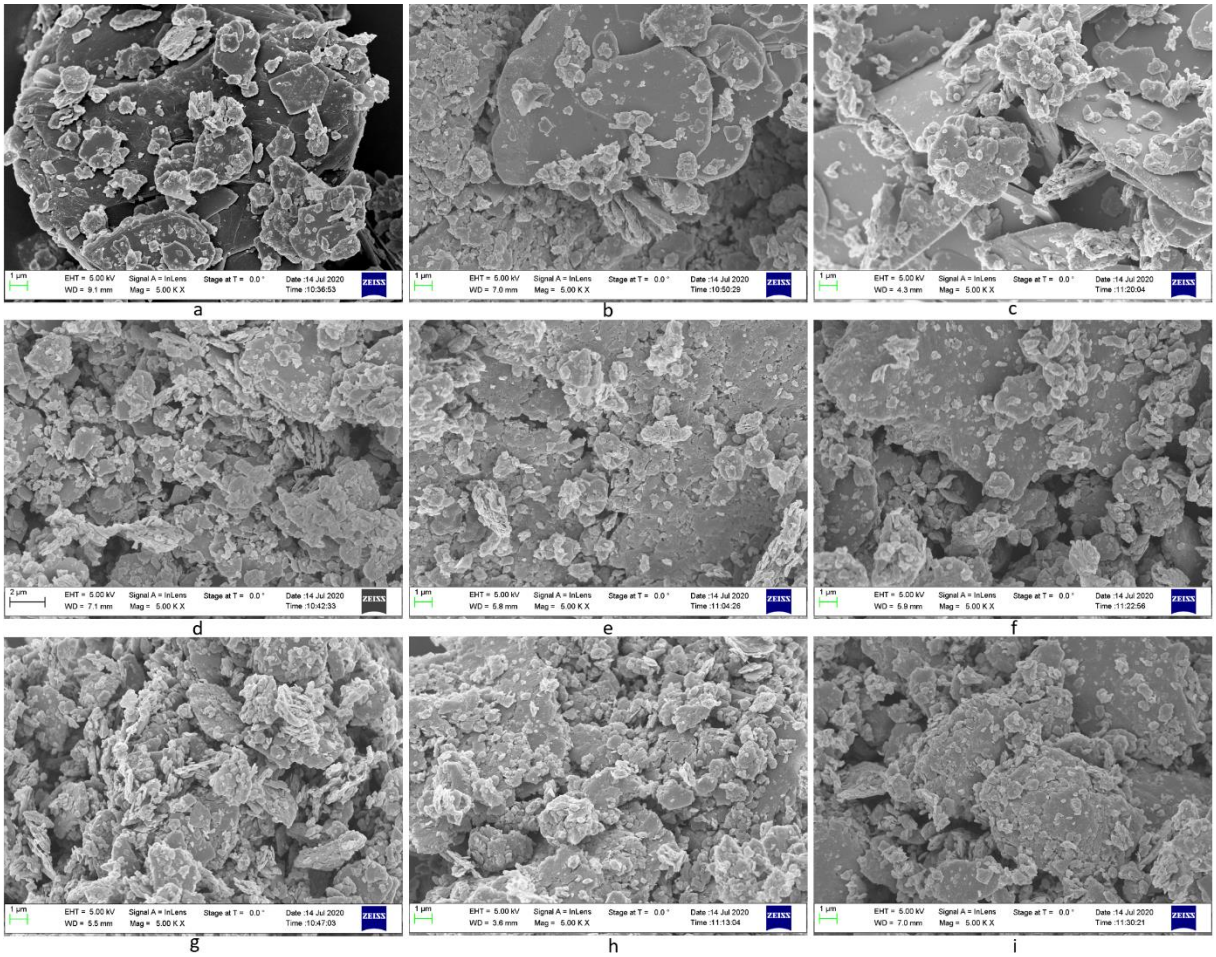

Figure 26: SEM evaluation of rotation speed and milling time. SnS_2 powders with 10 wt. % graphite. Performed milling parameters were a)1h 100 rpm b) 1h 200 rpm c) 1h 400rpm d) 5h 100 rpm e) 5h 200rpm f) 5h 400 rpm g) 10h 100 rpm h) 10h 200 rpm and i) 10h 400 rpm.

The SEM images show that after 1 hour milling at the different the rpm values, the microstructure of the samples is not homogenous and large particles surrounded by smaller ones can be observed. However, the powder microstructures after 5 and 10 h of milling at 200 and 400 rpm appear to be more compact. The degree of compaction seems to increase when a milling time of 10 hours is used. In general, it is very difficult to distinguish between the microstructures of SnS_2 and graphite particles in the SEM micrographs since both layered structures form platelets. Based on these preliminary investigations, a total milling time of 10

hours was selected for further studies. Revolutions of 100rpm, 200rpm and 400rpm per minute seemed suitable.

After the preliminary tests, both SnS_2 and graphite were separately milled at 100, 200 and 400 rpm for 10 hours, in order to investigate the effect of the milling parameters on the morphology and phase constitution of the pure powders. Figure 27 illustrates the measured PXRD patterns of pristine and mechanochemical treated graphite as a function of milling speed.

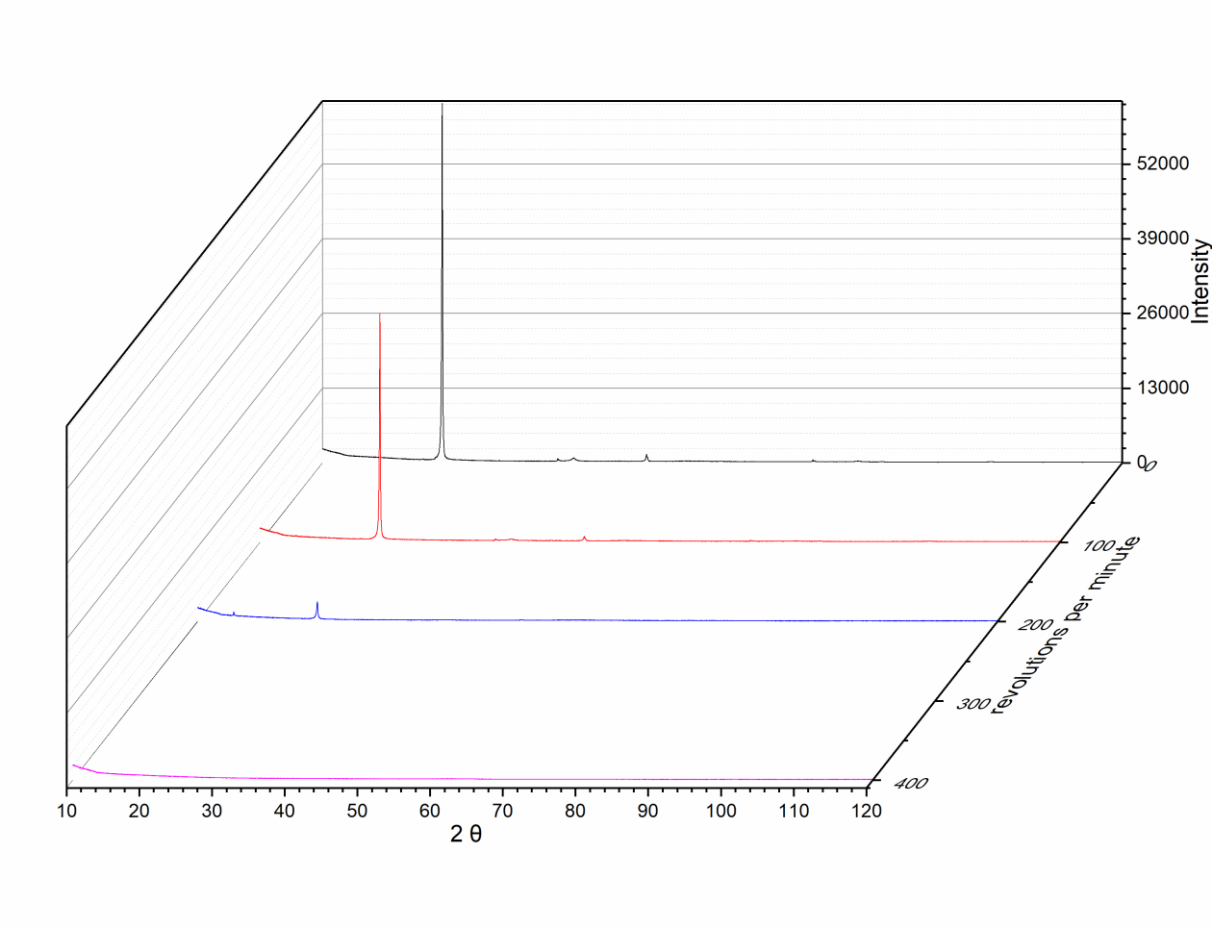

Figure 27: Measured PXRD patterns of pristine and ball milled graphite dependent on different rotation speed.

One can see a decrease in intensities with increasing rotation speed and strong preferred orientation in the [0 0 1] direction. Interestingly, there are no detectable peaks after applying ball milling for 10 hours at 400 rpm, indicating that an amorphous phase has formed. Table 4 summarizes the results of the Rietveld refinement of the PXRD measurements of graphite including the lattice parameters and average crystal sizes prior to and after ball milling for 10 hours at 100, 200 and 400 rpm.

Table 4: Results of the Rietveld refinement of pristine graphite and graphite, which was milled at 100, 200 and 400 rpm for 10 hours.

				Lattice parameters [Å]		
sample	**phase**	**space group**	**Average crystal size [nm]**	**a**	**c**	**R_{wp}**
graphite MCMB pristine	graphite 2H	P63/mmc	129	2.461(1)	6.719(2)	12.357
graphite 10h100rpm	graphite 2H	P63/mmc	111	2.461(2)	6.712(1)	9.759
graphite 10h200rpm	graphite 2H	P63/mmc	54	2.50(1)	6.724(5)	8.532
graphite 10h400rpm	amorphous					

No significant changes are observed between the lattice parameters of pristine graphite and those after ball milling for 10 hours at 100 rpm whereas a significant enlargement of the cell can be observed at 200 rpm. In general, the average crystal size decreases with increasing number of revolutions per minute, eventually no crystalline structures are detected after milling with 400 rpm for 10 hours.

The SEM micrographs of SnS_2 powders in pristine form and after the mechanochemical treatment with different revolutions per minute are shown in Figure 28. Pristine SnS_2 platelets show sharp edges that appear rounded after milling for 10 hours at 100 rpm. Additionally, particles of significantly smaller size are distributed between the large platelets with rounded edges at 100 rpm, and the degree of agglomeration is less than in the pristine sample. Further increases in rpm lead to particle size reduction and the formation of primary nano particles which tend to agglomerate. According to the micrographs, the primary particles are smaller at 400 rpm compared to those at 200 rpm.

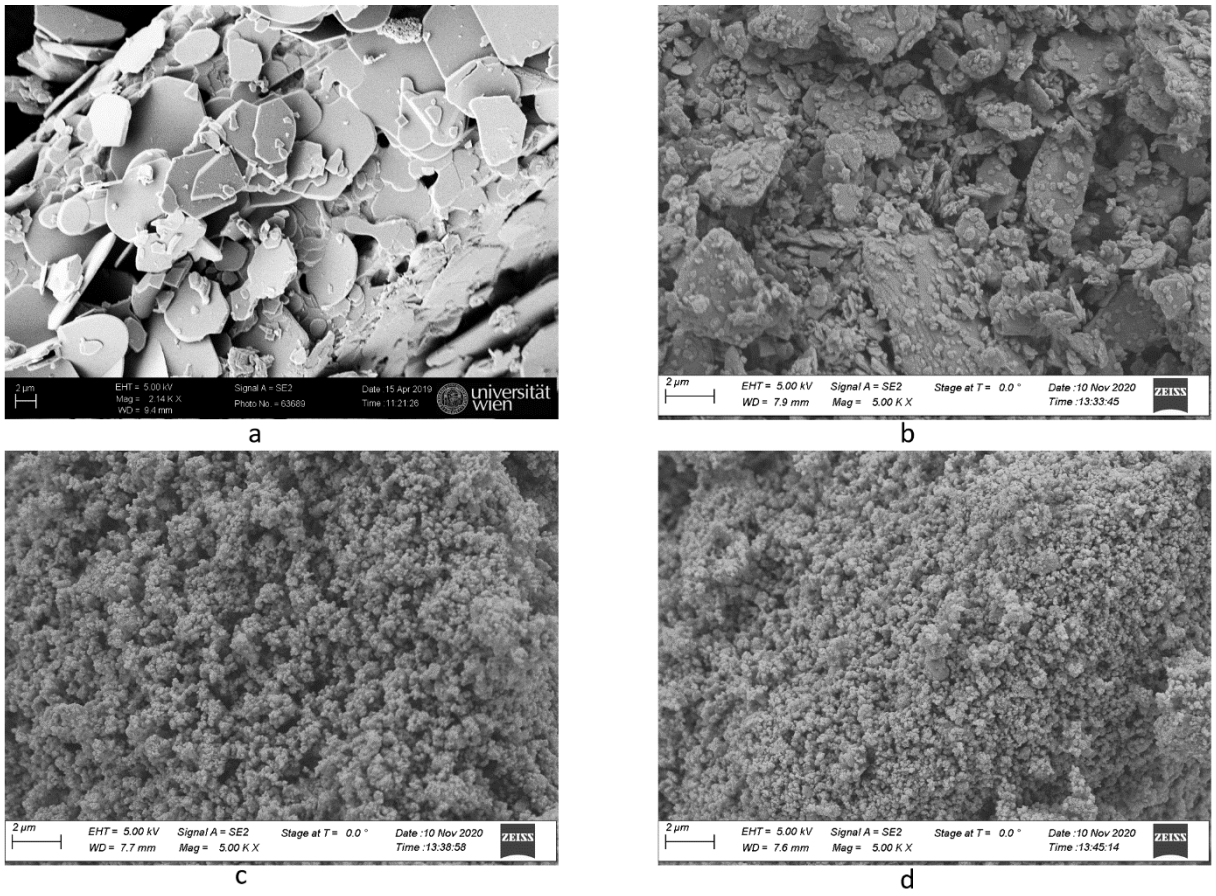

Figure 28: SEM SnS_2 powder samples a) pristine b) BM 10h 100 rpm c) BM 10h 200 rpm d) BM 10h 400 rpm.

The four different SnS_2 powder samples were additionally characterized by PXRD. Figure 29 to Figure 32 show the XRD-patterns of the SnS_2 samples in pristine form and after mechanochemical treatment for 10 hours at 100, 200 and 400 rpm and illustrate the phase transformation effects implemented via ball-milling.

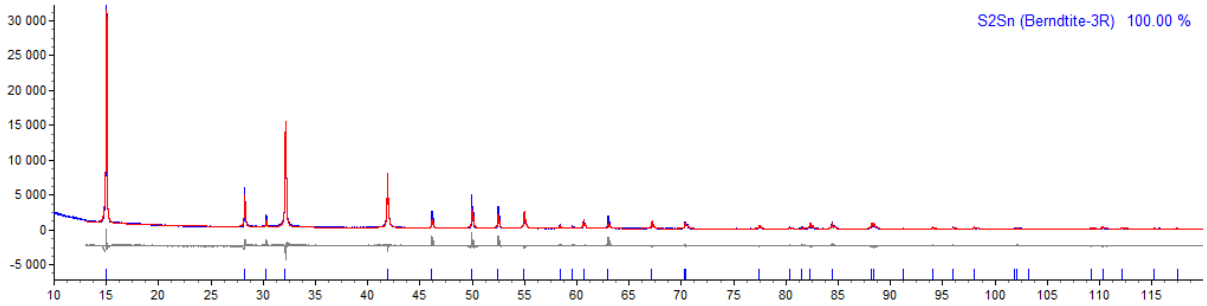

Figure 29: XRD-pattern SnS_2 pristine from MKNano.

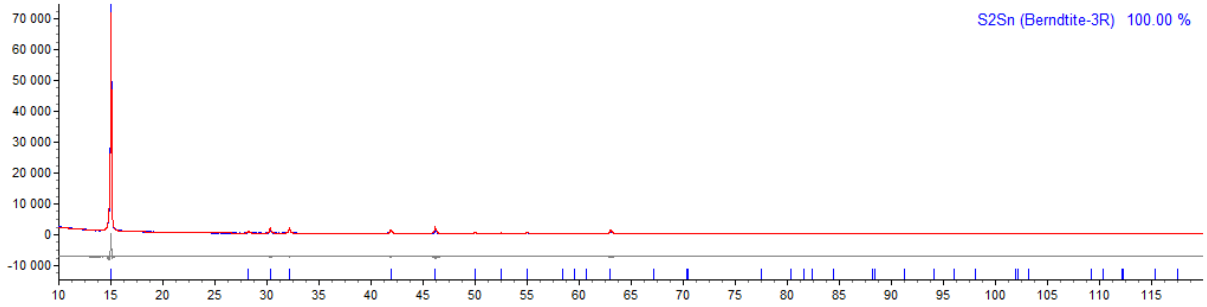

Figure 30: XRD-pattern SnS_2 after ball milling for 10 hours at 100 rpm.

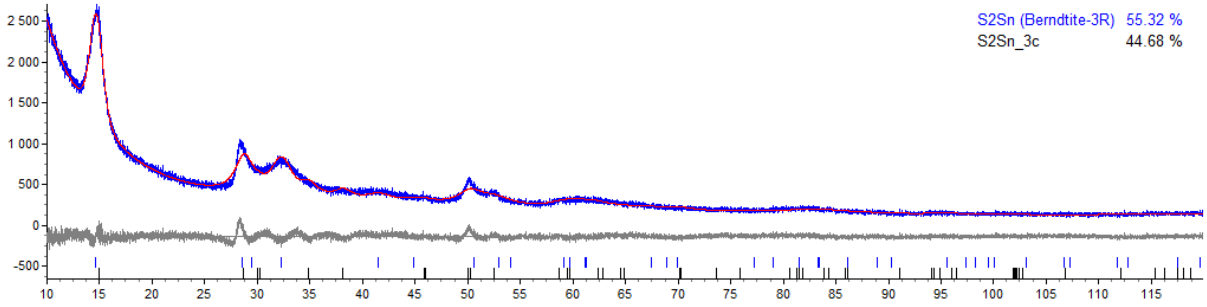

Figure 31: XRD-pattern SnS_2 after ball milling for 10 hours at 200 rpm.

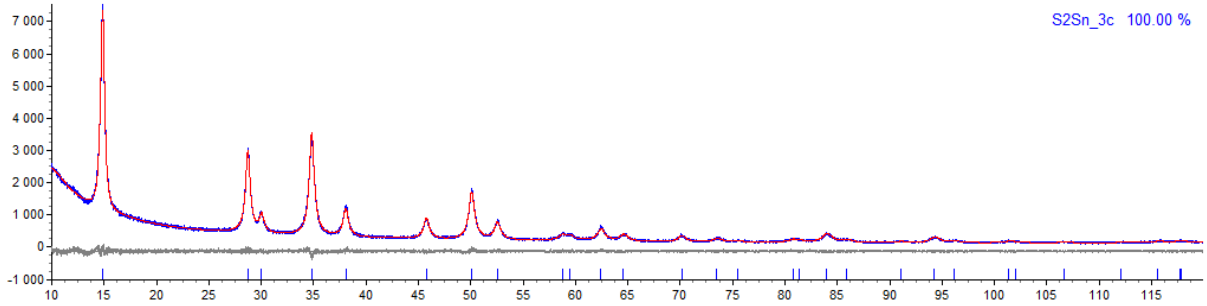

Figure 32: XRD-pattern SnS_2 after ball milling for 10 hours at 400 rpm.

All XRD patterns show strong preferred orientation in the [0 0 1] direction as evidenced by the dominant peak at 2θ=15° corresponding to the (001) reflex; its relative intensity is significantly higher than expected from the structure factor. At 100 rpm, although the original SnS_2 structure is retained, there is an even increased preferred orientation in the [0 0 1] direction after milling. At 200 rpm, however, the measured peaks for SnS_2 become broader with less intensity, and new peaks also appear. At 400 rpm, no diffraction lines of the pristine SnS_2 could be observed anymore but a new powder pattern appeared.

Table 5 lists the phases including lattice parameters and average crystallite sizes of the powder samples after mechanochemical treatment for 10 hours at 100, 200 and 400 rpm, respectively. Following treatment for 10 hours at 100 rpm, SnS_2 reveals only a minimal change in its lattice parameters and no significant changes in the average crystallite size (234 nm) compared to pristine SnS_2 (209 nm). The sample at 200 rpm is clearly less crystalline than the other powder samples, as indicated by the significantly broader peaks in its PXRD pattern. The Rietveld refinement of the PXRD pattern of the sample after milling for 10 h at 400 rpm was somewhat problematic as no suitable model structures were available in the ICSD. However, the peak positions of the pattern could be indexed and fit with a hkl-phase in TOPAS which revealed a trigonal rhombohedral unit cell with similar a-parameter and tripled c-parameter compared to the pristine SnS_2. A so-called cell search in the ICDS data base could identify $CdCl_2$(3R) as a structure with similar lattice spacing and same space group. The distribution of the Sn- and S-atoms according to this structure type resulted in a structure phase which allowed us to refine the present XRD powder pattern (400 rpm, 10 h) in TOPAS with excellent quality. It may be a metastable phase induced by mechanical stress. Its average crystallite size is 151nm. The sample that was ball milled for 10 hours at 200 rpm shows a mixture of SnS_2 and SnS_2_3c and a significant decrease in average crystallite size compared to all other samples.

Table 5: Results of the Rietveld refinement of pristine SnS_2 and SnS_2, which was milled at 100, 200 and 400 rpm for 10 hours.

					Lattice parameters [Å]		
sample	**phase**	**amount [%]**	**space group**	**Average crystal size [nm]**	**a**	**c**	**R_{wp}**
pristine	SnS_2	100	P-3m1	209	3.6485(4)	5.8982(9)	12.77
10h100rpm	SnS_2	100	P-3m1	234	3.648(1)	5.899(1)	10.475
10h200rpm	SnS_2	56	P-3m1	6	3.60(3)	6.05(9)	6.467
	SnS_2_3c	44	R-3m	3	3.65(3)	17.740(2)	
10h400rpm	SnS_2_3c	100	R-3m	151	3.641(1)	17.837(8)	4.935

These powders were further electrochemically investigated, and the results are shown in subchapter 6.1.5. A comparison of the crystal structure types of different polytypes is given here.

6.1.2 SnS_2 Polytype

Figure 33 illustrates the crystal structure of the newly found polytype of SnS_2_3c, which was detected after performing ball milling at 400 rpm on the pristine SnS_2 powder for 10 hours.

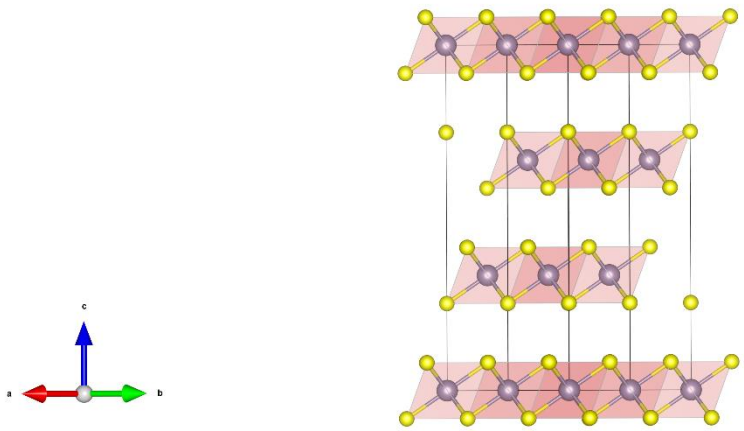

Figure 33: SnS_2_3c polytype structure.

Sn atoms are illustrated as silver spheres, whereas S atoms are yellow spheres. The polytype SnS_2_3c belongs to space group R-3m and shows a different stacking sequence compared to Berndtite SnS_2. Figure 34 illustrates the crystal structure of Berndtite SnS_2.

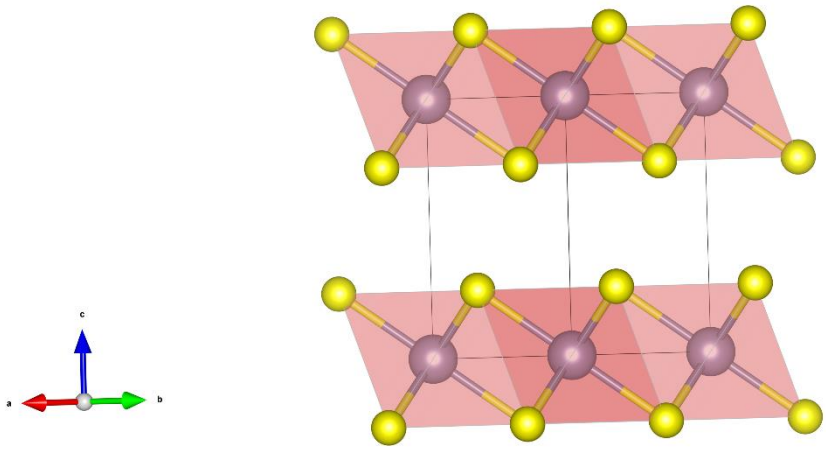

Figure 34: SnS_2 Berndtite structure.

SnS_2 Berndtite exhibits a CdI_2 structure which belongs to space group P-3m1. The structure was already explained in detail in subchapter 3.1., according to Ramsdell [20] notation for polytypes it is 2H-SnS_2 since the sulfur layers show ABAB…. stacking along [0 0 1]. Every second S-layer and all Sn-layers are congruent and accordingly, the triple layer units S-Sn-S are congruently stacked. However, in the newly found polytype structure, only every fourth S-

Sn-S unit is congruent resulting in a triple c-parameter. According to the ABC-αβγ notation [21] for S-and Sn-atoms the stacking sequence is (AγB)(CβA)(BαC) what results in a rhombohedral symmetry. The Ramsdell notation is 6R-SnS_2. Since lithium is known to occupy the octahedral and tetrahedral interstitial sites in the crystal structure, another lithiation mechanism can be expected for the 6R-SnS_2 polytype compared to that for 2H-SnS_2 one. Therefore, the electrochemical lithiation process of the 3R-SnS_2 polytype is further investigated in the next subchapter by performing discharge with a low specific current of 2.5 $mAhg^{-1}$ to simulate quasi-equilibrium conditions and investigate the respective crystal structure via ex-situ XRD with full-profile Rietveld refinement of the electrodes XRD-patterns.

6.1.3 Equilibrium discharge curve

Experiments were conducted to examine the electrochemical response and discharge curves of the intercalation reaction of lithium into the various SnS_2 host structures after ball milling at 100, 200 and 400 rpms. Figure 35 illustrates the measured discharge curves up to a specific capacity of 350$mAhg^{-1}$ for electrodes that were made from SnS_2 following ball-milling. One plateau is seen for the 100 rpm sample, whereas the 400 rpm sample shows multiple plateaus and the 200 rpm sample a continuous drop in potential.

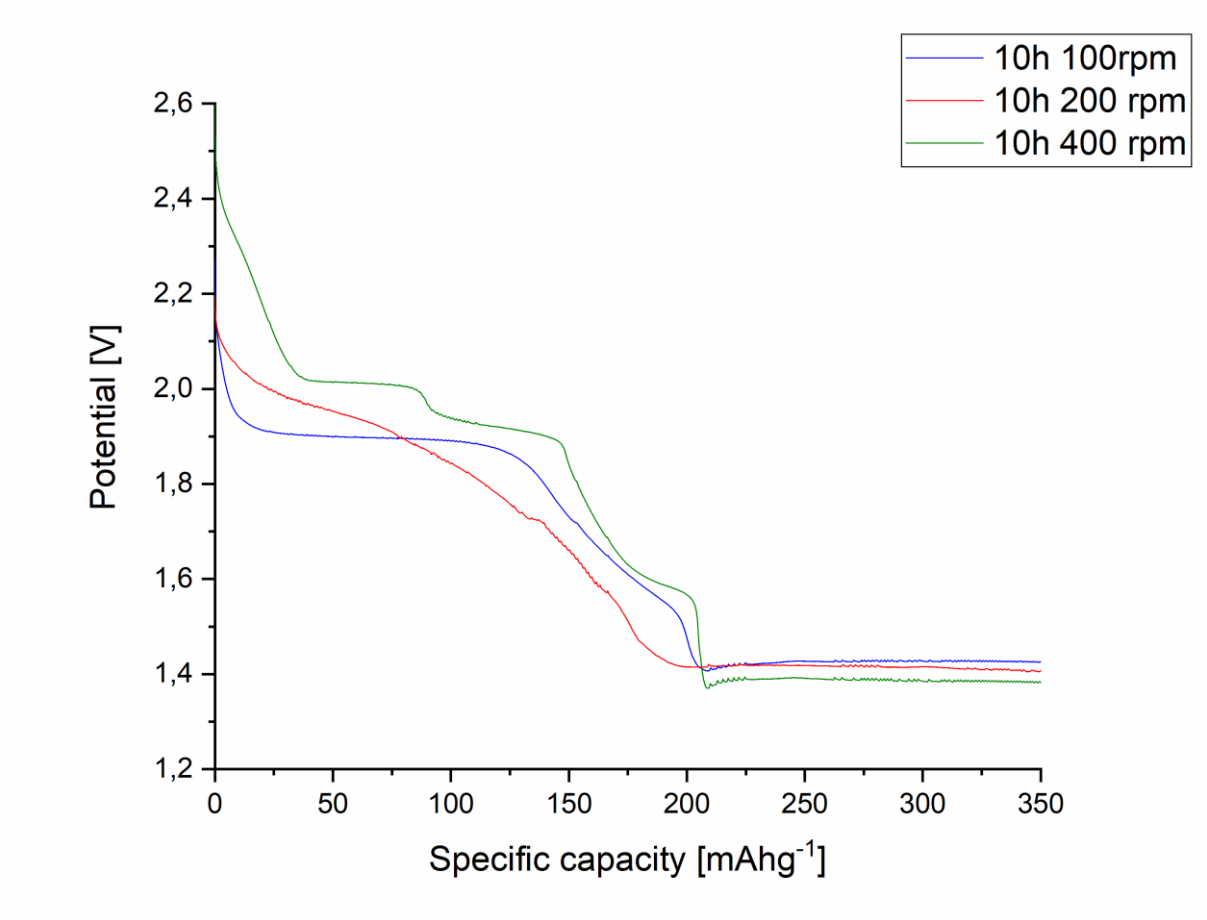

Figure 35: Equilibrium discharge curves of SnS_2 ball-milled for 10 hours at different revolution per minute.

As described in chapter 2.2, the presence of voltage plateaus may indicate the occurrence of phase transformations in the different materials as a function of lithium intercalation. To gather further information on the phase evolution in the sample that was milled for 10 hours at 400 rpm, ex-situ XRD was performed on electrodes that were discharged to specific capacities of 30, 60, 160, 210 and 375 mAh g^{-1}. Figure 36 illustrates the discharge curve of the samples and indicates the points where the discharges were stopped for ex-situ XRD exposures. The

experiments were performed with a relatively low specific current of 2.5 mA g^{-1} to ensure quasi-equilibrium conditions.

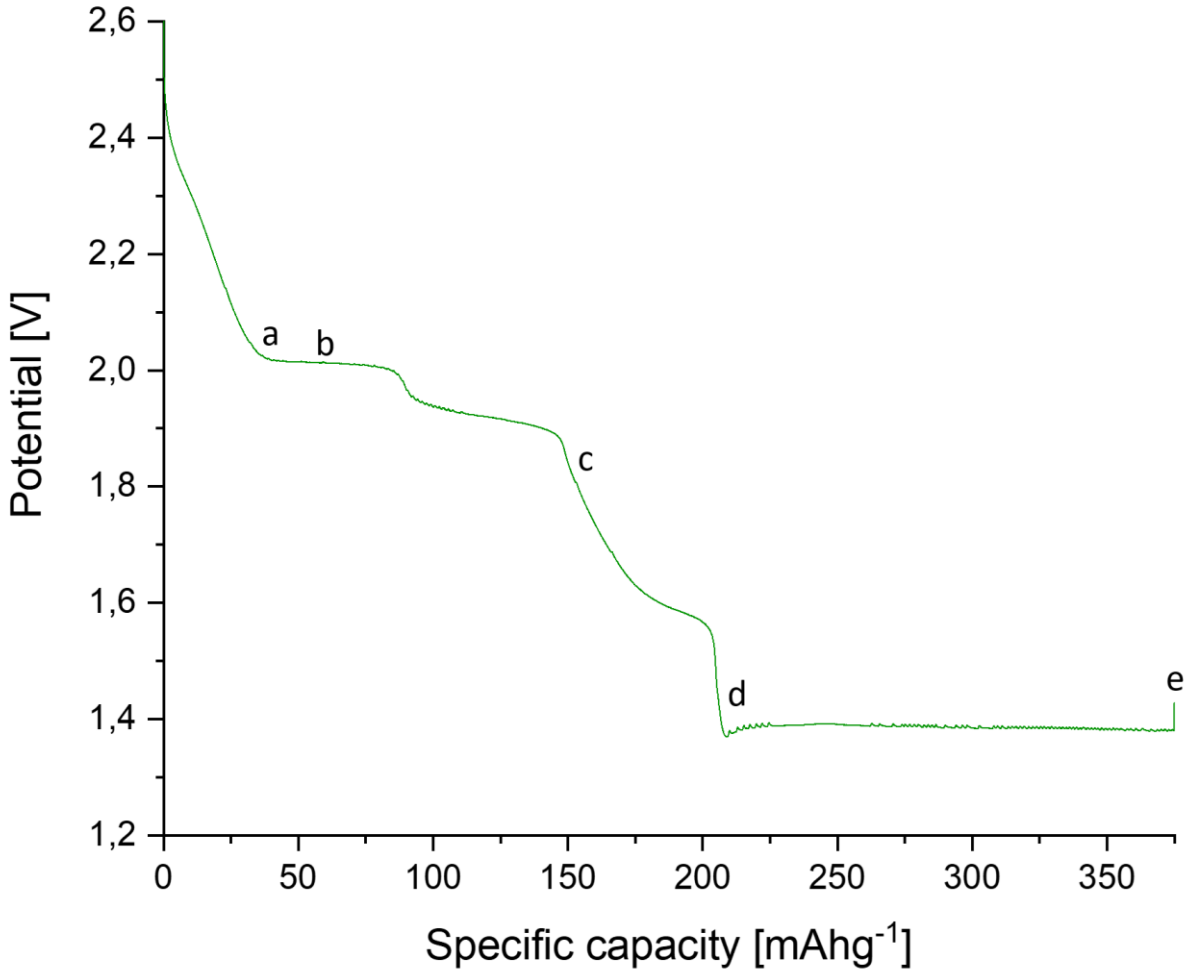

Figure 36: discharge curve for electrodes that were made from SnS_2 powders that were milled for 10 hours at 400 rpm. Discharges were stopped at a) 30, b) 60, c) 160, d) 210, respectively e) 375 $mAhg^{-1}$.

After discharge, the six (6) coin cells were disassembled and the crystalline phases determined using ex-situ XRD in argon atmosphere. Figure 37 illustrates the measured ex-situ XRD patterns of the electrodes after discharge to the specified capacities.

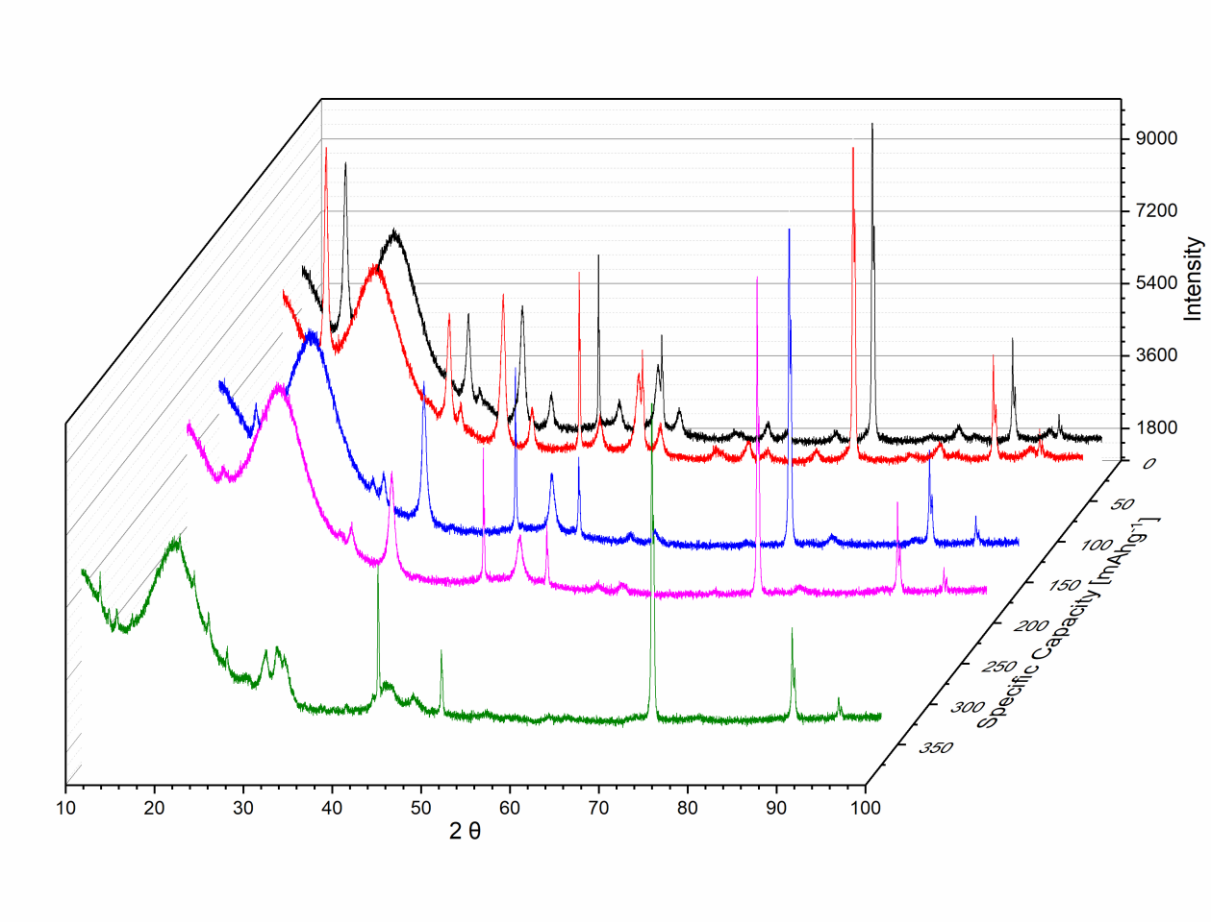

Figure 37: ex-situ XRD pattern for different discharge states of SnS_2 electrodes that were made from $_{SnS2}$ powders that was mechanochemical treated for 10 hours at 400 rpm. The electrodes were discharged with a specific current of 2.5 mAg^{-1}.

The broad peak at about 2θ = 20° is due to near range order diffraction effects of the amorphous polycarbonate dome that is used to ensure argon atmosphere during measurement. Since Cu was used as the current collector in electrode fabrication, it is found in all examined samples. However, it is not listed in the following table and the amounts of crystalline phases in the electrodes are normalized to 100 % without Cu. Table 6 lists data from the Rietveld refinements of the patterns illustrated in Figure 37.

Table 6: Rietveld refinement of BM 10h 400 rpm SnS_2 electrodes during discharge.

				Lattice parameters [Å]			
sample	**phase**	**amount [%]**	**space group**	**a**	**b**	**c**	**R_{wp}**
a	SnS_2_3c	100	R-3m	3.650(2)		17.87(2)	2.814
b	SnS_2_3c	100	R-3m	3.650(3)		17.87(2)	2.52
c	Li_2SnS_3	100	R-3m	3.846(3)		18.64(3)	2.865
d	Li_2SnS_3	100	R-3m	3.850(4)		18.62(4)	2.845
e	Li_2SnS_3	66	R-3m	3.82(1)		19.1(1)	2.787
	Sn	29	$I4_1$/amd	5.83(1)		3.181(9)	
	Li_4SnS_4	5	Pnma	14.65(3)	7.61(8)	6.42(9)	

There is no significant difference between samples a and b, since both feature the polytype phase SnS_2_3c after discharge to 30 and 60 $mAhg^{-1}$, respectively. Nevertheless, the *a* and *c* lattice parameters of the polytype are slightly larger compared to those of the non lithiated polytype structure with *a*=3.641(1) and *c*=17.837(8) Å whereby the enlargement of c is more significant. This perhaps indicates that Li atoms preferably occupy the interlayer octahedral sites. When going to the higher specific capacity values of 160 and 210 $mAhg^{-1}$ for electrodes c and d, respectively, the lithiated tin sulfide phase Li_2SnS_3 appears. This phase forms via the full intercalation of Li on the octahedral interlayer sites and the substitution of 1/3 of the Sn-atoms at the intra-layer octahedral sites by Li atoms. The sample composition shifts from the SnS_2–Li tie-line to the SnS_2–Li_2S tie-line an Sn should precipitate which is, however, not detected in XRD. Its diffraction pattern could merge into the background due to low amount, poor crystallinity or even amorphous state.

Sample e at a capacity of 375 $mAhg^{-1}$shows Sn, the lithated phases Li_2SnS_3 and Li_4SnS_4 and additional peaks which could not yet be identified. The composition Li_4SnS_4 is also on the SnS_2–Li_2S tie-line and forms on further substitution of Sn by Li. This seems to be the last step before the conversion reaction where Sn and Li_2S is formed. It was further observed that the additional peaks enhance and the peaks from Li_2SnS_3 lower if the domes are measured again after a couple of days. Since there is no indication for oxidation, we believe that the release of mechanical strain from electrochemical lithiation leads to phase transformations. Unfortunately, phase diagrams of the ternary materials system Li-S-Sn are not available.

Since the lithiation mechanism of the SnS_2_3c polytype is not completely clarified, further investigations using the galvanostatic intermittent titration technique (GITT) should be performed to ensure a better approximation to equilibrium conditions during the lithiation reaction.

6.1.4 SnS_2/C composites

After the preliminary tests, SnS_2/C composites with 10 wt. % and 20 wt. % MCMB graphite powder were ball milled at 100, 200 and 400 rpm for 10 hours, respectively, to create the active electrode material. After milling, the powder samples were characterized using SEM and PXRD. SEM micrographs of SnS_2/C composites after mechanochemical treatment are illustrated in Figure 38.

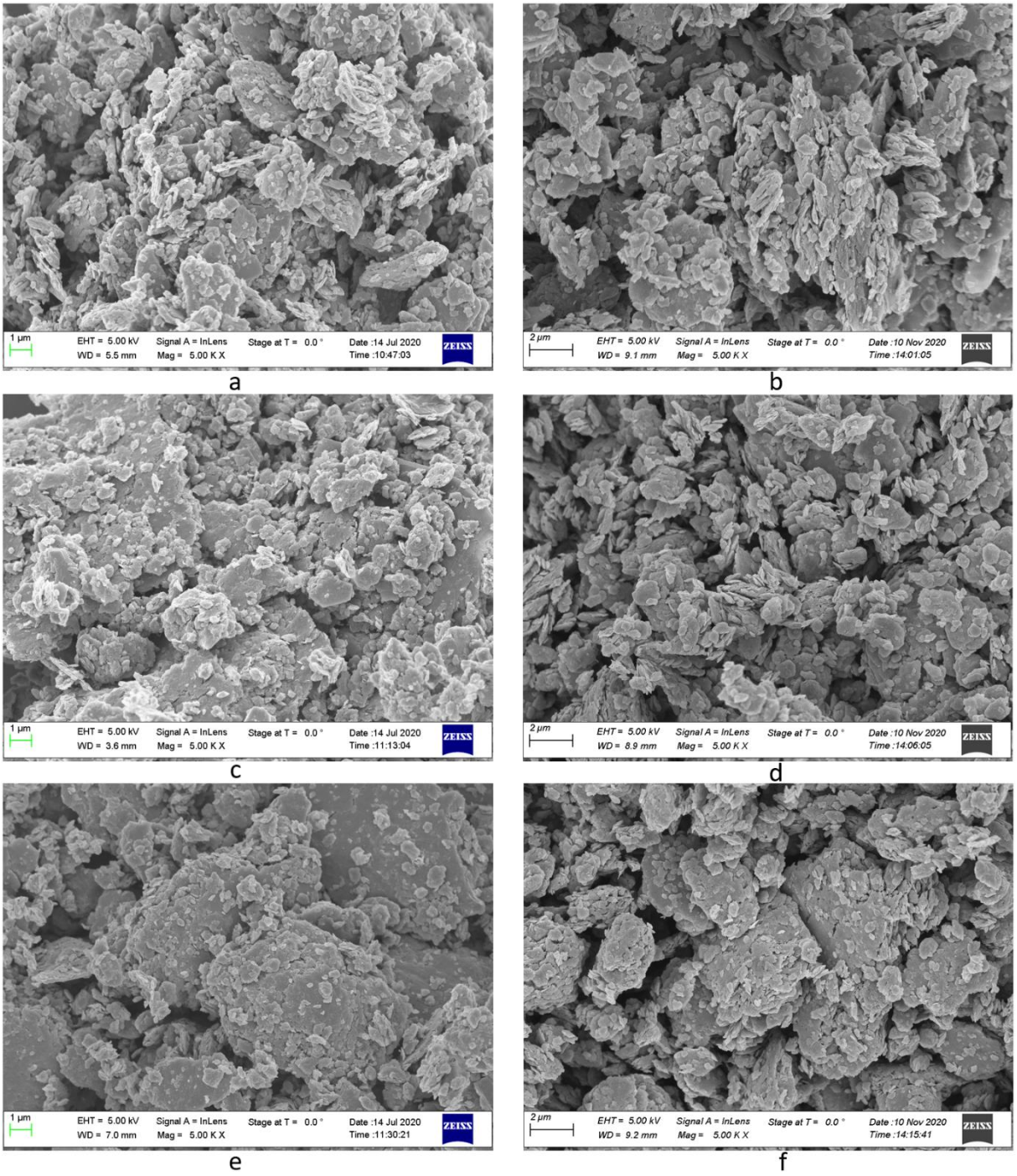

Figure 38: SEM SnS_2/C composite powders a)10 % C 100 rpm b) 20%C 100 rpm c)10%C 200 rpm d) 20%C 200 rpm e) 10% C 400 rpm f) 20%C 400 rpm.

In general, the morphology of the ball milled SnS_2 samples with 10 wt.% and 20 wt. % graphite are quite similar to each other (see Figure 38). The SEM micrographs further show that nano-particles are not formed when milling is performed with additional carbon as opposed to without

carbon (see Figure 28 for comparison). In fact, the MCMB graphite may be acting as a lubricant to reduce the forces on the SnS_2 particles during milling. The measured XRD patterns of the SnS_2/C composite samples with 10 and 20 wt.% carbon, which were ball-milled for 10 hours at 100, 200 and 400 rpm are shown in Figure 39 and Figure 40, respectively.

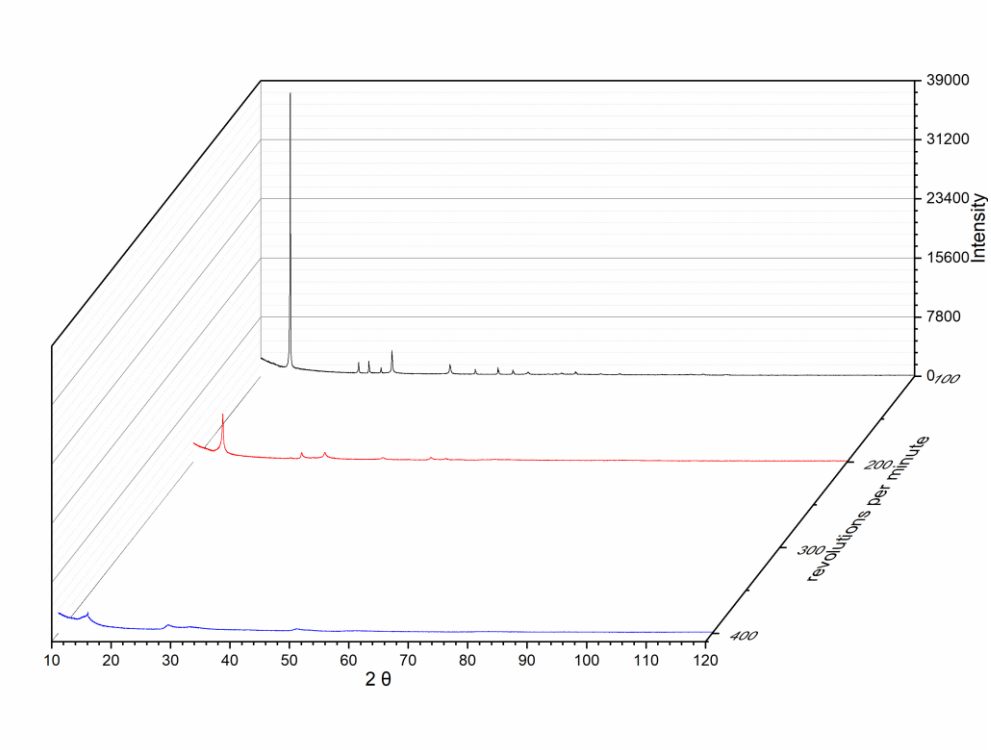

Figure 39: PXRD patterns of SnS_2/C composite powders with 10 wt.% carbon after mechanochemical treatment for 10 hours at 100, 200 and 400 rpm.

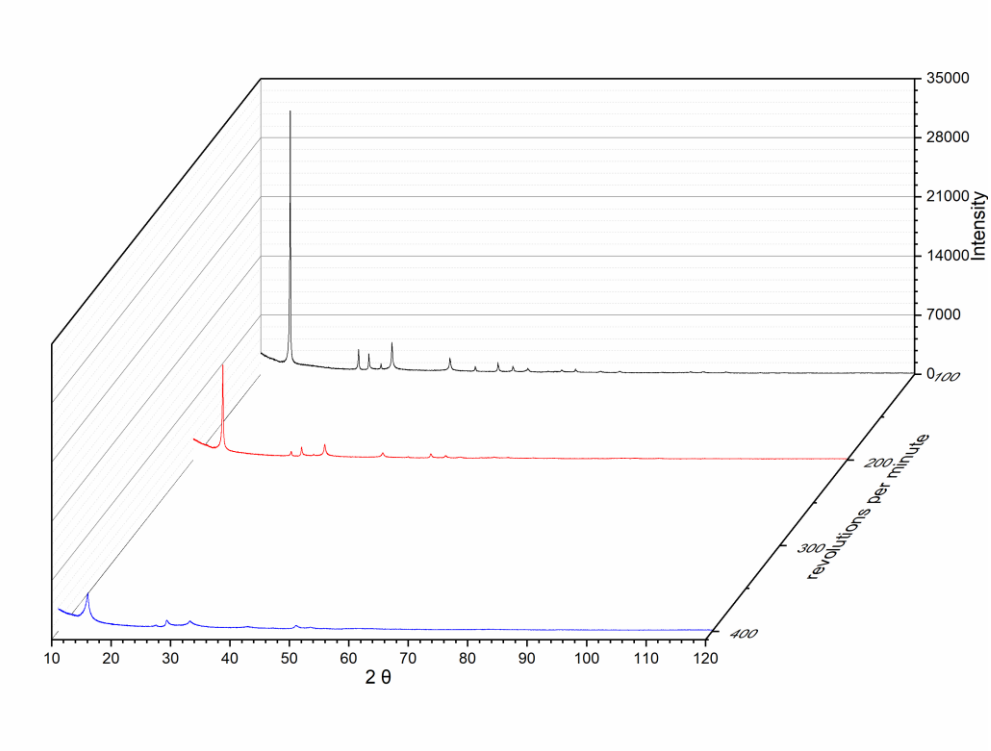

Figure 40: PXRD patterns XRD SnS_2/C composite powders with 20 wt.% carbon after mechanochemical treatment for 10 hours at 100, 200 and 400 rpm.

Rietveld refinement of the measured XRD patterns of the samples was also performed and the results are given in Table 7.

Table 7: Rietveld refinement of SnS_2/C composite powders.

				Lattice parameters [Å]		
sample	**phase**	**amount [%]**	**space group**	**a**	**c**	**R_{wp}**
SnS_2/10C 10h100rpm	SnS_2 (Berndtite 3R)	88	P-3m1	3.648(1)	5.898(2)	11.706
	graphite 2H	12	P63/mmc	2.48(1)	6.72(1)	
SnS_2/10C 10h200rpm	SnS_2 (Berndtite 3R)	98	P-3m1	3.642(7)	5.93(2)	8.645
	graphite 2H	2	P63/mmc	2.55(6)	6.7(1)	
SnS_2/10C 10h400rpm	SnS_2 (Berndtite 3R)	73	P-3m1	3.605(9)	5.97(7)	6.637
	SnS_2_3c	27	R-3m	3.60(5)	18.2(1)	
	graphite 2H	amorphous				
SnS_2/20C 10h100rpm	SnS_2 (Berndtite 3R)	82	P-3m1	3.645(4)	5.907(9)	13.497
	graphite 2H	18	P63/mmc	2.50(1)	6.72(1)	
SnS_2/20C 10h200rpm	SnS_2 (Berndtite 3R)	86	P-3m1	3.643(5)	5.90(1)	11.36
	graphite 2H	14	P63/mmc	2.51(1)	6.72(4)	
SnS_2/20C 10h400rpm	SnS_2 (Berndtite 3R)	80	P-3m1	3.639(8)	5.92(3)	7.478
	SnS_2_3c	16	R-3m	3.65(3)	17.93(8)	
	graphite 2H	4	P63/mmc	2.50(2)	6.76(3)	

Table 7 clearly shows that also the amount of detectable, crystalline carbon decreases with increasing number of revolutions per minute. In the samples milled at 100 and 200 rpm, only the 2H-SnS_2 modification was observed for SnS_2. However, at 400 rpm, the SnS_2_3c polytype phase was additionally identified. At this milling speed, no crystalline carbon phases were detected for the sample milled with 10 wt. % MCMB graphite, whereas for the sample milled with 20 wt. % MCMB graphite, a small amount of a carbon phase could be detected. Interestingly, the *c* lattice parameter of the polytype structure SnS2_3c is noticeably larger after mechanochemical treatment for 10 hours at 400 rpm compared to the samples without carbon.

6.1.5 Electrochemical performance of SnS_2 and SnS_2/C composite material

Nine (9) SnS_2 samples with 0, 10 and 20 wt. % carbon, which were milled at 100, 200 and 400 rpm, were investigated electrochemically via galvanostatic cycling with potential limitation (GCPL). Cycling was performed in the potential window between 0.01 and 1.8 V vs Li^+/Li at a specific current of 100 $mAhg^{-1}$.

The cycling performance of the pristine SnS_2 and ball-milled SnS_2 electrodes with and without carbon is shown in Figure 41 and Figure 42. In all cases, one can observe an irreversible capacity loss during the first cycle, which occurs due to the irreversible conversion reaction of SnS_2 with Li that can be written as:

$$SnS_2 + 4Li^+ + 4e^- \rightarrow 2Li_2S + Sn$$

This non-reversible conversion reaction leads to the formation of Sn particles surrounded by a Li_2S matrix. The reversible capacity of the electrode after the first cycle originates from the cycling reaction of $Li^+ + e^-$ and Sn.

The results of the electrochemical tests show capacity degradation after approximately the 25th cycle for the pristine sample as well as those which were milled for 10 hours at 100 and 400 rpm without carbon (see Figure 41a). Filled out symbols indicate discharge capacities while empty symbols show the charge capacity. A much better cycling performance is observed for samples that were ball-milled for 10 hours with 200 rpm without carbon. It can be assumed that this improved performance is due to reduction in particle size. A significantly improved performance of electrodes fabricated from SnS_2 powders that were ball-milled with carbon at 400 rpm for 10h is noticeable in Figure 41b and c. These electrodes do not show the typical capacity degradation after the 25th cycle compared to other electrodes.

Figure 42a, b, and c show the cycling performance of SnS_2/C composite materials as a function of carbon content at the investigated rotation speeds of 100, 200 and 400 rpm, respectively. Figure 42a and b reveal that there is no significant improvement in cycling performance with increasing carbon content for samples that were milled at 100 rpm and 200 rpm. However, Figure 42c shows a large difference in performance at 400 rpm depending on the carbon content. While the sample without carbon shows capacity degradation at the 25th cycle, those with 10 and 20 % graphite perform very well throughout 50 cycles.

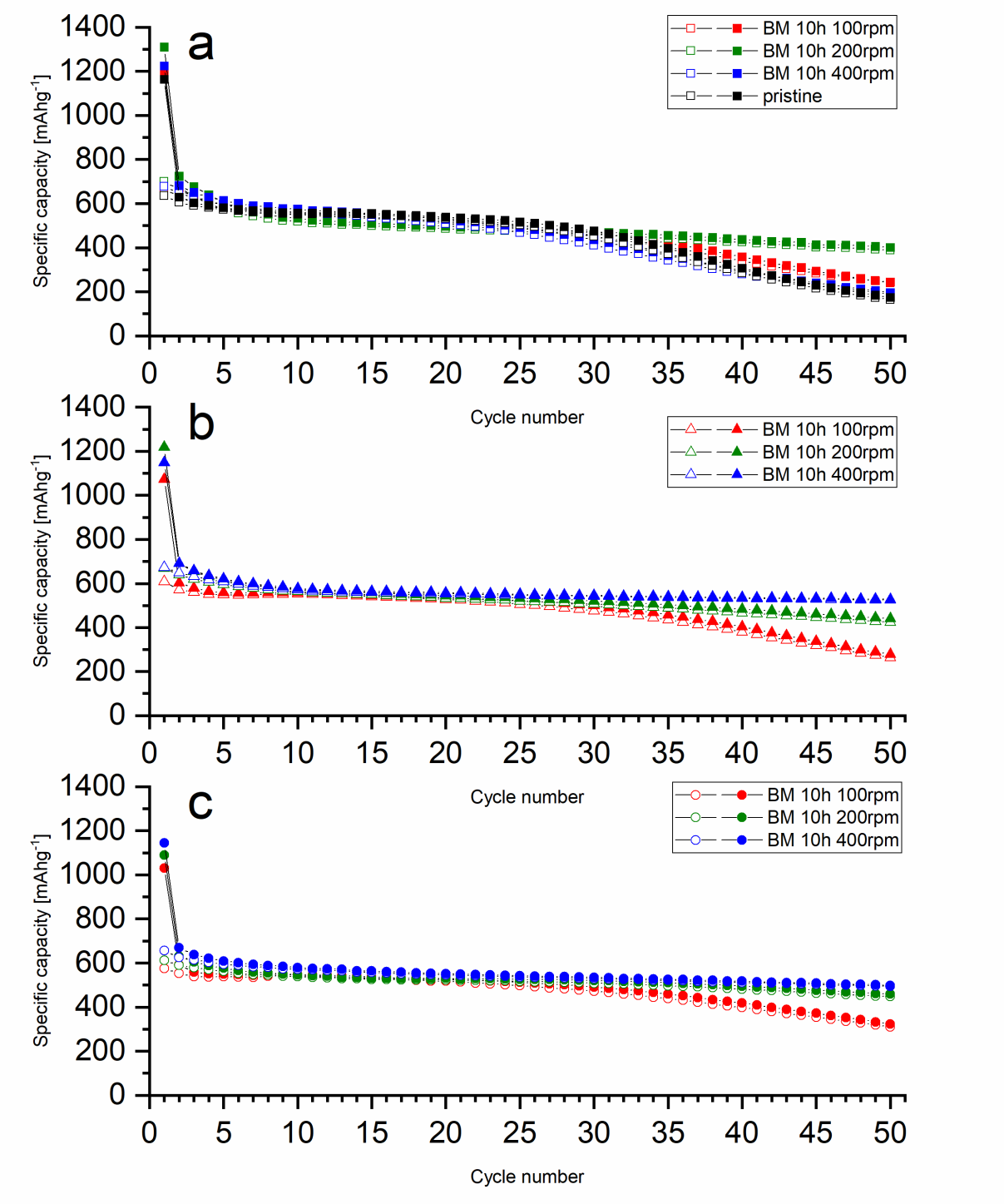

Figure 41: Cycling performance of SnS_2/C composite electrodes with a) 0% graphite, b) 10% graphite and c) 20% graphite in the active material. Discharge capacities shown as filled out symbols and charge capacities shown as empty symbols.

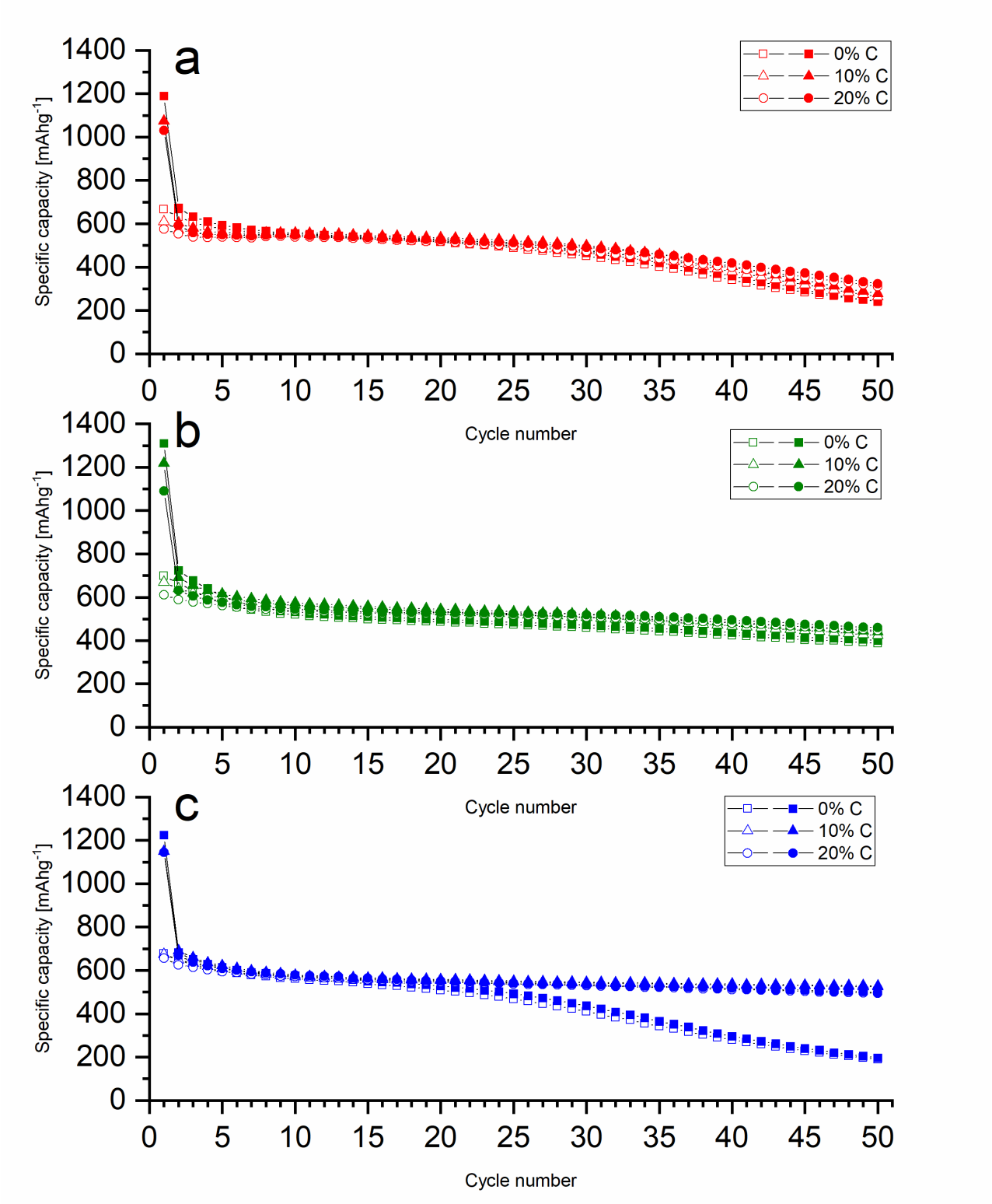

Figure 42: Cycling performance of SnS_2/C composite electrodes with active material that was milled at a)100rpm, b) 200rpm respectively c) 400rpm for 10 hours. Discharge capacities shown as filled out symbols and charge capacities shown as empty symbols.

To understand these different trends, post-mortem SEM and PXRD were performed on the electrodes after cycling. The SEM micrographs of the cycled electrodes, which were fabricated with pristine and ball milled SnS_2 with 0 wt. % carbon, are shown in Figure 43.

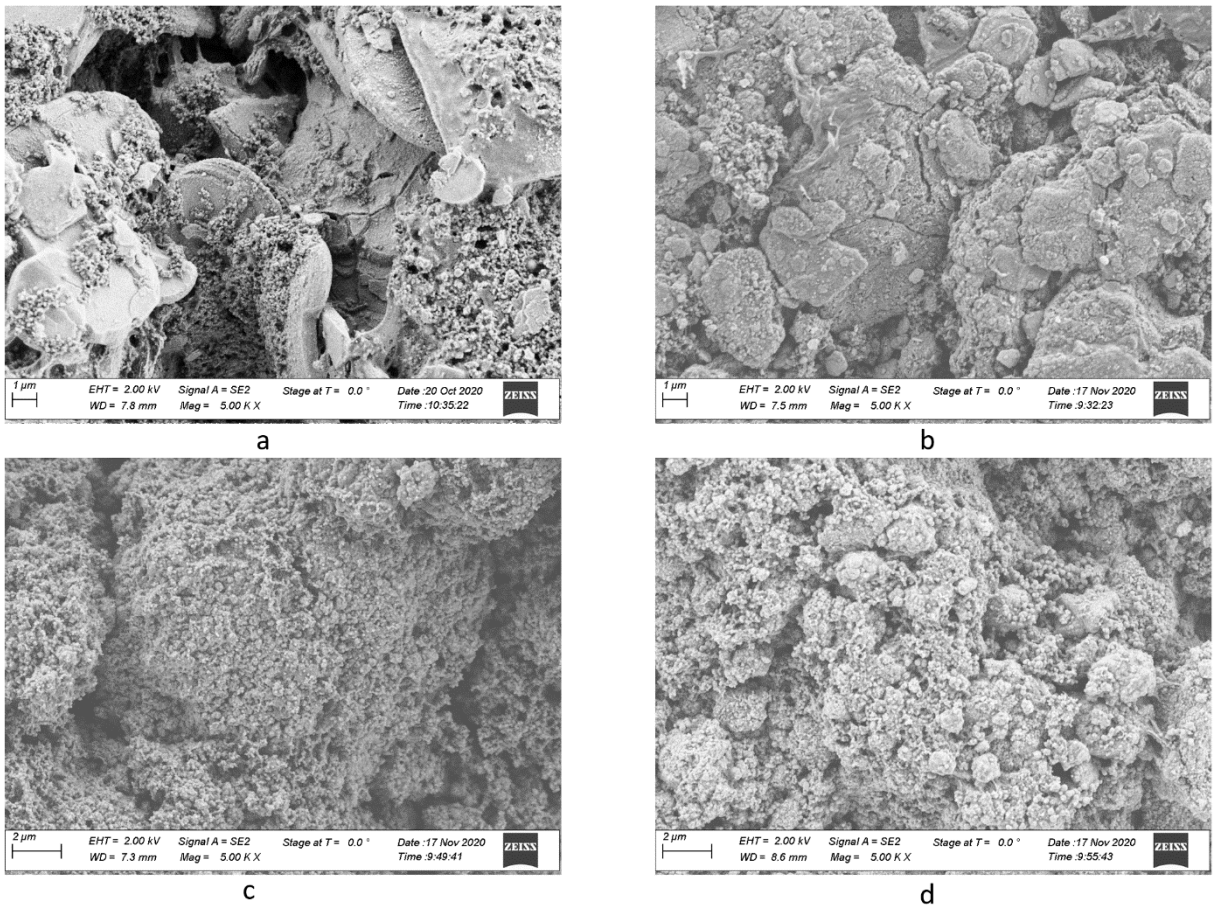

Figure 43: post-mortem SEM of electrodes after 50 cycles with a) pristine or ball-milled for b) 10 hours at 100rpm c) 10 hours at 200rpm d) 10 hours at 400 rpm SnS_2 anode active material.

Post-mortem SEM of the SnS_2 electrode after cycling reveals large cracks in the platelets, which are only connected to each other via the binder material PVDF and the C45 conductive additive. A similar microstructure is obtained for the cycled electrode of the sample which was milled for 10h at 100 rpm.

Unexpectedly, the samples which were milled for 10 hours at 200 rpm performed better than those which were milled for 10h at 400 rpm. One possible explanation for this effect can be found in the post-mortem SEM micrographs of the electrodes in Figure 43. Although, both consist of nano-sized primary particles, there appears to be a strong formation of agglomerates in the 10h 400 pm electrodes, which become physically isolated from each other during cycling. At 200 rpm, however, the primary particles do not agglomerate, remain well distributed and are therefore in better contact with the C45 conductive carbon.

The post-mortem SEM micrographs of electrodes with 10 and 20 wt. % carbon after 50 cycles are shown in Figure 44. Large cracks are evident in the electrode active material for the samples which were milled at 100 and 200 rpm. However, evenly distributed particles of the active material with nearly no cracks could be observed in the SEM micrograph of the samples which were milled at 400 rpm with carbon. One possible hypothesis for the reduced crack formation is that, since graphite can act as a buffer phase between the active material particles during lithiation, there is less mechanical stress on the particles during the alloying reaction, and therefore less crack formation during cycling.

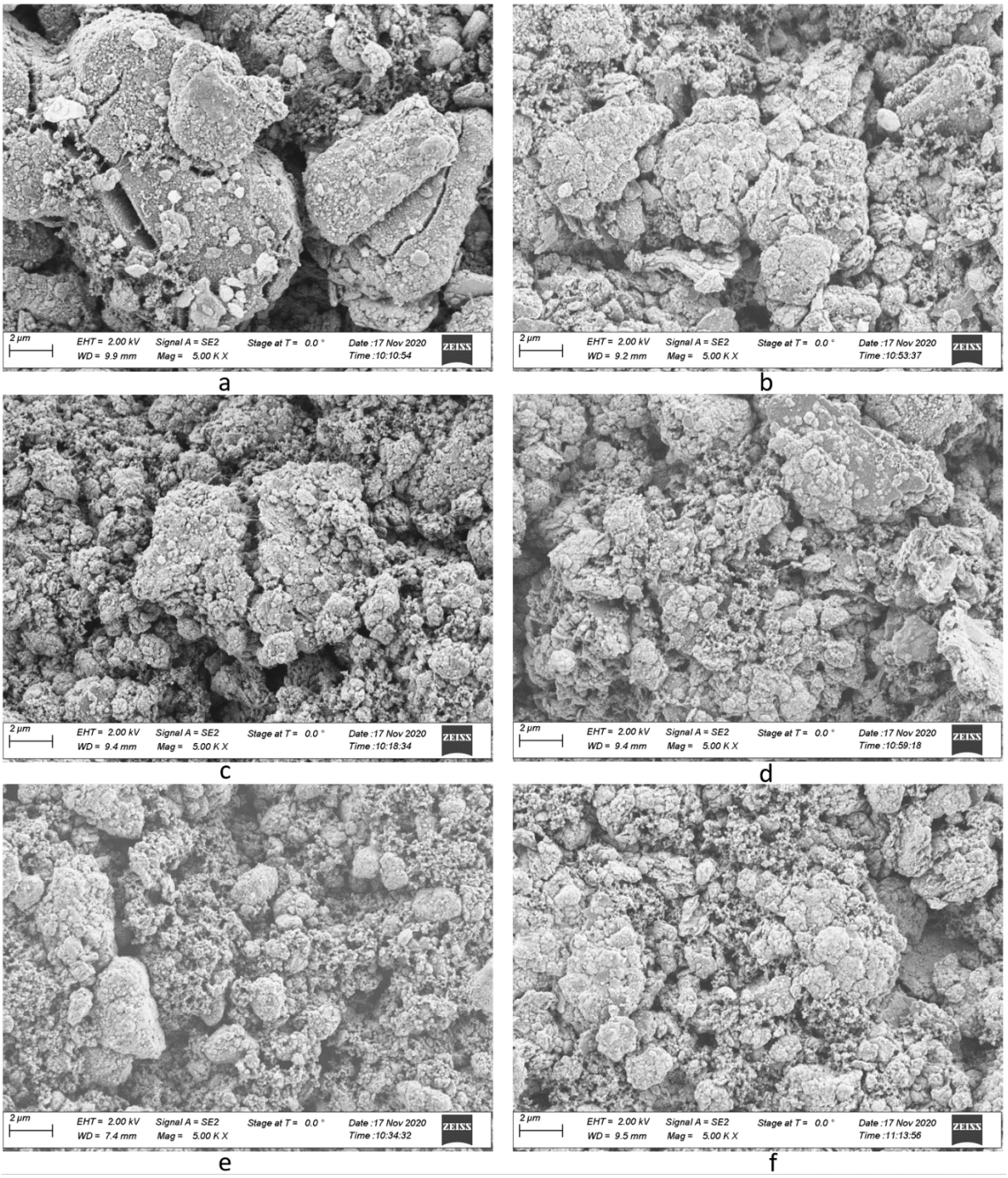

Figure 44: SEM SnS_2/C composite post mortem electrodes after 50 cycles a) 10% C 100 rpm b) 20%C 100 rpm c)10%C 200 rpm d) 20%C 200 rpm e) 10% C 400 rpm f) 20%C 400 rpm.

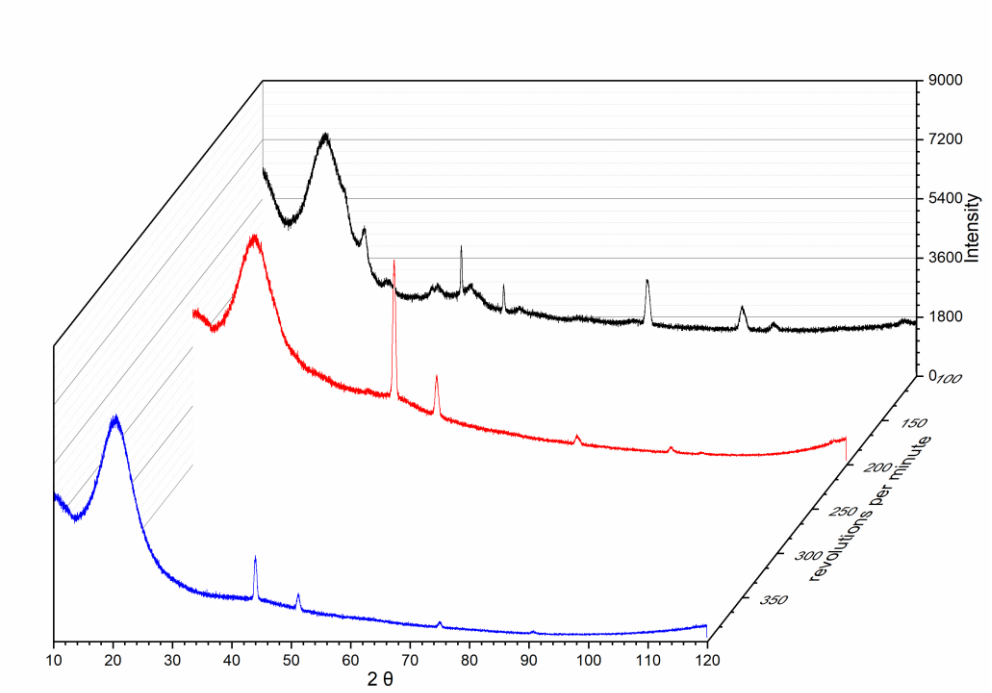

Figure 45: post-mortem XRD pattern of electrodes that were fabricated from SnS_2 powders that were ball milled for 10 hours.

Post-mortem XRD was performed on the cycled electrodes of the SnS_2 samples after mechanochemical treatment for 10 hours at 100, 200 and 400 rpm (Figure 45). The measured powder patterns show no crystalline phases in the electrode active material at 200 rpm and 400 rpm after cycling, since the only detectable peaks are those from the Cu current collector. However, for the cycled electrode from the sample milled at 100 rpm (Figure 46), Sn, Li_2S and Li_2Sn_5 could be found as poorly crystalline phases. The broad peak at about 2θ = 20° comes from near range order diffraction effects of the amorphous polycarbonate dome.

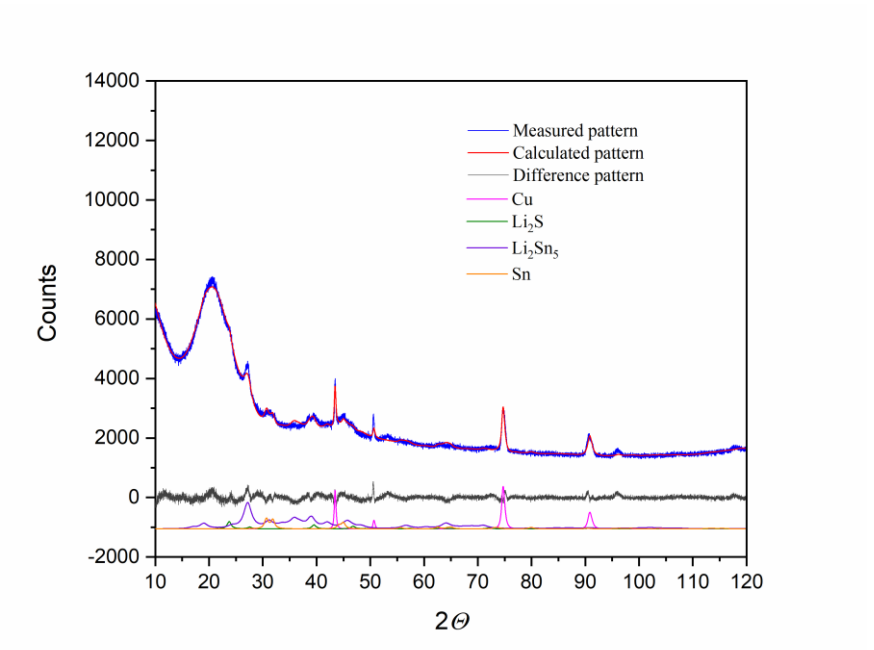

Figure 46: XRD pattern of the cycled electrode after 50 cycles BM 10h 100rpm.

Data on the post-mortem XRD investigations of the electrodes that were prepared using only ball milled SnS_2 as the active electrode material are listed in Table 8.

Table 8: Rietveld refinement of post mortem SnS_2 electrodes after 50 cycles.

				Lattice parameter [Å]		
Sample	**phase**	**amount [%]**	**space group**	**a**	**c**	**R_{wp}**
SnS_2_pm10h100rpm	Li_2Sn_5	66	P4/mbm	10.2467774	3.240775	
	Li_2S	23	Fm-3m	6.3994054		
	Sn	11	$I4_1$/amd	5.7691169	3.1742553	3.209
SnS_2_pm10h200rpm	amorphous					
SnS_2_pm10h400rpm	amorphous					

Post mortem XRD was also performed on the cycled electrodes which contain additions of 10 and 20 wt.% of graphite in the active material. Table 9 lists the results of the Rietveld refinement of the measured XRD patterns.

Table 9: Rietveld refinement of post mortem SnS_2/C electrodes after 50 cycles.

				Lattice parameter [Å]		
Sample	**phase**	**amount [%]**	**space group**	**a**	**c**	**R_{wp}**
SnS_2_10C_pm100	Li_2S	77	Fm-3m	6.48(8)		
	Li_2Sn_5	13	P4/mbm	10.13(8)	3.34(4)	
	Sn	10	$I4_1$/amd	5.86(5)	3.16(4)	3.388
SnS_2_10C_pm200	*					
SnS_2_10C_pm400	Li_2S	69	Fm-3m	6.470(7)		
	Sn	26	$I4_1$/amd	5.80(5)	3.22(5)	
	Li_2Sn_5	5	P4/mbm	10.4(1)	3.31(5)	2.677
SnS_2_20C_pm100	*					
SnS_2_20C_pm200	*					
	Li_2S	48	Fm-3m	6.45(1)		
	Li_2Sn_5	28	P4/mbm	10.3(1)	3.31(6)	
SnS_2_20C_pm400	Sn	24	$I4_1$/amd	5.83(6)	3.20(6)	3.458

The electrodes marked with (*) were deformed during the PXRD measurements (likely due to the internal stress in the electrodes in their charged states) so that the measured patterns could not be refined. These experiments should be repeated at a later date using more petroleum jelly to fix the electrodes onto the silicon monocrystal sample holder.

Since the electrodes are in in charged state for the post-mortem investigations, only Li_2S and Sn are the expected crystalline phases. However, all measured electrodes feature the phase Li_2Sn_5. The cycling mechanism for the alloying reaction can be written in simplified form as:

$$Sn \rightleftharpoons Sn + Li_2Sn_5 \rightleftharpoons Li_2Sn_5 \rightleftharpoons Li_2Sn_5 + Li_{17}Sn_4 \rightleftharpoons Li_{17}Sn_4$$

Therefore, the appearance of Li_2Sn_5 in the electrodes in the charged states indicates that the de-alloying reaction is not completely reversed.

To sum up the mechanochemical route, these investigations were a great success in total. It was possible to improve the performance of pristine SnS_2 significantly via ball milling for 10 hours at 200 rpm, this is due to reduction of particle sizes. In addition, the synthesis of SnS_2/C composite materials made it possible to achieve excellent electrochemical performances with almost no capacity degradation after the first cycle, especially for samples with carbon content of 10 wt. % that were milled for 10 hours at 400 rpm.

6.1.6 Carbon content determination of SnS_2/C composites with TGA

CHNSO elemental analysis is the analytical technique of choice for determining the carbon contents of materials. In this method, the sample is weighed and then introduced into the elemental analyzer, where it is combusted. The gaseous products of the combustion reaction are directed into a gas chromatograph, where the ratio of the combustion products (e.g. CO_2, NO_2, H_2O and SO_2) as determined. Using this ratio, the compositions of the elements C, H, N, and S in the sample can be determined.

Although CHNSO elemental analysis is the usual method for carbon content determination, TGA was explored in this thesis as an alternative method to determine the carbon contents of our samples and to check the homogeneity of the carbon distribution. To do this, SnS_2 samples with defined amounts of carbon (10 wt. % and 20 wt. % MCMB graphite) were prepared by ball-milling and investigated using TGA at the University of Vienna. Additionally mixtures of SnS_2 and 10 wt. % graphite, which were prepared using a mortar, were also investigated. The TGA experiments were performed in synthetic air (80 % N_2, 20 % O_2) flow, with a heating rate of 10 °C/min up to 1200 °C. Before the TGA experiments, the mass of the sample was weighed using an external microbalance. After the TGA experiments, the mass of the sample residue was weighed and PXRD was performed to characterize the phase constitution of the sample after TGA. Figure 47 illustrates the TG curve of a SnS_2 sample with 10 wt. % carbon.

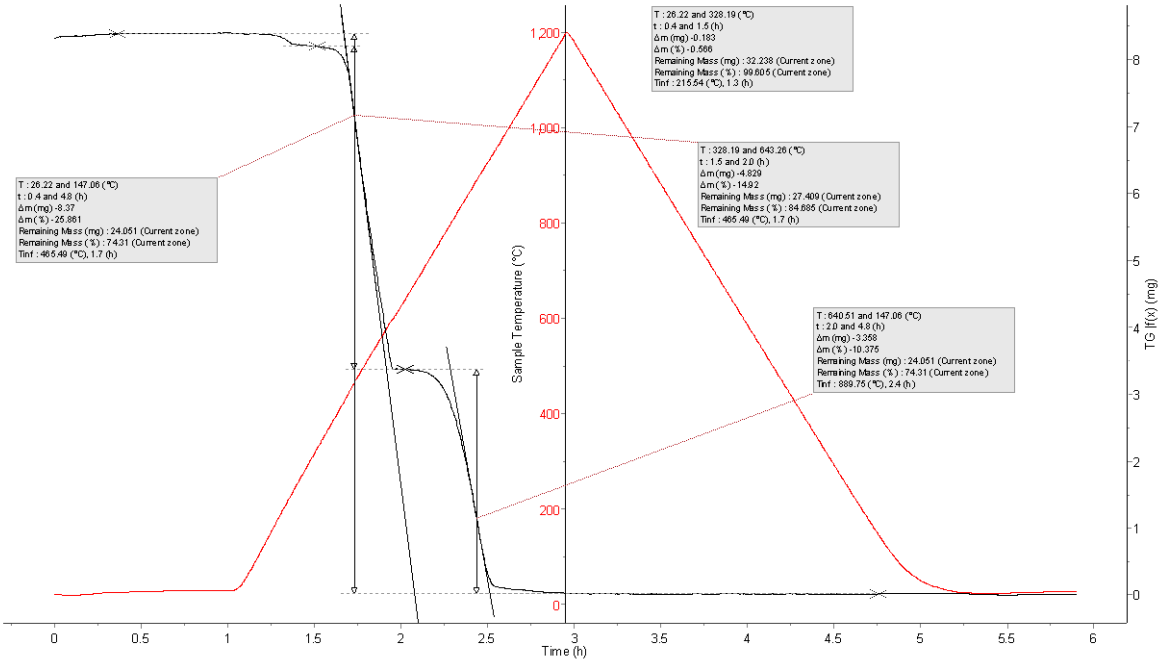

Figure 47: TG of SnS_2 with 10 wt. % graphite.

At least three steps can be distinguished in the TGA curve, where the first one can be attributed to the loss of a small amount of water[2]. This effect was also observed by other authors, e.g. Prabha et al. [53]. The other two steps are most likely due to the evolution of gas-species such as SO_2 and CO_2 during the reaction with O_2. However, the exact nature of the reaction occurring at each step in the TG curve cannot be determined without a chemical composition

[2] This step has an inflection point at 216 °C what seems to be too high for surface water. Water of constitution was not described for SnS_2 and thus we suppose it comes from a minor intercalation of water molecules into the layered structure.

analysis of the exhaust gas. Rietveld refinement of the PXRD pattern of the sample residues after TG showed only phase pure SnO_2 for all powders investigated. XRD data is listed in Table 10 and one XRD pattern of SnO_2 is illustrated in Figure 48.

Table 10: Rietveld refinement of 10h 200 rpm ball milled SnS_2/C with 10 wt. % respectively 20 wt. % graphite after TG in synthetic air.

			Lattice parameters [Å]		
sample	**phase**	**space group**	**a**	**c**	**R_{wp}**
TG_SnS_2/10C_1	SnO_2	P42/mnm	4.7397(9)	3.1869(7)	7.411
TG_SnS_2/10C_2	SnO_2	P42/mnm	4.7373(3)	3.1863(5)	9.257
TG_SnS_2/10C_3	SnO_2	P42/mnm	4.7378(5)	3.1867(7)	10.549
TG_SnS_2/20C_1	SnO_2	P42/mnm	4.7379(4)	3.1867(5)	11.424
TG_SnS_2/20C_2	SnO_2	P42/mnm	4.7380(4)	3.1868(5)	11.351
TG_SnS_2/20C_3	SnO_2	P42/mnm	4.7350(7)	3.1870(8)	9.123

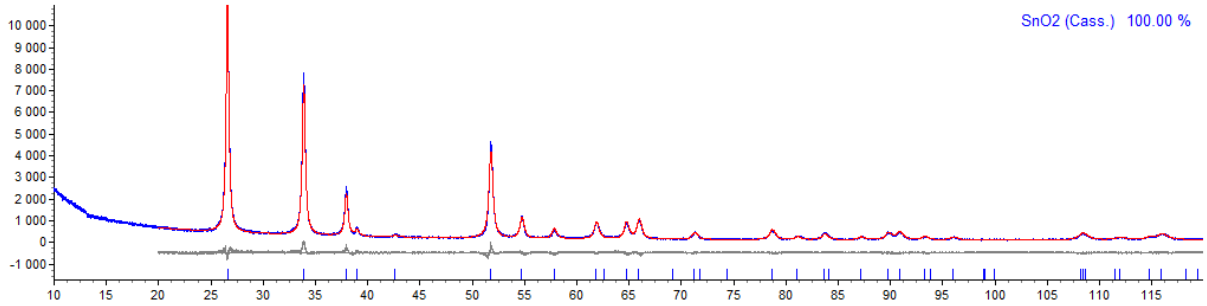

Figure 48: XRD of ball milled 10 hours 200 rpm SnS2/C composite sample after TG showing phase pure SnO_2.

Since all powders have been identified as phase pure SnO_2, a chemical reaction for the decomposition of SnS_2 (without MCMB graphite) can be written as follows:

$$SnS_2 + 3\,O_2 \rightarrow SnO_2 + 2SO_2$$

According to this reaction, the theoretical mass loss associated with the reaction of SnS_2 with O_2 is 17.6% and the residual mass should be 82.4%. Mass losses of 17.4 and 17.8 % are in excellent agreement with the theory.

A similar equation can also be written for the reaction of mixtures of SnS_2 and MCMB graphite as:

$$xSnS_2 + (1-x)C + (2x+1)\,O_2 \rightarrow xSnO_2 + 2xSO_2 + (1-x)CO_2$$

where *x* is the mole fraction of SnS_2 in the SnS_2+C mixture, and the formation of CO_2 is assumed. Therefore, based on the masses of the samples before and after the TGA experiments, the amount of graphite in the samples can be determined. Table 11 lists the carbon content of the SnS_2/10 wt.% graphite mixtures that were prepared using the mortar. The TG carbon content was determined using baseline correction from two successive thermo cycles while the TG raw carbon content was determined without baseline correction. It has to be mentioned that the mass loss in the last step is 10.4 %, this is very close to the carbon content. Obviously, the graphite burns selectively with the highest rate at 890 °C after the decomposition of SnS_2 with the highest rate at 465 °C.

Table 11: carbon content of mixtures of SnS_2 and graphite determined with TG and external weighing.

	microbalance	**TG**	**TG raw**
1	9.96	10.16	10.06
2	9.94	10.00	9.89
3	9.92	10.11	9.97
average	**9.94**	**10.09**	**9.97**
σ	0.02	0.07	0.07

The carbon content determined with TG and via external weighing is fairly close to the expected one and the method is therefore a suitable alternative for CHNSO elemental analysis.

The carbon contents determined via TG, TG raw and external weighing of the SnS_2/C composite materials, which were prepared by ball-milling, are listed in Table 12. Three samples were taken respectively.

Table 12: carbon content of ball milled samples after mechanochemical treatment for 10 hours at 200rpm determined with TG, TG raw and external weighing.

	microbalance	**TG**	**TG raw**		**microbalance**	**TG**	**TG raw**
1	12.27	12.12	11.56		21.55	21.23	21.11
2	12.09	11.80	11.63		21.66	21.73	21.58
3	12.06	11.68	11.63		21.44	21.32	21.22
average	**12.14**	**11.86**	**11.60**		**21.55**	**21.43**	**21.30**
σ	0.09	0.18	0.03		0.09	0.22	0.20
Expected carbon content	10				20		

In general, a significantly higher carbon content than expected was measured in all ball-milled samples. The standard deviation is slightly higher than without ball milling but well below this difference. Our conclusion is that ball milling results in homogeneous distribution of graphite in SnS_2 and the higher C contents in the ball-milled samples is most probably due to the preferred adhesion of SnS_2 onto the milling bowl and spheres.

6.2 Thermal route

6.2.1 Evaluation of coating temperature

To determine the ideal temperature for the coating of SnS_2 via thermal decomposition of PVA, thermogravimetry in combination with differential thermal analysis was performed in argon flow on pristine PVA, powder samples of SnS_2 that were subjected to ball-milling at 200 rpm for 10 hours, and on a 1:1 mass mixture of SnS_2 and PVA that was homogenized with an agate mortar. Figure 49 shows the measured TG-DTA curves of PVA as it is heated to a temperature of 1050 °C with a heating rate of 10 °C/min in an argon flow of 100 ml/min. The TG signal is illustrated in green, the DTG signal in brown, and the DTA signal in blue. Two measurements were performed, the first one is illustrated with solid lines and the second one with dashed lines.

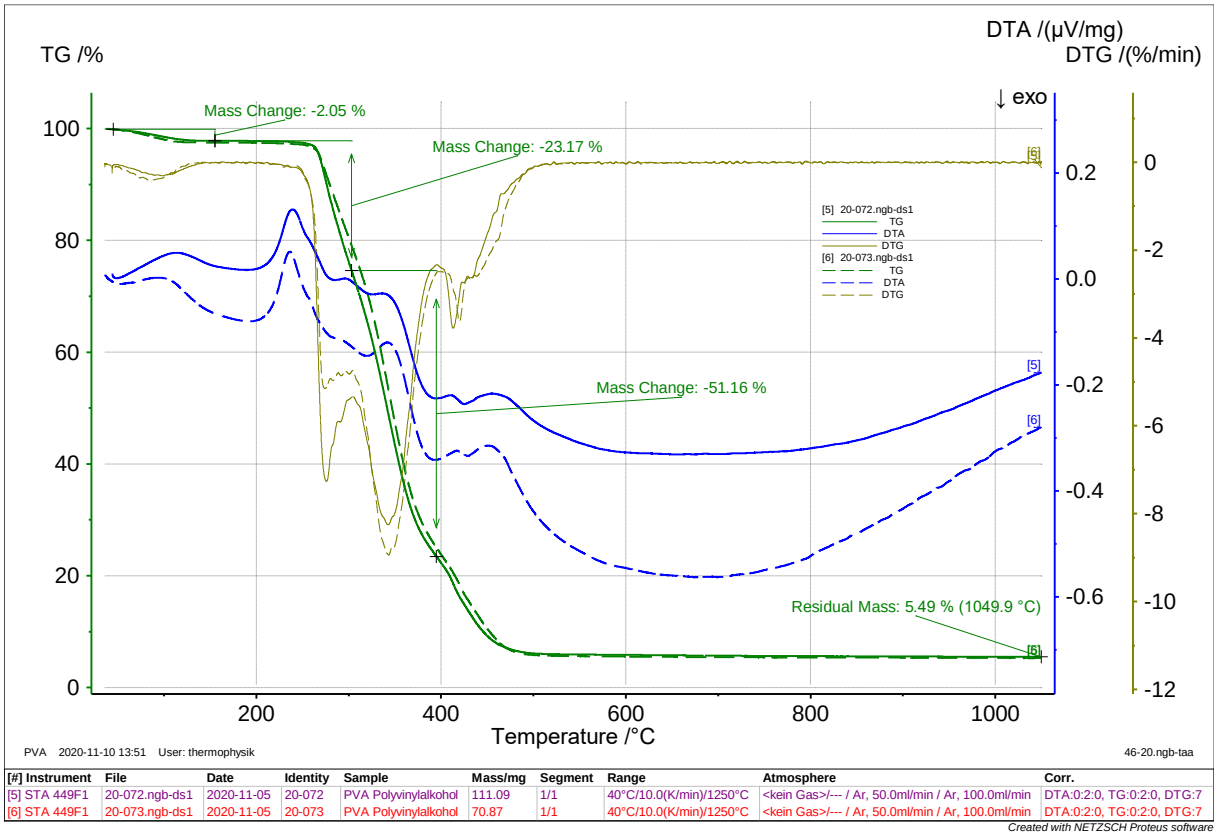

[#] Instrument	File	Date	Identity	Sample	Mass/mg	Segment	Range	Atmosphere	Corr.
[5] STA 449F1	20-072.ngb-ds1	2020-11-05	20-072	PVA Polyvinylalkohol	111.09	1/1	40°C/10.0(K/min)/1250°C	<kein Gas>/--- / Ar, 50.0ml/min / Ar, 100.0ml/min	DTA:0:2:0, TG:0:2:0, DTG:7
[6] STA 449F1	20-073.ngb-ds1	2020-11-05	20-073	PVA Polyvinylalkohol	70.87	1/1	40°C/10.0(K/min)/1250°C	<kein Gas>/--- / Ar, 50.0ml/min / Ar, 100.0ml/min	DTA:0:2:0, TG:0:2:0, DTG:7

Created with NETZSCH Proteus software

Figure 49: TG-DTA of PVA in argon flow (100ml/min) atmosphere with a heating rate of 10°C/min up to 1050 °C. Solid lines show the first measurement and dashed lines the second one.

When examining the DTG signal of the first measurement in detail, a small peak appears with a minimum at about 150°C, which is followed by three defined peaks with minima at about 270 °C, 350°C and 420 °C, respectively. In the first step, a 2.1% mass loss occurs, whereas in the 2nd, 3rd and final steps, mass losses of 23.2 %, 51.2 %, and 23.6 % were measured. The total mass loss of PVA at 1050°C in argon flow atmosphere is 94.5 %. Unfortunately, the product could not be characterized due to the low residual mass of 5.5%.

The measured TG-DTA data shown in Figure 49 are similar to those of Peng et al. [40], Raju et al. [54] and Senkevich et al. [55]. According to their measurements, which were performed in nitrogen flow atmosphere with heating rates of 5, 10, 20, 30, 40 and 50 °C/min, the thermal degradation of PVA takes place between temperatures of 300 and 500 °C. The residual mass of PVA after the heat treatment is not given numerically, nevertheless the mass loss according to the TG curve is about 95%. In the literature, the mechanism is described as two-step-

degradation at temperatures of 300-450 °C and 450°-550°C, respectively. In the first step, a dehydration of the polymer takes place during the formation of polyene structures. Other side products besides water are acetaldehyde, acetone, furan and acetic acid. The next step at higher temperatures is even more complex since chain-scission reactions, side-reactions and cyclization reactions occur [40]. Consequently, further characterization with TG-MS-FTIR is planned in order to completely understand and solve this mechanism.

Following the experiments on PVA, TGA-DTA was performed on SnS_2, which was ball milled for 10 hours at 200 rpm prior to the measurements. Figure 50 shows the results of a TG-DTA experiment of SnS_2 in 100 ml/min argon flow at a heating rate of 10°C/min up to a temperature of 1200 °C.

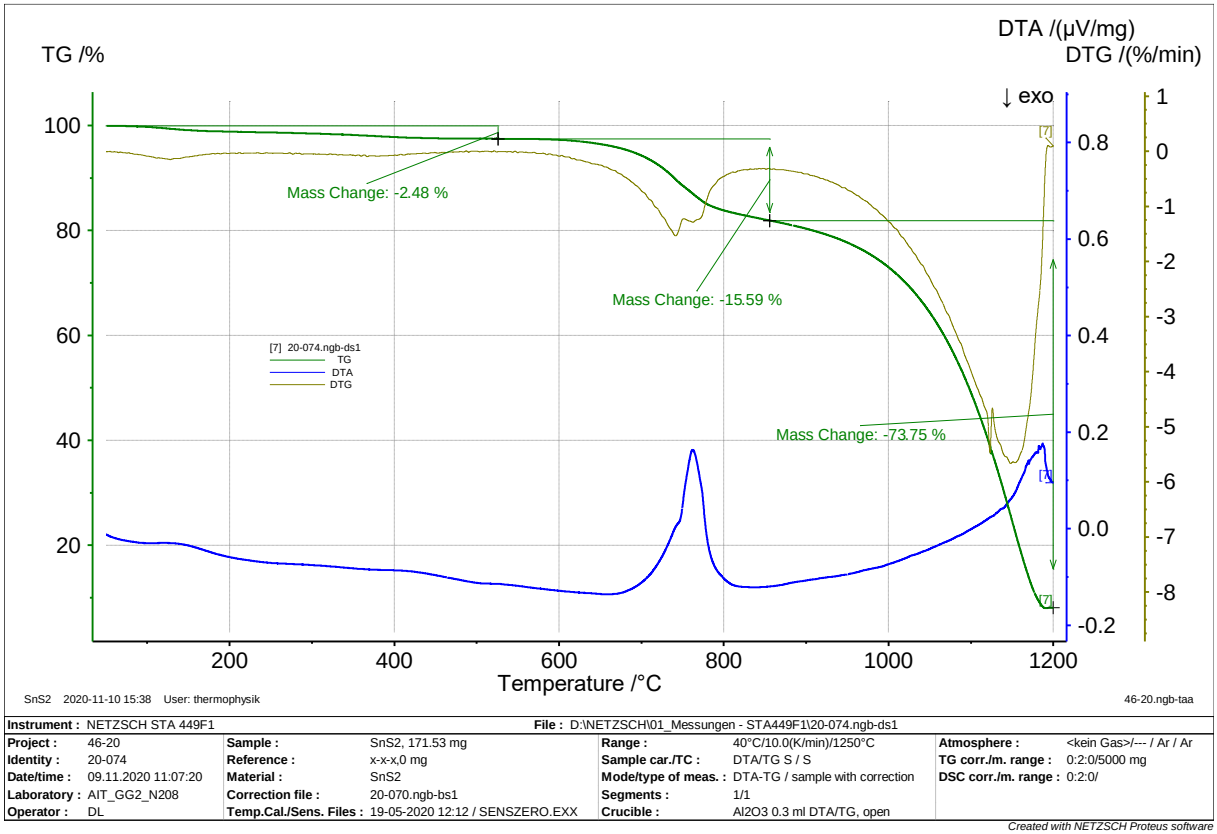

Figure 50: TG-DTA of ball milled 10 hours 200 rpm SnS_2 in argon flow atmosphere up to 1200 °C.

Three steps are indicated in the TG curve. The first mass loss of 2.5% prior to 500 °C was identified as H_2O using mass spectrometry and confirms the release of water discussed in chapter 6.1.6. Further mass losses of 15.6% and 73.8% are shown for the second and third steps, respectively. Consequently, a residual mass of 8.2% and a total mass loss of 91.8 % were detected. According to the Sn–S phase diagram of Lindwall et al. [27], the peritectic reaction L + SnS_2 ⇋ Sn_2S_3 occurs at 758 °C, what could be ascribed to the peak maximum in the DTA signal. Unfortunately, the gas outlet was blocked by sulfur precipitates during the experiment and the residual mass was too low for PXRD analysis of the reaction product in order to characterize the phases present. However, according to the measured TG-DTA data, SnS_2 seems to be stable in argon flow atmosphere up to about 600 °C.

Further TG-DTA measurements were performed on mixtures of SnS_2 (ball-milled for 10 hours 200 rpm) and PVA in order to check for any reactions between the two substances on heating. The 1:1 SnS_2/PVA mixture was homogenized prior to the TG experiments with an agate mortar. Figure 51 illustrates the TG-DTG curve of a 1:1 mass mixture of SnS_2 and PVA in 100ml/min argon flow up to a temperature of 900 °C with a heating rate of 10°C/min.

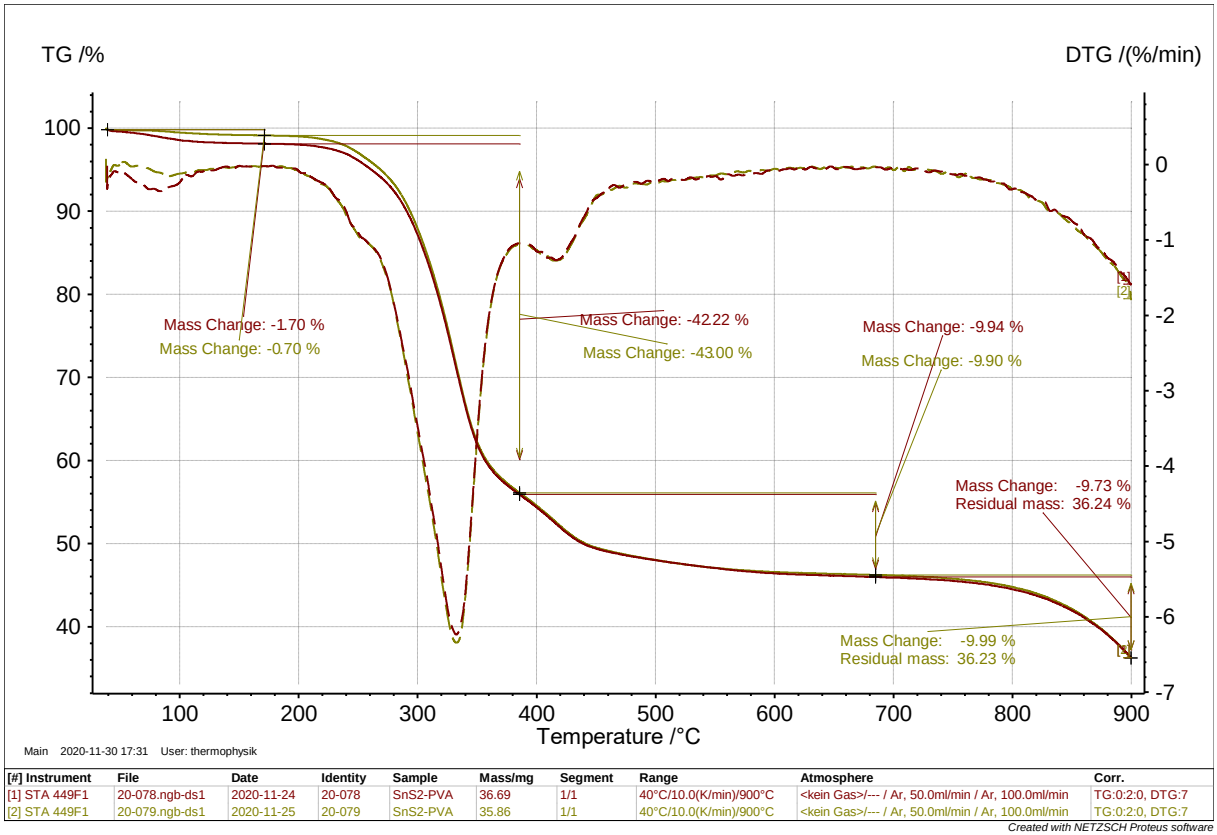

[#] Instrument	File	Date	Identity	Sample	Mass/mg	Segment	Range	Atmosphere	Corr.
[1] STA 449F1	20-078.ngb-ds1	2020-11-24	20-078	SnS2-PVA	36.69	1/1	40°C/10.0(K/min)/900°C	<kein Gas>/--- / Ar, 50.0ml/min / Ar, 100.0ml/min	TG:0:2:0, DTG:7
[2] STA 449F1	20-079.ngb-ds1	2020-11-25	20-079	SnS2-PVA	35.86	1/1	40°C/10.0(K/min)/900°C	<kein Gas>/--- / Ar, 50.0ml/min / Ar, 100.0ml/min	TG:0:2:0, DTG:7

Created with NETZSCH Proteus software

Figure 51: TG-DTG of a 1:1 mixture of SnS_2/PVA in argon flow atmosphere with a heating rate of 10°C/min up to 900 °C.

The mixture loses about 1 % of its mass in the first step, 43 % in the second and 10 % in the third and the fourth steps. Consequently, a residual mass of 36.2% and a total mass loss of 64% were detected. Unfortunately, no articles in literature have been found that describe the thermal decomposition mechanism of the SnS_2/PVA mixture. Despite this, 500°C seems to be a suitable coating temperature, since at that temperature the thermal decomposition product of PVA is stable and SnS_2 only loses about 2.5% of its initial mass, which was detected as H_2O. Consequently, isothermal TG at 500 °C was performed on a 1:1 wt. mixture of ball milled (10 hours 200 rpm) SnS_2 and PVA in order to confirm the stability of the product at 500°C. Figure 52 illustrates an isothermal TG experiment at 500 °C for 2 hours in argon flow atmosphere with 20 ml/min, which was performed with a 1:1 wt. mixture of ball milled (10 hours 200 rpm) SnS_2 and PVA.

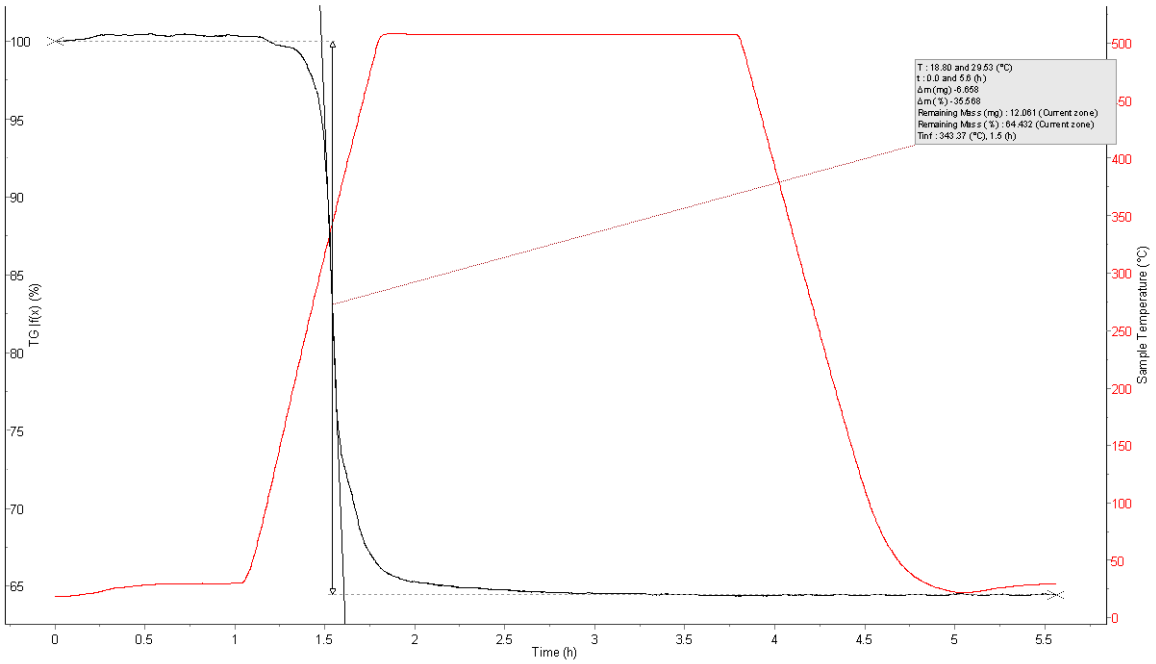

Figure 52: Isothermal TG of a 1:1 mixture of SnS_2 and PVA at 500 °C in argon flow atmosphere 20ml/min for 2 hours.

The measurement shows that the major mass loss takes place even before reaching the temperature of 500 °C. During the isothermal segment, the mass loss of the sample stabilizes to its final value of about 35.6%.

Based on this, coating experiments in a tube furnace at the AIT were performed. However, conditions are not completely identical to the TG setup since the flow of inert gas, the size of the system and the sample amount are different. These investigations are described in more detail in subchapter 6.2.3.

6.2.2 Isothermal TGA of SnS_2 in argon atmosphere

In order to gather further insight into the behavior of pristine SnS_2 during isothermal treatment at 500 °C in argon flow atmosphere, additional heat treatment experiments were performed with SnS_2 samples in a DTA/TGA device in argon flow at a rate of 20 ml /minute at the university of Vienna. The isothermal measurements were performed for 2, 5, 10, 15 and 20 hours, respectively, and the latter is shown in Figure 53.

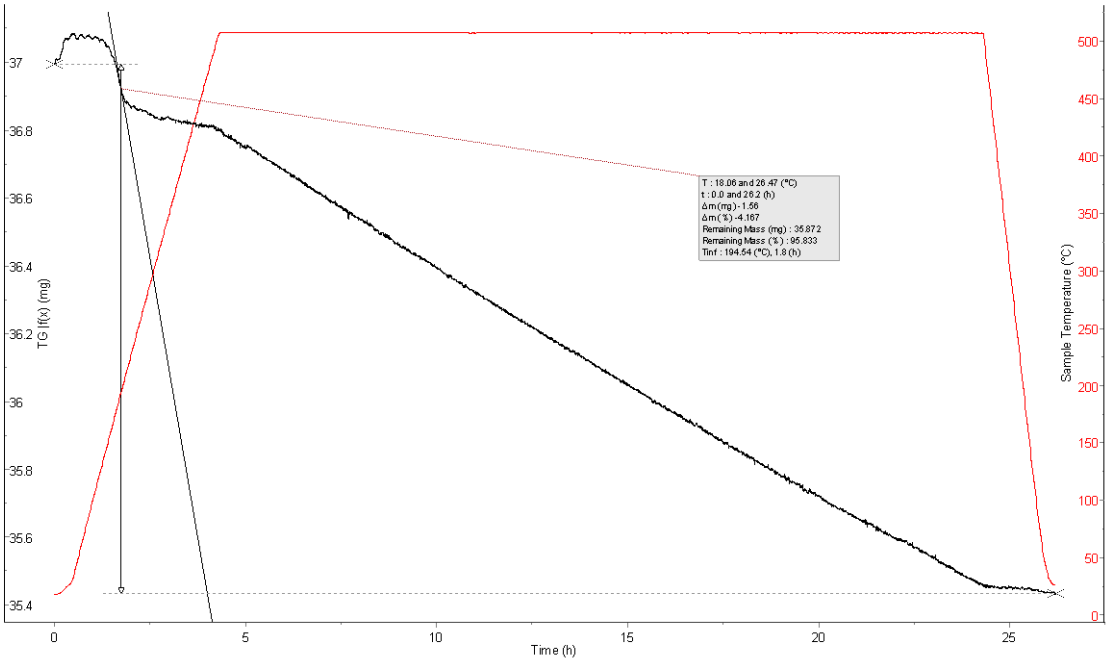

Figure 53: Isothermal TG of SnS_2 at 500 °C for 20 hours in argon flow atmosphere 20ml/min.

During heating, a virtual mass gain[3] is detected at lower temperatures, which can be neglected for the determination of the total mass loss. After reaching the temperature of 500 °C, the mass loss is continuous, and the total mass loss after 20 hours at 500 °C is 4.4 %. Table 13 lists the mass losses of SnS_2 after isothermal heat treatment for 2, 5, 10, 15, and 20 hours at 500 °C in argon flow atmosphere with 20 ml/min. The mass losses were determined by externally weighing the samples before and after the reaction using a microbalance, as well as by the measured TG data.

Table 13: mass loss of SnS_2 in percentage after isothermal TG at 500°.

Time [h]	Microbalance [%]	TG [%]	XRD [%]
2	1.22	1.01	1.36
5	1.68	1.52	1.46
10	3.44	2.84	3.39
15	4.96	3.81	5.02
20	4.44	4.17	5.44

According to the data, the mass loss increases steadily with increasing thermal treatment time from about 1 % at 2 hours to 4.4% after 20 hours. However, the sample that was heat treated for 15 hours does not fit the overall trend since the mass loss that was detected with external weighing is comparably high. Therefore, this measurement is going to be repeated for

[3] On heating the density of the Ar gas and thus the buoyant force lowers resulting in a virtual gain of mass. This is usually compensated by base line correction which obviously did not work properly in this case. This has, however, no impact on the total mass loss.

clarification. The remaining samples after TGA were further characterized using PXRD and the measured XRD patterns are illustrated in Figure 54.

The crystalline phases after isothermal heat treatment at 500 °C were identified as Sn_2S_3 (Ottemannite) and SnS_2 (Berndtite). Obviously, sulfur vapor which is formed from solid SnS_2 is transported by argon gas out of the system and shifts the equilibrium $2\ SnS_2 \rightarrow Sn_2S_3 + S(g)\uparrow$ to the right side.

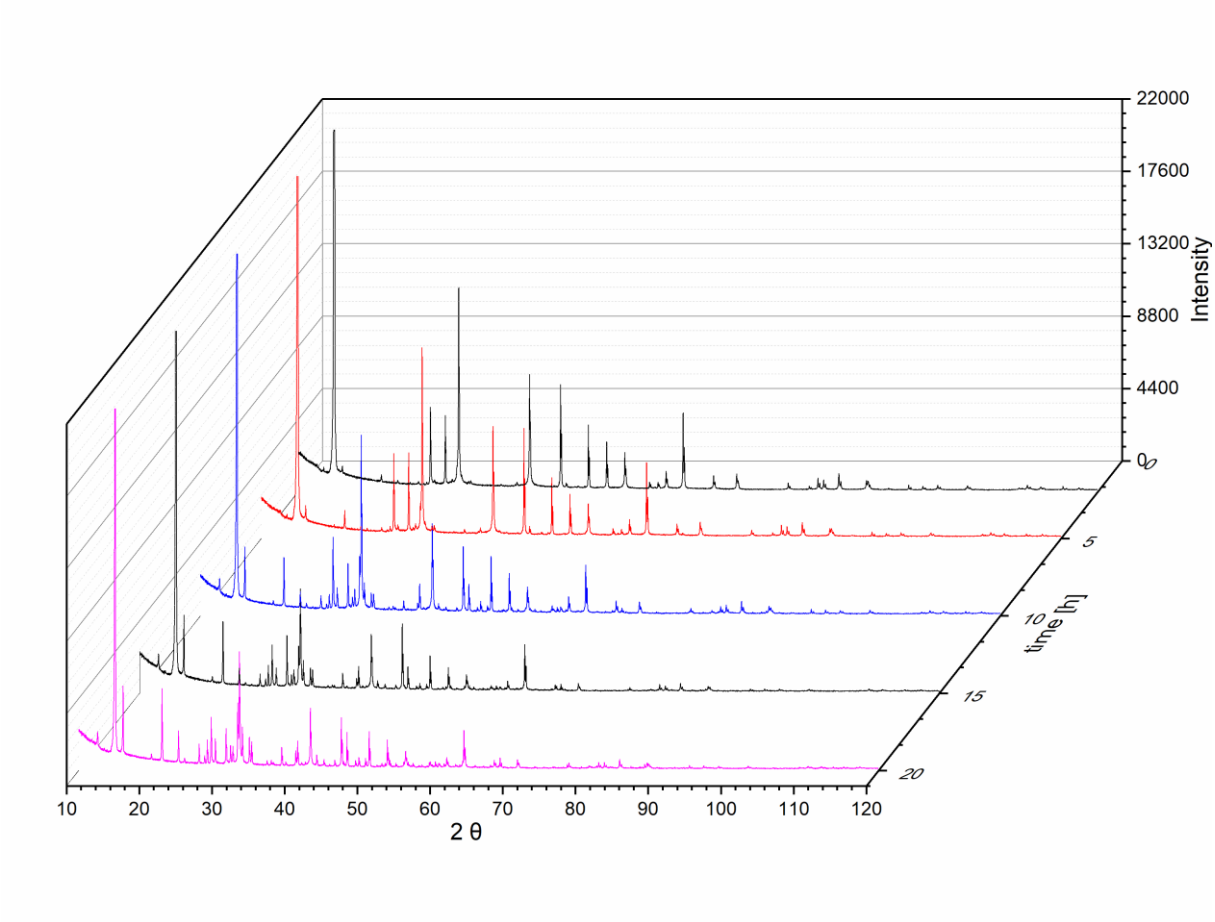

Figure 54: XRD pattern of heat treated SnS_2 at 500 °C for 2, 5, 10, 15 and 20 hours.

All patterns were refined separately and Figure 55 shows the XRD pattern of the powder after isothermal treatment at 500 °C for 20 hours.

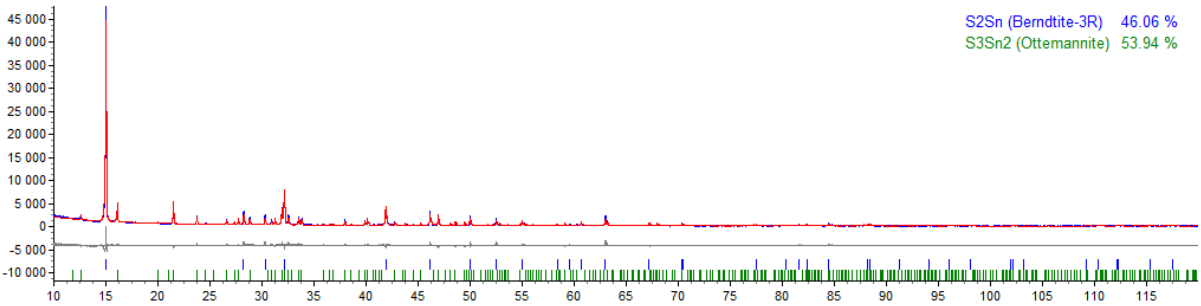

Figure 55: XRD pattern of heat treated SnS_2 at 500 °C for 20 hours.

Table 14 summarizes the data from the Rietveld refinements of the PXRD patterns of the SnS_2 samples that were heat treated for 2 hours, 5 hours, 10 hours, 15 hours and 20 hours at 500 °C. The relative amounts of masses of SnS_2 and Sn_2S_3 from XRD refinements were used to

calculate the mass loss. The results are compared with those from TG in Table 13. Considering a rather large error of amounts of masses from XRD the agreement is quite satisfying.

Table 14: Rietveld refinement of SnS_2 samples after isothermal TG at 500 °C in argon flow atmosphere with 20 ml/min.

Time at 500°C				Lattice parameters [Å]			
	phase	amount [%]	space group	a	b	c	R_{wp}
2h	SnS_2	86	P-3m1	3.6480(3)		5.8983(7)	13.002
	Sn_2S_3	14	Pnma	8.87(2)	3.749(8)	14.02(3)	
5h	SnS_2	85	P-3m1	3.6483(3)		5.8983(7)	13.02
	Sn_2S_3	15	Pnma	8.869(7)	3.749(2)	14.02(1)	
10h	SnS_2	66	P-3m1	3.648229		5.8982038	13.228
	Sn_2S_3	34	Pnma	8.8678856	3.7488688	14.0203756	
15h	SnS_2	50	P-3m1	3.6482(3)		5.8984(7)	11.098
	Sn_2S_3	50	Pnma	8.8688(2)	3.7486(9)	14.022(3)	
20h	SnS_2	46	P-3m1	3.6481(4)		5.8984(4)	11.081
	Sn_2S_3	54	Pnma	8.869(2)	3.7484(7)	14.0226(2)	

To summarize the results of these measurements, the longer the heat treatment time, the more SnS_2 was converted into Sn_2S_3. Interestingly there is no significant difference in the amounts of crystalline phases of SnS_2 and Sn_2S_3 between isothermal treatment for 2 hours and 5 hours. After 15 hours of isothermal heat treatment at 500 °C, however, half of the initial SnS_2 is converted to Sn_2S_3. Towards 20 hours of heat treatment more than 54 % is converted into Sn_2S_3.

6.2.3 Coating experiments

Based on the results of the TGA-DTA investigations which were previously presented, coating experiments were performed on 1:1 wt. mixtures of ball-milled SnS_2 (10 hours at 200 rpm) and PVA, which were heat treated at 500°C for 1 minute, 2 hours, 5 hours, 10 hours and 15 hours in a tube furnace at AIT using an argon flow of 100 ml/min. The furnace was heated up and cooled down at rates of 2°C/min and 5°C/min, respectively. Prior to starting the heat treatment experiments, the tube furnace was fully evacuated once and re-filled with Ar gas. The masses of the samples before and after the heat treatments were measured using a microbalance. Additionally, PXRD was performed on the reaction products in order to identify the crystalline phases after the decomposition reaction. Table 15 lists the mass losses of the heat treated SnS_2/PVA samples at 500°C, whereas Figure 56 shows the data as a function of time.

Table 15: mass loss of SnS_2/PVA 500 °C tube furnace.

time [h]	Mass loss [%]
0.02	51.0
2	51.1
5	51.9
10	53.0
15	54.2

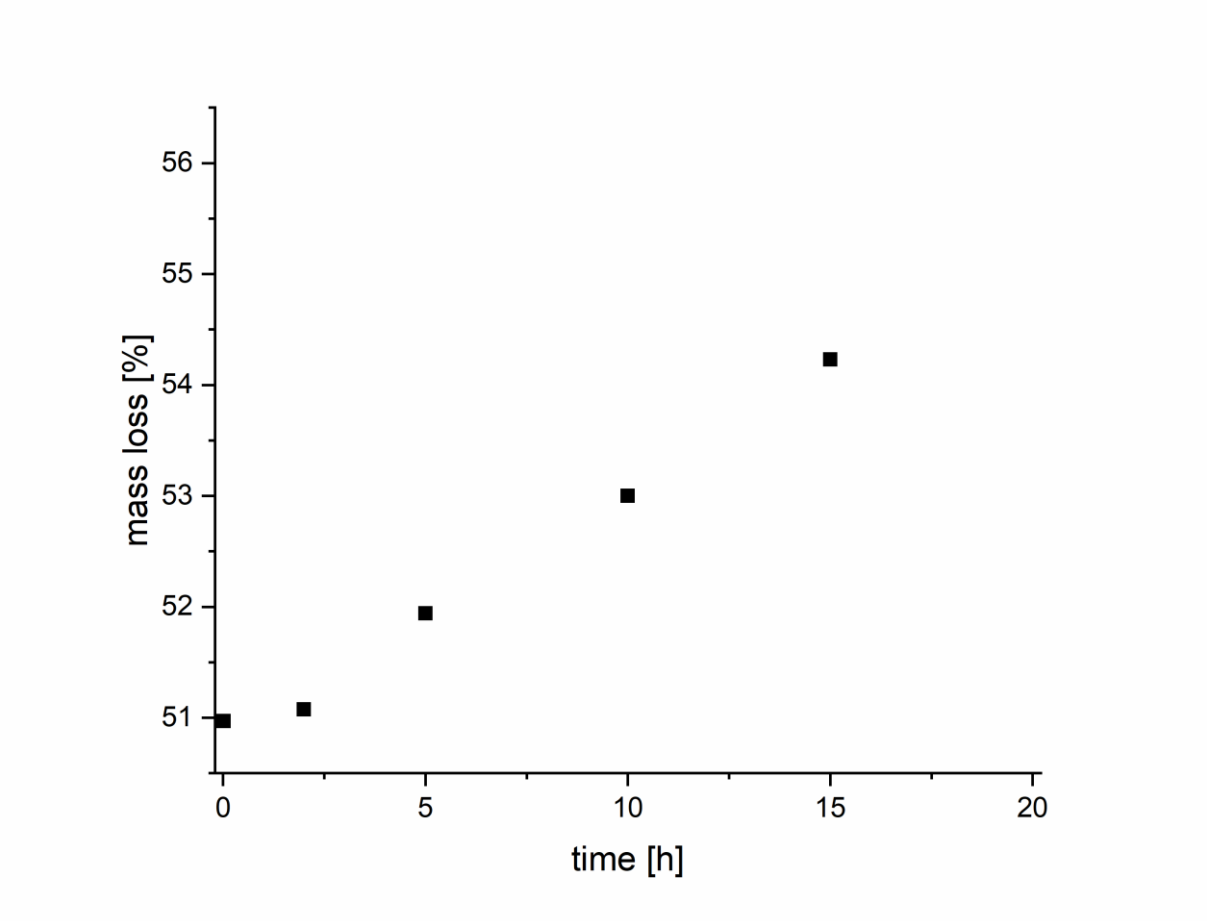

Figure 56: Mass losses of SnS_2/PVA after different time durations of isothermal heat treatment at 500°C.

Figure 56 shows a relatively linear change in the mass loss of the 1:1 mixture of SnS_2 and PVA after heat treatment at 500 °C for the different time durations. However, the sample which was kept at 500 °C for only one minute does not fit the linear mass loss model. Obviously, approx.

50 % of mass loss occurred already on heating before the isothermal segment started. This assumption is supported by the TGA measurement shown in Figure 51, where the mass loss is approx. 53 % after heating with 10 K/min.

The decomposition reaction products were further characterized using Rietveld analysis of the measured PXRD patterns, which are shown in Figure 57.

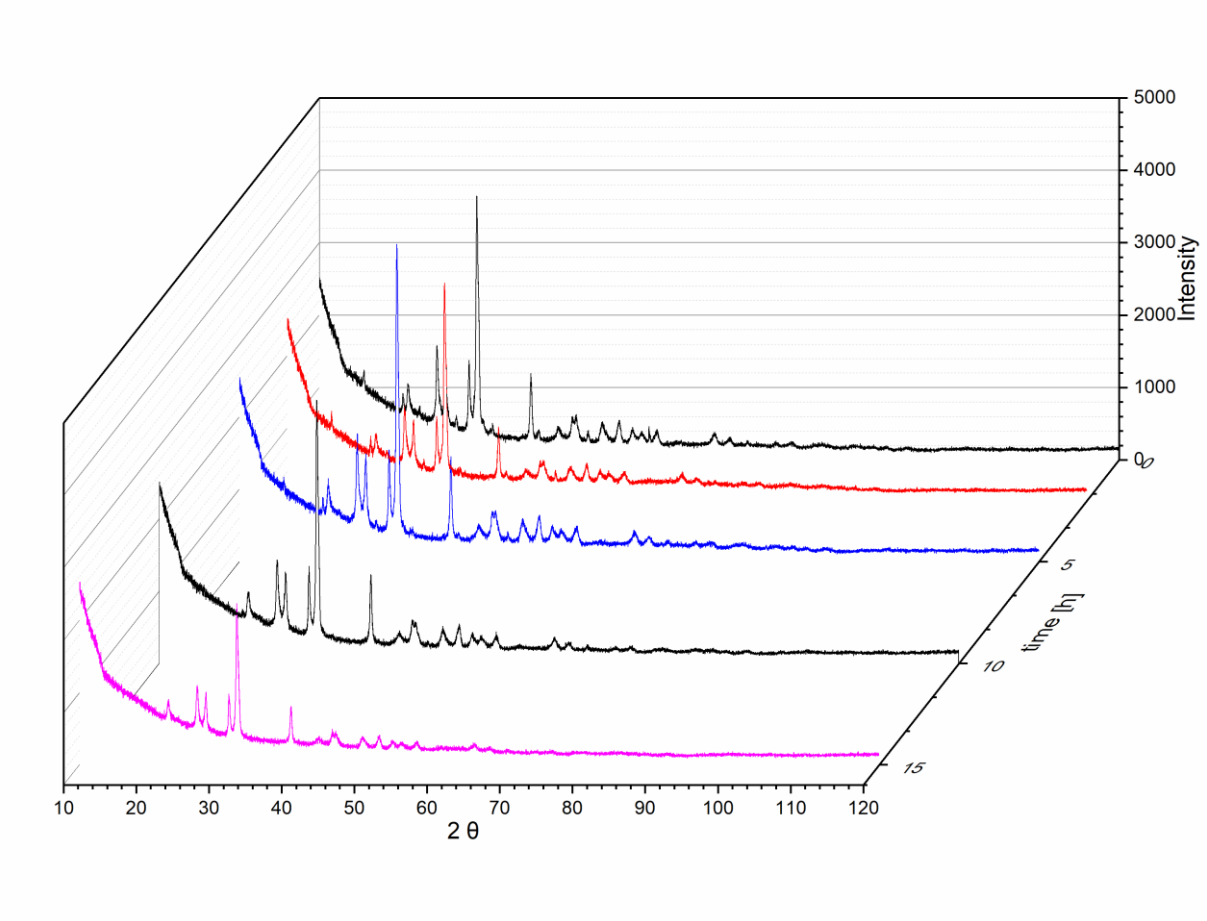

Figure 57: XRD pattern of the heat treated (500°C) PVA/SnS_2 mixtures.

Table 16 further lists the results of the Rietveld refinements of the SnS_2/ PVA samples after heat treatment at 500 °C for different time durations. It includes the amount of the respective crystalline phases, space group, lattice parameters and R-value. An example of the Rietveld refinements is shown in Figure 58, where the measured, calculated, and difference patterns as well as the calculated patterns for the individual phases are shown for the sample which was heat treated for 2 hours at 500°C.

Table 16: Rietveld refinement of SnS_2/PVA samples after treatment at 500 °C for 1 minute, 2, 5, 10 and 15 hours.

sample	phase	amount [%]	space group	Lattice parameters [Å] a	b	c	R_{wp}
SnS_2_PVA_500C_0h	LT-SnS	87	Pnma	11.243(8)	3.996(3)	4.267(4)	9.415
	Sn_2S_3	13	Pnma	8.86(2)	3.739(7)	13.99(3)	
SnS_2_PVA_500C_2h	LT-SnS	89	Pnma	11.274(8)	4.000(4)	4.269(4)	8.229
	Sn_2S_3	11	Pnma	8.87(2)	3.745(6)	14.01(2)	
SnS_2_PVA_500C_5h	LT-SnS	93	Pnma	11.27(1)	4.007(4)	4.273(4)	8.878
	Sn_2S_3	7	Pnma	8.88(2)	3.750(8)	14.03(3)	
SnS_2_PVA_500C_10h	LT-SnS	97	Pnma	11.27(1)	4.008(4)	4.272(5)	9.119
	Sn_2S_3	3	Pnma	8.88(4)	3.81(2)	13.93(5)	
SnS_2_PVA_500C_15h	LT-SnS	100	Pnma	11.29(2)	4.005(7)	4.278(7)	7.625

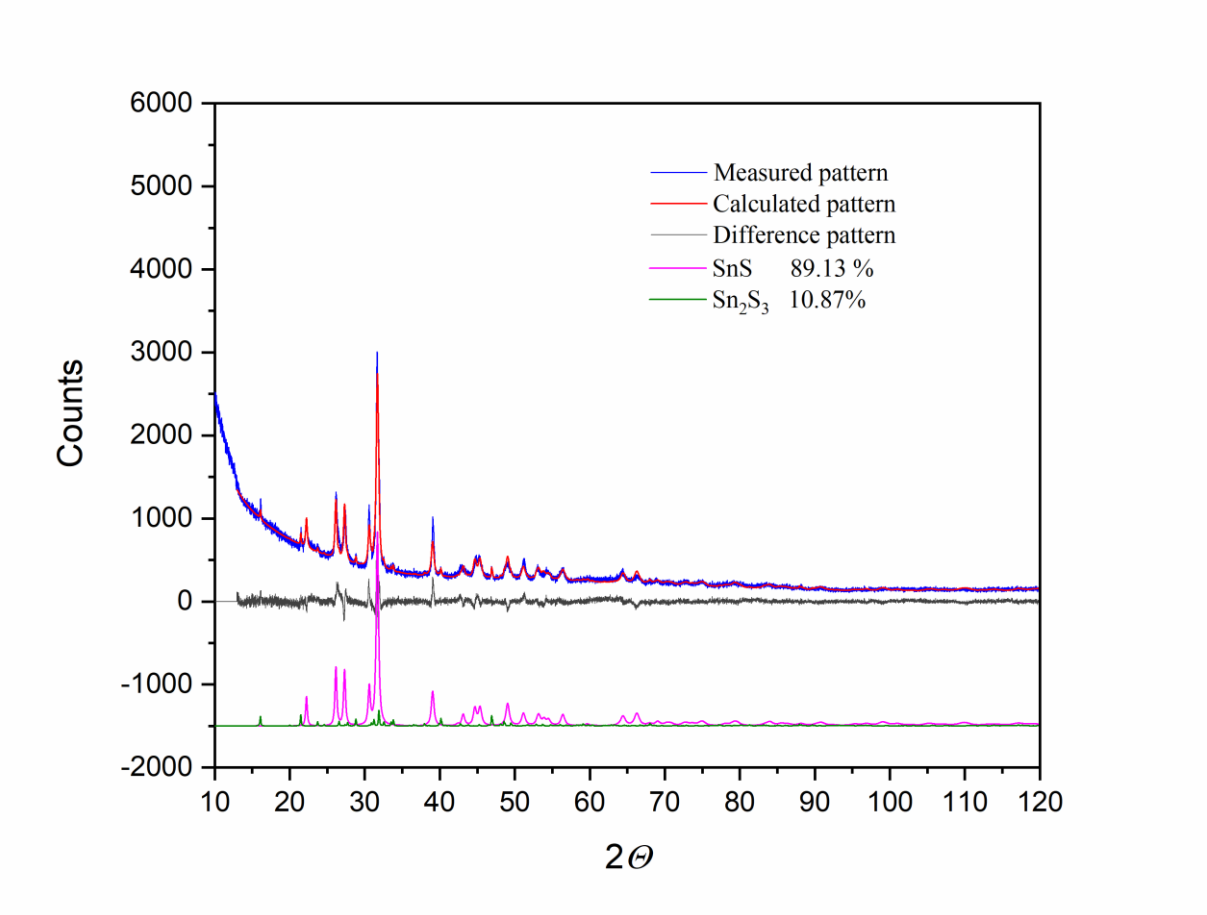

Figure 58: crystalline phases of SnS_2/PVA after 2 hours at 500 °C.

In contrast to the TGA experiments on the decomposition of pure SnS_2 at 500°C in argon, SnS_2 could not be detected in any of the samples which were mixed with PVA, not even in the sample which spent only 1 minute at 500 °C. In fact, as the heat treatment time increases, the amount of SnS increases until a phase pure sample is achieved after 15 hours. Furthermore, no carbonaceous crystalline phases were found in any of the samples. PVA or possible decomposition products like CO therefore seem to act as reducing agent which facilitates the conversion of SnS_2 to SnS via the Sn_2S_3 intermediate according to:

$$2\ SnS_2 \rightarrow Sn_2S_3 + S\uparrow \text{ and } Sn_2S_3 \rightarrow 2\ SnS + S\uparrow$$

SnS does not further decompose into sulfur and tin but evaporates since SnS and similar species are stable in the gas phase [56]; compare also with the TGA curve in Figure 50 which shows heating of SnS_2 up to 1200 °C with a mass loss of approx. 95 %. The amounts of crystalline phases from the Rietveld refinements of the measured XRD patterns are graphically illustrated in Figure 59 as a function of heat treatment time.

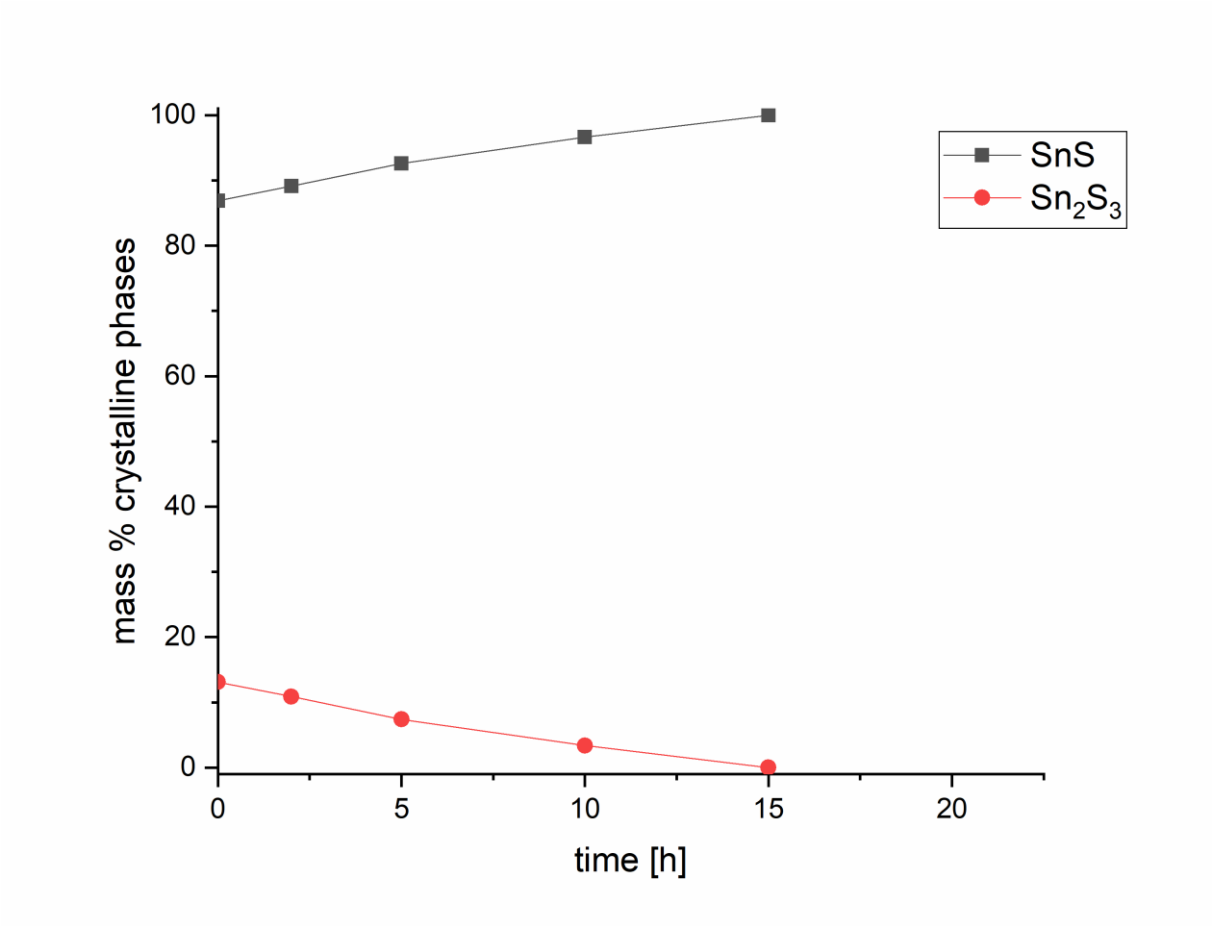

Figure 59: Ratio of SnS (grey) and Sn_2S_3 (red) after isothermal heat treatment of SnS_2 with PVA at 500 °C.

These results show that it is not possible to create a carbon coating on SnS_2 under these conditions using PVA, as the SnS_2 is reduced to Sn_2S_3 and SnS due to the reaction with PVA in flowing Ar atmospheres. Despite this, SEM was performed on the samples which were heat treated for 5, 10, and 15 hours in order to investigate the particle and coating morphologies after heat treatment (see Figure 60).

Figure 60 illustrates SEM graphs of SnS_2/PVA samples that were isothermally treated at a temperature of 500 °C for 5 hours, 10 hours respectively 15 hours.

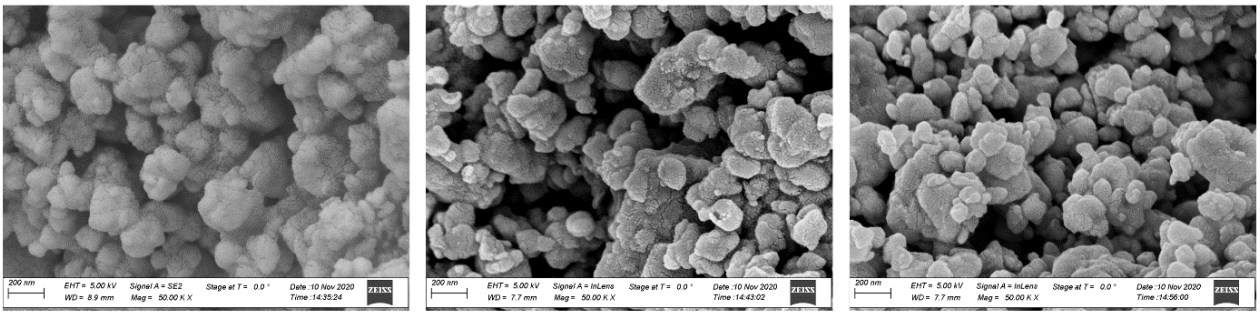

Figure 60: SEM micrograph of a 1:1 mixture of SnS_2 and PVA after heat treatment at 500 °C for a) 5 hours, b) 10 hours and c) 15 hours.

The three micrographs show coated nanoparticles with some cracks in the coating layer. The cracks may have been generated due to gas formation at the tin sulfide particles / coating interfaces during the heat treatment. Future investigations such as Fourier transform infrared spectroscopy (FTIR), Raman spectroscopy and X-ray photoelectron spectroscopy (XPS) should be carried out to determine the chemical composition of the coating layer. Additionally, transmission electron microscopy (TEM) measurements are desirable to determine the thickness of coating.

To summarize, these investigations did not lead to desired results of coated SnS_2 nanoparticles. Nevertheless, valuable information could still be obtained about the thermal decomposition behavior of SnS_2 mixed with PVA. Additionally, a new synthesis method for preparing coated SnS nanoparticles starting from SnS_2 and PVA was found. For future work, the electrochemical behavior of coated SnS nanoparticles should be performed and promise further interesting research opportunities for the future.

7 Appendix

7.1 Abstract

Commercially produced Li-ion batteries usually contain graphite as anode active material, this master's thesis goal is the development and improvement of alternative SnS_2 anode materials. Two different approaches were performed in order to coat SnS_2 with a conducting carbon layer, namely a mechanochemical route (ball milling) and a thermal route. Powders and electrodes were characterized using scanning electron microscopy (SEM), powder X-ray diffraction (XRD) and selected samples were further investigated using thermogravimetric analysis (TGA). The electrochemical performance of prepared coin cells was determined with galvanostatic cycling under potential limitation (GCPL).

Preliminary investigations lead to promising ball milling parameters for the first approach, whereas 10 hours seems to be a suitable milling time. Mechanochemical treatment with ball milling successfully improved the electrochemical performance of half cells. Firstly, through the reduction of particle sizes and secondly through the synthesis of SnS_2/carbon composite materials. Ball milling for 10 hours at 200 rpm without carbon resulted in lower capacity degradation compared to pristine SnS_2 electrodes. Superior results were achieved with SnS_2/C composites containing 10 wt. % graphite, whereby the powders were milled for 10 hours at 400 rpm. There was almost no decrease in specific capacity after first cycling and thus a very high coulombic efficiency was detected. Selected samples were further investigated regarding their carbon content using TGA. A trend that the carbon content after ball-milling was higher than expected was shown, that is most probably due to the preferred adhesion of SnS_2 onto the milling bowl and spheres.

Post-mortem XRD on cycled electrodes after 50 cycles revealed that for powders that were milled with a high value of revolution per minute no crystalline structures were detected anymore. This trend was shown in phase pure samples as well as with additional graphite. Additionally, a new polytype of SnS_2, that has not been described by scientific literatures yet, was identified after ball milling for 10 h with 400 rpm. Further investigations regarding its lithiation mechanism during equilibrium discharge were performed. Future work concerning the new polytype of SnS_2 is planned using single crystal XRD for structural clarification. The equilibrium discharge states should preferentially be reinvestigated with galvanostatic intermittent titration technique (GITT).

The second approach dealt with carbon coating of anode active materials using a thermal method and polyvinyl alcohol (PVA) as carbon source. Unfortunately, the initially promising coating temperature of 500 °C turned out to be unsuccessful in the end, since SnS_2 is not stable, neither in its pristine form, nor in a 1:1 wt. mixture with PVA. Under the presence of PVA at 500 °C SnS_2 decomposes into SnS and Sn_2S, whereby the fraction of SnS rises with rising duration of the treatment. Nevertheless, it was possible to gather valuable information about the conversion of SnS_2 and an additional promising way to synthesize SnS was found. TG-DTA-MS-FTIR will be carried out in order to understand the different behavior of SnS_2 in presence of PVA regarding the occurring gas species. The powdered samples were investigated using SEM, XRD and partially TGA. The success of coating was shown using SEM. Future work will be performed in order to determine the composition of the coated layer regarding the purity of carbon in detail with IR/Raman-spectroscopy. Electrochemical investigations of the PVA coating approach have not yet been completed by the time this master's thesis ends, but they show promising intermediate data and possible further development opportunities for the future.

7.2 Zusammenfassung (Deutsch)

Zur Verbesserung der elektrochemischen Eigenschaften von SnS_2 Anodenmaterialien als Alternativen für Graphit in Lithiumionenbatterien wurden im Rahmen dieser Arbeit zwei unterschiedliche Ansätze mit dem Ziel, Kohlenstoffschichten auf SnS_2-Partikel anzubringen, durchgeführt. Im Zuge des mechanochemischen Ansatzes wurden Mahlversuche mit einer Kugelmühle durchgeführt und zunächst passende Parameter für die Methode gesucht. Die Pulver, sowie die nach wissenschaftlichem Standard hergestellten Elektroden, wurden jeweils mittels Rasterelektronenmikroskopie und Röntgenbeugung untersucht. Ausgewählte Pulverproben wurden auch mittels thermischer Analyse hinsichtlich des Kohlenstoffgehaltes untersucht, die Eignung der TGA Methode zur Messung des Kohlenstoffgehaltes wurde vorher nachgewiesen. Es zeigte sich, dass der Kohlenstoffgehalt systematisch höher ist als gemäß Einwaage, dies liegt vermutlich an der unterschiedlichen Haftung der beiden Materialien am Mahlbecher und den Kugeln.

Das elektrochemische Verhalten und die Kapazitätsstabilität des auf SnS_2 basierenden Elektrodenmaterials konnten einerseits mittels Verkleinerung der Partikelgrößen, hier lieferte das Mahlen für 10 Stunden bei 200 rpm das beste Ergebnis, und andererseits durch Herstellung von SnS_2/C Gemischen erreicht werden. Elektroden, deren Pulvergemische für 10 Stunden bei 400 rpm mit 10 % Graphit gemahlen wurden, zeigten herausragende elektrochemische Eigenschaften. Weiters wurde eine Überstruktur von SnS_2 gefunden, welche bisher nicht in der Fachliteratur beschrieben ist. Diese entstand nach Mahlen des Pulvers für 10 Stunden bei 400 rpm und konnte mittels Pulverdiffraktometrie kristallografisch beschrieben werden. Die Aufklärung der Phasenumwandlungen bei der stufenweisen elektrochemischen Lithiierung jener Struktur war großteils erfolgreich und zeigt die Unterschiede im Vergleich zu der herkömmlichen SnS_2 Struktur auf. Zur weiteren Aufklärung sind Messungen mittels galvanostatic intermittent titration technique (GITT) geplant. Post-mortem XRD Untersuchungen der Elektroden aus Pulvern unter harschen Mahlbedingungen zeigten, dass nach 50 Entlade/Ladezyklen in den meisten Fällen keine kristallinen Strukturen mehr vorhanden sind.

Der zweite Ansatz befasste sich mit der Kohlenstoffbeschichtung der SnS_2 Anodenmaterialien mittels thermischer Behandlung unter Verwendung von Polyvinylalkohol (PVA) als Kohlenstoffquelle. Leider stellte sich eine thermische Instabilität von SnS_2 unter Anwesenheit von PVA bei der zunächst aus reinem SnS_2 ermittelten Beschichtungstemperatur von 500 °C heraus. Unter Anwesenheit von PVA wandelt sich SnS_2 bei 500 °C zu SnS und Sn_2S_3 um, wobei der Anteil von SnS mit steigender Behandlungsdauer zunimmt. Nichtsdestotrotz konnten wertvolle Informationen bezüglich Stabilität des Materials und Anwendbarkeit der Beschichtungsmethode gesammelt werden. Die thermische Zersetzung SnS_2 von ist eine vielversprechende Synthesemethode für SnS, welches bisher schwer herzustellen war. TG-DTA-MS-FTIR Untersuchen zur Analyse der bei der Zersetzung entstehenden Gasspezies sind geplant. Die beschichteten Proben wurden mit XRD, TGA und SEM untersucht. Dabei bestätigte sich die Ausbildung einer Schicht, allerdings muss in zukünftigen Raman/IR-Messungen noch die Zusammensetzung hinsichtlich ihrer Reinheit geklärt werden. Die elektrochemischen Untersuchungen des Beschichtungsansatzes sind zum Zeitpunkt der Fertigstellung dieser Masterarbeit noch nicht abgeschlossen, versprechen aber interessante mögliche Weiterentwicklungsmöglichkeiten für die Zukunft.

7.3 List of figures

Ich habe mich bemüht, sämtliche Inhaber der Bildrechte ausfindig zu machen und ihre Zustimmung zur Verwendung der Bilder in dieser Arbeit eingeholt. Sollte dennoch eine Urheberrechtsverletzung bekannt werden, ersuche ich um Meldung bei mir.

7.4 List of tables

8 References

1. *Handbook of battery materials*. (Wiley-VCH Verlag, 2011).

2. Goodenough, J. B. & Park, K.-S. The Li-Ion Rechargeable Battery: A Perspective. *J. Am. Chem. Soc.* **135**, 1167–1176 (2013).

3. Miao, Y., Hynan, P., von Jouanne, A. & Yokochi, A. Current Li-Ion Battery Technologies in Electric Vehicles and Opportunities for Advancements. *Energies (Basel)* **12**, 1074 (2019).

4. Kamat, P. V. Lithium-Ion Batteries and Beyond: Celebrating the 2019 Nobel Prize in Chemistry – A Virtual Issue. *ACS Energy Lett.* **4**, 2757–2759 (2019).

5. Popp, H., Koller, M., Jahn, M. & Bergmann, A. Mechanical methods for state determination of Lithium-Ion secondary batteries: A review. *J. Energy Storage* **32**, 101859 (2020).

6. Hannan, M. A., Lipu, M. S. H., Hussain, A. & Mohamed, A. A review of lithium-ion battery state of charge estimation and management system in electric vehicle applications: Challenges and recommendations. *Renew. Sustain. Energy Rev.* **78**, 834–854 (2017).

7. Huggins, R. A. *Advanced batteries : materials science aspects*. (Springer, 2009).

8. Gomadam, P. M., Weidner, J. W., Dougal, R. A. & White, R. E. Mathematical modeling of lithium-ion and nickel battery systems. *J. Power Sources* **110**, 267–284 (2002).

9. Zhang, W.-J. A review of the electrochemical performance of alloy anodes for lithium-ion batteries. *J. Power Sources* **196**, 13–24 (2011).

10. Godshall, N. A., Raistrick, I. D. & Huggins, R. A. Relationships among Electrochemical, Thermodynamic, and Oxygen Potential Quantities in Lithium-Transition Metal-Oxygen Molten Salt Cells. *J. Electrochem. Soc.* **131**, 543–549 (1984).

11. Blomgren, G. E. The Development and Future of Lithium Ion Batteries. *J. Electrochem. Soc.* **164**, A5019--A5025 (2016).

12. Karmakar, S., Chowdhury, C. & Datta, A. Two-Dimensional Group IV Monochalcogenides: Anode Materials for Li-Ion Batteries. *J. Phys. Chem. C* **120**, 14522–14530 (2016).

13. Wachtler, M., Besenhard, J. O. & Winter, M. Tin and tin-based intermetallics as new anode materials for lithium-ion cells. *J. Power Sources* **94**, 189–193 (2001).

14. Li, D., Fürtauer, S., Flandorfer, H. & Cupid, D. M. Thermodynamic assessment and experimental investigation of the Li–Sn system. *Calphad* **47**, 181–195

(2014).

15. Son, Y., Sung, J., Son, Y. & Cho, J. Recent progress of analysis techniques for silicon-based anode of lithium-ion batteries. *Curr. Opin. Electrochem.* **6**, 77–83 (2017).

16. Nitta, N., Wu, F., Lee, J. T. & Yushin, G. Li-ion battery materials: present and future. *Mater. Today* **18**, 252–264 (2015).

17. Burton, L. A. *et al.* Electronic and optical properties of single crystal SnS2: an earth-abundant disulfide photocatalyst. *J. Mater. Chem. A* **4**, 1312–1318 (2016).

18. Burton, L. A. *et al.* Synthesis, Characterization, and Electronic Structure of Single-Crystal SnS, Sn2S3, and SnS2. *Chem. Mater.* **25**, 4908–4916 (2013).

19. Chakrabarti, A. *et al.* Tin(IV) sulfide: Novel nanocrystalline morphologies. *Inorganica Chim. Acta* **374**, 627–631 (2011).

20. Ramsdell, L. S. Studies on silicon carbide. *Am. Mineral.* **32**, 64–82 (1947).

21. Dubrovskii, G. B. Crystal structure and electronic spectrum of SnS2. *Phys. Solid State* **40**, 1557–1562 (1998).

22. Minagawa, T. Common Polytypes of SnS2 and SnSe2. *J. Phys. Soc. Japan* **49**, 2317–2318 (1980).

23. Kim, T.-J., Kim, C., Son, D., Choi, M. & Park, B. Novel SnS2-nanosheet anodes for lithium-ion batteries. *J. Power Sources* **167**, 529–535 (2007).

24. MORALES, J., PEREZVICENTE, C. & TIRADO, J. Chemical and electrochemical lithium intercalation and staging in 2H□SnS2. *Solid state ionics* **51**, 133–138 (1992).

25. Lefebvre, I., Olivier-Fourcade, J., Jumas, J. & Lavela, P. Lithium insertion mechanism in SnS2. *Phys. Rev. B - PHYS REV B* **61**, 3110–3116 (2000).

26. Sharma, R. C. & Chang, Y. A. The S−Sn (Sulfur-Tin) system. *Bull. Alloy phase diagrams* **7**, 269–273 (1986).

27. Lindwall, G., Shang, S., Kelly, N. R., Anderson, T. & Liu, Z.-K. Thermodynamics of the S–Sn system: Implication for synthesis of earth abundant photovoltaic absorber materials. *Sol. Energy* **125**, 314–323 (2016).

28. Masing, G. & Tammann, G. Metallographische Mitteilungen aus dem Institut für physikalische Chemie der Universität Göttingen. LXXV. Über das Verhalten von Lithium zu Natrium, Kalium, Zinn, Cadmium und Magnesium. *Zeitschrift für Anorg. Chemie* **67**, 183–199 (1910).

29. Grube, O. & Meyer, E. ELEKTRISCHE LEITFÄHIGKEIT UND ZUSTANDSDIAGRAMM BEI BINÄREN LEGIERUNGEN. *Zeitschrift für Elektrochemie und Angew. Phys. Chemie* **40**, 771–777 (1934).

30. Reichmann, T. L., Li, D. & Cupid, D. M. Heat capacities and an updated thermodynamic model for the Li–Sn system. *Phys. Chem. Chem. Phys.* **20**, 22856–22866 (2018).

31. Sangster, J. & Bale, C. W. The Li-Sn (Lithium-Tin) System. *J. phase equilibria Diffus.* **19**, 70–75 (1998).

32. Gomollón-Bel, F. Ten Chemical Innovations That Will Change Our World: IUPAC identifies emerging technologies in Chemistry with potential to make our planet more sustainable. *Chem. Int.* **41**, 12–17.

33. Zhang, B. *et al.* Insertion compounds and composites made by ball milling for advanced sodium-ion batteries. *Nat. Commun.* **7**, 10308 (2016).

34. Xu, J. *et al.* Sulfur–Graphene Nanostructured Cathodes via Ball-Milling for High-Performance Lithium–Sulfur Batteries. *ACS Nano* **8**, 10920–10930 (2014).

35. Xia, J. *et al.* Layer-by-layered SnS2/graphene hybrid nanosheets via ball-milling as promising anode materials for lithium ion batteries. *Electrochim. Acta* **269**, 452–461 (2018).

36. Zhao, H. *et al.* Facile ball-milled synthesis of SnS2-carbon nanocomposites with superior lithium storage. *Prog. Nat. Sci.* **28**, 676–682 (2018).

37. Liu, J. *et al.* Sandwich-like SnS/Polypyrrole Ultrathin Nanosheets as High-Performance Anode Materials for Li-Ion Batteries. *ACS Appl. Mater. Interfaces* **8**, 8502–8510 (2016).

38. KIM, H. S. I. K., CHUNG, Y. H., KANG, S. H. & SUNG, Y.-E. Electrochemical behavior of carbon-coated SnS2 for use as the anode in lithium-ion batteries. *Electrochim. Acta* **54**, 3606–3610 (2009).

39. Li, Y., Tu, J. P., Huang, X. H., Wu, H. M. & Yuan, Y. F. Nanoscale SnS with and without carbon-coatings as an anode material for lithium ion batteries. *Electrochim. Acta* **52**, 1383–1389 (2006).

40. Peng, Z. & Kong, L. X. A thermal degradation mechanism of polyvinyl alcohol/silica nanocomposites. *Polym. Degrad. Stab.* **92**, 1061–1071 (2007).

41. *Principles and applications of thermal analysis*. (Blackwell Pub., 2008).

42. Röntgen, W. C. *Eine neue Art von Strahlen : = Ueber eine neue Art von Strahlen*. (Stahel, 1896).

43. West, A. R. *Solid state chemistry and its applications*. (Wiley, 2014).

44. Hahn, edited by T. *International tables for crystallography. Volume A, Space-group symmetry*. (Fifth, revised edition. Dordrecht ; London : Published for the International Union of Crystallography by Kluwer Academic Publishers, 2002., 2002).

45. Friedrich, W., Knipping, P. & Laue, M. Interferenzerscheinungen bei

Röntgenstrahlen. *Ann. Phys.* **346**, 971–988 (1913).

46. Bish, D. L. & Post, J. E. *Modern Powder Diffraction*. (De Gruyter). doi:https://doi.org/10.1515/9781501509018.

47. Guinebretiere, R. *X-ray diffraction by polycrystalline materials*. (ISTE, 2007).

48. Dinnebier, R. E., Leineweber, A. & Evans, J. S. O. *Rietveld Refinement: Practical Powder Diffraction Pattern Analysis using TOPAS*. (De Gruyter). doi:https://doi.org/10.1515/9783110461381.

49. McMullan, D. Scanning electron microscopy 1928–1965. *Scanning* **17**, 175–185 (1995).

50. Vernon-Parry, K. D. Scanning electron microscopy: an introduction. *III-Vs Rev.* **13**, 40–44 (2000).

51. Mehta, R. Interactions, Imaging and Spectra in SEM. in *Scanning Electron Microscopy* (ed. Kazmiruk, V.) (IntechOpen, 2012). doi:10.5772/35586.

52. Coats, A. W. & Redfern, J. P. Thermogravimetric analysis. A review. *Analyst* **88**, 906–924 (1963).

53. Prabha, D. *et al.* TG-DSC analysis, magnetic and antifungal properties of Al-doped SnS2 nanopowders. *J. Mater. Sci. Mater. Electron.* **28**, 15556–15564 (2017).

54. Raju, C. L., Rao, J. L., Reddy, B. C. V & Veera Brahmam, K. Thermal and IR studies on copper doped polyvinyl alcohol. *Bull. Mater. Sci.* **30**, 215–218 (2007).

55. Senkevich, S. I., Druzhinina, T. V, Kharchenko, I. M. & Kryazhev, Y. G. Thermal transformations of polyvinyl alcohol as a source for the preparation of carbon materials. *Solid fuel Chem.* **41**, 45–51 (2007).

56. Kellogg, H. H. Vaporization Chemistry in extractive Metallurgy. *Metall. Soc. AIME* **236**, 602–615 (1966).